An Investigation into 3D Air-based Synthetic Aperture Sonar Imaging using Compressive Sensing and an Ultrasound Transducer Array

Josiah Jideani

A dissertation submitted to the Department of Electrical Engineering,
University of Cape Town, in fulfilment of the requirements
for the degree of Master of Science in Engineering.

Cape Town, June 2013

Declaration

I declare that this dissertation is my own, unaided work. It is being submitted for the degree of Master of Science in Engineering in the University of Cape Town. It has not been submitted before for any degree or examination in any other university.

Signature of Author .....

Cape Town

March 2013

Abstract

Compressive sensing (CS) also known as compressive sampling is a technique used to reconstruct or recover the full-length of a signal with only a few non-adaptive measurements. It is a model-based framework for data acquisition and signal recovery that is based on the principles of sparsity and incoherence. Sparsity refers to the fact that a signal of interest is sparse and compressible and can be represented concisely in a given basis. Incoherence refers to the idea that a sparse signal is spread out in the basis in which it is acquired. A prominent area of application of this technique is tomography such as magnetic resonance imaging (MRI), X-ray CT, and in 3D synthetic aperture radar (SAR) imaging for reconstructing the elevation reflectivity profile. This dissertation describes the investigation into three-dimensional (3D) synthetic aperture sonar (SAS) imaging in air using compressive sampling. In the work, a 3D SAS simulator using compressive sampling was implemented in MATLAB. The effect of the number of baselines as well as the super-resolution factor on the final image was also investigated. A real 3D SAS imaging system was designed and the results were compared with the results of the simulated system. In the system, the SAS data was captured in a multiple transducer (baseline), single-pass configuration with 15 ultrasonic receivers and a single ultrasonic transmitter that operate at about 40 kHz. Signal conditioning circuits for the transmit and receive signals were built on pieces of veroboard. A PC which ran a custom designed LabVIEW virtual instrument (VI) was used for the synchronous transmission and reception of ultrasonic signals, and the control of the SAS platform via the NI PCI-6070E data acquisition card. The received 2D SAS signal from each transducer was focused using the accelerated chirp scaling algorithm. Compressive sensing was applied to a stack of focused 2D SAS images to achieve focusing in the elevation direction. 3D scenes containing point targets were successfully reconstructed in 3D SAS images using this technique with 9 baselines and a super-resolution factor of 3. The results confirm that CS is an effective technique in super-resolution tomographic reconstructions provided the baseline span is small compared to the imaging range. Also for reliable reconstructions, the appropriate super-resolution factor and number of acquisitions must be chosen.

This work is dedicated to my Lord and Saviour Jesus Christ.

Acknowledgements

I would like to thank my supervisor Assoc. Prof. A. J. Wilkinson for his guidance, assistance and supervision throughout this dissertation.

I would also like to thank my parents, Prof. I. A. Jideani and Assoc. Prof. (Mrs) V. A. Jideani and my brothers Paul Jideani and Timothy Jideani for their love, prayer, support, guidance and constant motivation during this period. May God continue to bless and keep you. I am also grateful to Yusuf Agabi and Olabisi Falowo; my pastors, for their prayers and support.

To Kiri Nicolaides of the CSIR for his support and for granting me access to the processing facilities in his research unit to be able to complete the last phase of this work.

I would also like to thank Lanche Grootboom for his support and for being a very good friend during this work. I am also grateful to my other friends and acquaintances that provided support and assistance in one way or the other during the course of this project.

Above all I would like to thank God for the life he has given me as well as the strength, wisdom and understanding to complete this work.

Contents

List of Figures

List of Tables

List of Symbols

$a_n(f,x,y)$	—	Amplitude pattern for nth target
$a_r(f,x,y)$	—	Transmit-receive mode radar amplitude pattern
B_0	—	Transmitted RF baseband bandwidth
B_t	—	Total Radar Bandwidth
B_y	—	Spatial half-beamwidth of the radiation pattern in the cross-range direction
B_{ymax}	—	Maximum half-beamwidth in the cross-range direction
c	—	Speed of light
D_x	—	Diameter of the radar or transducer in the range direction
D_y	—	Diameter of the radar or transducer in the cross-range direction
f	—	Fast-time frequency in Hertz
f_c	—	Centre frequency
$f_0(x,y)$	—	2D SAR ideal target function in the spatial domain
$f(x,y)$	—	2D SAR reconstructed target function in the spatial domain
$F(k_x,k_y)$	—	Two-dimensional Fourier transform of target function
$F_n(f,k_u)$	—	Two-dimensional Fourier transform of the point spread function of the nth target
f_s	—	Radar A/D sampling frequency
f_{prf}	—	Pulse repetition frequency
$g(s_p)$	—	One-dimensional elevation vector with $P+1$ elements
$g(x,u,s_p)$	—	Two-dimensional echoed signal received by a sensor at orbit s_p
$h_r(f,x,y)$	—	Transmit-receive mode radar radiation pattern
$H_{rx}(f)$	—	Ultrasound receiver transfer function in the fast-time frequency domain
$H_s(f)$	—	Transfer function of the ultrasound transmitter-receiver cascade in the fast-time frequency domain
$H_{tx}(f)$	—	Ultrasound transmitter transfer function in the fast-time frequency domain
k	—	Radar wavenumber
k_x	—	Spatial frequency or Doppler-wavenumber domain for range x
k_y	—	Spatial frequency or Doppler-wavenumber domain for cross-range y
k_u	—	Spatial frequency or Doppler wavenumber domain for synthetic aperture, u
L	—	Half-size of the synthetic aperture
L_s	—	Half-size of the in-orbit elevation aperture; The size of the in-orbit elevation aperture is $2L_s$

M	—	Number of synthetic aperture samples
M_z	—	Number of in-orbit elevation samples
N	—	Number of fast-time samples
N_z	—	Number of elevation samples that satisfies the Nyquist sampling theorem
$p(t)$	—	Transmitted radar signal
$P(f)$	—	Fourier transform of the transmitted radar signal
PRF	—	Pulse Repetition Frequency in slow-time
PRI	—	Pulse Repetition Interval in slow-time
P	—	Number of orbits/passes in the multipass SAR configuration is $P+1$
R	—	Range
$R(s_p, z)$	—	Radial range from the pth sensor on the in-orbit elevation-aperture to a target at some elevation z.
$r_n(u)$	—	Radial range from the radar to the nth target as a function of synthetic aperture position
r_{min}	—	Minimum radial range from the radar to the swath
r_{max}	—	Maximum radial range from the radar to the swath
$s(t, u)$	—	Echod SAR signal from the target area
$s(f, u)$	—	One-dimensional Fourier transform of SAR signal with respect to fast-time
$S(f, k_u)$	—	Two-dimensional Fourier transform of SAR signal with respect to fast-time and slow-time
$S_n(f, k_u)$	—	Two-dimensional Fourier transform of the nth target SAR signal with respect to fast-time and slow-time.
$s_m(t, u)$	—	Fast-time matched-filtered echoed signal
$S_m(t, k_u)$	—	One-dimensional Fourier transform of fast-time matched-filtered SAR signal with respect to slow-time
$s_0(t, u)$	—	Reference SAR signal
T_c	—	Reference fast-time point
T_e	—	Fast-time sampling end time for SAR signal
T_p	—	Radar signal pulse width
T_s	—	Fast-time sampline start time for SAR signal
u	—	Synthetic aperture domain
X_0	—	Half-size of the target area in the range domain
X_{0max}	—	Maximum half-size of the range swath; $2X_{0max}$ is the maximum size of the range swath
X_c	—	Mean range of target region; centre of the target area in the range direction
x	—	Range domain
x_n	—	Range of the nth target
y	—	Cross-range or azimuth domain
y_n	—	Cross-range of the nth target
Y_0	—	Half-size of the target area in the cross-range domain
Z_0	—	Half-size of the illuminated elevation extension of the scene.

λ	—	Wavelength
σ_n	—	Reflectivity of the *nth* target
ω	—	Fast-time frequency in radians per second
$\phi_{d(y)}$	—	Antenna beam divergence angle in the cross-range direction
ξ_p	—	Elevation spatial-frequency
η	—	Elevation super-resolution factor
η_{up}	—	Upper limit on elevation super-resolution factor
ε	—	Compressive sampling regularization parameter
$\zeta_0(t)$	—	Ideal complex range (fast-time) profile in the fast-time domain
$\zeta_0(f)$	—	Ideal complex range (fast-time) profile of the target region in the fast-time frequency domain
$\zeta(t)$	—	Reconstructed complex range profile of the target region in the fast-time domain as a result of bandlimited transmitted pulse
$\zeta(f)$	—	Reconstructed complex range profile of the target region in the fast-time frequency domain
$\sigma_0(t)$	—	Ideal amplitude function of complex range profile of the target region
$\sigma(t)$	—	Reconstructed amplitude function of the complex range profile of the target region
θ_s	—	Radar squint angle
θ_v	—	View angle of the radar in multipass configuration
$\varphi_0(t)$	—	Ideal phase function of complex range profile
$\varphi(t)$	—	Approximate phase function of the complex range profile
Φ	—	Measurement matrix
Ψ	—	Sparsity matrix
ρ_z	—	Super-resolution elevation sampling interval $\rho_z = {\triangle_z}/{\eta}$
$\gamma(x, u, z)$	—	Three-dimensional scene reflectivity function
$\gamma(z)$	—	One-dimensional scene reflectivity function in the elevation domain
$\tilde{\gamma}(z)$	—	One-dimensional scene reflectivity function in the elevation domain including the residual video phase, $\tilde{\gamma}(z) = \gamma(z)e^{-j\frac{2\pi}{\lambda x}z^2}$
$\hat{\gamma}(z)$	—	Finite resolution estimate of the scene reflectivity function in the elevation domain
$\triangle_s$	—	In-orbit elevation sampling interval
$\triangle_t$	—	Fast-time sampling interval
$\triangle_u$	—	Synthetic aperture sampling interval
$\triangle_\tau$	—	Slow-time sampling interval or Pulse Repetition Interval (PRI)
$\triangle_x$	—	Range resolution
$\triangle_y$	—	Cross-range resolution
$\triangle_z$	—	Elevation sampling interval; Nominal 3-dB elevation resolution

Nomenclature

2D—Two-dimensional

3D—Three-dimensional

ADC—Analog to Digital Converter

Azimuth—Angle in a horizontal plane, relative to a fixed reference, usually north or the longitudinal reference axis of the aircraft or satellite.

Baseline—The axis over which multiple SAS/SAR acquisitions are made for tomographic reconstruction.

Beamwidth—The angular width of a slice through the mainlobe of the radiation pattern of an antenna in the horizontal, vertical or other plane.

CS—Compressive Sampling or Compressive Sensing

Cross-range—Direction orthogonal to the radar's line of sight.

DAQ—Data Acquisition

Doppler frequency—A shift in the radio frequency of the return from a target or other object as a result of the object's radial motion relative to the radar.

Elevation—Direction orthogonal to range and azimuth.

LabVIEW—(Laboratory Virtual Instrumentation Engineering Workbench) System design platform and development environment for a visual programming language from National Instruments.

NI—National Instruments

PRF—Pulse repetition frequency.

Range—The radial distance from a radar to a target.

Synthetic Aperture Radar (SAR)—A signal-processing technique for improving the azimuth resolution beyond the beamwidth of the physical antenna actually used in the radar system. This is done by synthesizing the equivalent of a very long sidelooking array antenna.

Synthetic Aperture Sonar (SAS)—A signal-processing technique for improving the azimuth resolution beyond the beamwidth of the physical transducer actually used in the sonar system. This is done by synthesizing the equivalent of a very long sidelooking array transducer.

Swath—The area on earth covered by the antenna signal.

VI—Virtual Instrument

Chapter 1

Introduction

1.1 Background

Synthetic Aperture Radar (SAR) is a technique used to obtain two-dimensional (2D) images of the electromagnetic backscattering properties of any terrain. The SAR system is an active microwave remote sensing system which consists of a transmitter and receiver mounted on a platform. The platform can be either airborne or spaceborne. As the platform flies over a terrain of interest, electromagnetic (EM) pulses are transmitted from the transmitter toward the ground. Objects or targets on the ground reflect part of these incident pulses back to the receiver. These reflected pulses are sampled and processed via signal processing techniques to generate high resolution 2D images representing the reflectivity properties of objects in the illuminated scene. High resolution in the range (cross-track) direction is obtained by compressing a transmitted large bandwidth frequency modulated pulse called a chirp [4]. High resolution in the azimuth (along track or cross-range) direction is obtained by synthesizing a large aperture by coherently processing the data received by a sizeable real antenna as it moves along the acquisition track [4]. A single pass of the SAR system provides a 2D SAR image that represents the backscattering properties of the illuminated three-dimensional (3D) scene onto a 2D plane (range-azimuth), hence targets at the same range but different elevations are collapsed onto the same resolution cell in the 2D SAR image. Multi-pass systems are capable of producing 3D images of the scene [5] which can be useful in military surveillance.

Three-dimensional imaging is already in existence with the use of Interferometric SAR (InSAR) in which the phase difference between the signals acquired by two or more antennas with different view angles are used to generate a 3D altimetric profile of the imaged scene [5, 4]. However InSAR has a few short-comings namely: firstly it implicitly assumes the scattering mechanism to appear only at the surface level and as a consequence does not provide a scatter distribution along the height direction [5, 4]. Secondly it performs phase unwrapping which is a nonlinear process that often turns out to be rather critical due to the presence of steep regions of the imaged scene (foreshortening and layover) [4]. A new approach to SAR interferometry is the polarimetric SAR interferometry

where it is possible to separate different scattering mechanisms within the same azimuth-range SAR resolution cell. It however becomes impossible to separate contributions of the same scattering mechanism that spans different heights [5, 6].

SAR tomographic techniques, or sometimes referred to as multi-baseline SAR, allow the generation of 3D images such that for each azimuth and range position provides an estimation of the scattering distribution along the elevation direction [6]. It involves forming a second synthetic aperture in the elevation direction similar to the one formed in the azimuth direction, which is accomplished by using several multi-pass acquisitions on the same scene. However two problems arise from this technique which need to be addressed:

1. The number of acquisitions in the elevation direction for elevation aperture synthesis is much lower compared to the number of acquistions used in azimuth aperture synthesis. Also, the acquisition points may be unevenly spaced.

2. The spatial resolution in the height direction (orthogonal to the ground plane) is limited by the range and elevation (orthogonal to range) resolutions.

The first problem mentioned above introduces a degree of ill-conditioning in the processing step required for the image focusing along the elevation direction that may generate severe ambiguities and numerical instabilities in the elevation imaging process [5, 6]. Several techniques can be used to solve this problem including spectrum estimation techniques such as truncated singular value decomposition (TSVD) [7] and spectral estimation techniques, the non-uniform sampling theorem [6], or by exploiting the compressive sampling technique [5]. The TSVD-based tomography works on single-look images with full-range and azimuth resolutions and follows a deterministic approach. It is however not possible to achieve elevation resolutions higher than the nominal resolution obtainable from a given elevation aperture size. The techniques based on the non-uniform sampling theorem is based on the bandlimited properties of the signal acquired along the elevation direction and places a restriction on the maximum sampling interval and the minimum samples average density [5]. An improved elevation resolution is obtainable by employing spectral estimation techniques. These however work on multilook images which have decreased range and azimuth resolutions. Also they are based on statistical models and require a prior knowledge or estimation of the number of interfering scatterers and of the unknown covariance matrix which can be estimated from multilook data [5]. In summary so far, most of the aforementioned techniques are not capable of producing elevation-focused images with resolutions higher than the nominal resolution obtainable with the given elevation aperture size.

However, the tomographic technique based on compressive sensing [5] works on single-look SAR images obtained from a minimal number of measurements while still capable of enhancing the elevation resolution achievable with a given aperture extent. It is based on the premise that only a small number of scatterers with different elevations are present in the same range-azimuth resolution cell [5]. It is based on the compressive sampling

theorem which allows for data acquisition and super-resolution using only few signal samples [8, 9, 10].

Compressive sensing (CS) is a model-based framework for data acquisition and signal recovery based on the premise that a signal having a sparse representation in one basis can be reconstructed from a small number of measurements collected in a second basis that is incoherent with the first. If this condition is satisfied then the sparse signal of interest can be exactly reconstructed in high signal-to-noise ratio (SNR) by solving a convex optimization problem specifically by l_1-norm minimization. The tomographic technique based on CS theory has been dubbed tomographic CS focusing (TCS) [5].

1.2 Statement of Problem and Hypothesis

Synthetic Aperture Sonar (SAS) is similar to SAR in terms of the overall aim. However there are differences in both implementations as well as signal processing considerations in each of them. Synthetic aperture radar uses electromagnetic signals that travel as fast as light[1]. On the other hand synthetic aperture sonar uses acoustic signals that travel at the speed of sound depending on the medium in which they propagate[2]. Many of the differences between SAR and SAS are therefore associated with the differences in speed of propagation [11, 12]. SAS may be used in underwater surveillance and variations in temperature and salinity of seawater causes reflection and bending of ray paths thus making SAS processing slightly more tasking. Despite the differences in these two concepts, the principle of synthetic aperture imaging is the same in both that is to store successive echoes obtained from either radar or sonar carried by a moving platform and to coherently process them to synthesize a long aperture and thereby achieving high resolution images [11].

A short-coming of synthetic aperture imaging is the inability to resolve targets in the elevation direction. However in certain applications like the mining industry, it is important to resolve targets in a 3D volume. 3D synthetic aperture imaging requires acquisition of SAR or SAS data of the same scene over multiple baselines or different viewing angles. The major challenge of elevation imaging is that the nominal resolution in the height direction is low because it depends on the number of baselines which is usually very low. The task of attaining super-resolution in the elevation direction is usually left to the algorithm used to process the acquired data. A number of such algorithms have been developed such as the TSVD and the compressive sensing/sampling techniques. Several studies have been conducted in the area of 3D SAR imaging using compressive sampling. The aim of this dissertation therefore is to extend the 3D SAR imaging to the sonar domain by investigating the possibility of air-based 3D SAS imaging using an ultrasonic transducer array and the compressive sensing technique.

[1] Speed of light, $c = 3 \times 10^8\,\mathrm{m}s^{-1}$

[2] Speed of sound in air is approximately $340\,\mathrm{m}s^{-1}$. Speed of sound in water is approximately $1500\,\mathrm{m}s^{-1}$

1.3 Objectives

The main objective of this thesis is to design and implement a 3D SAS processor that is based on the compressive sensing. In order to achieve this, the following tasks will be performed:

- Simulate 3D SAS imaging using compressive sensing in MATLAB.
- Design an ultrasonic transducer array and transceiver circuitry for data acquisition of real ultrasonic signals.
- Design a control system for the data acquisition using LabView.
- Perform signal processing on acquired data to form 3D SAS images.
- Take readings from test scenes to demonstrate 3D SAS imaging.
- Compare experimental results with simulations.
- Draw conclusions and make recommendations for possible future work in this area.

It must be pointed out that the focus of this work was to investigate the effectiveness of compressive sampling as a signal processing technique in SAS tomography and the development of the hardware was solely to demonstrate the use of this technique in handling real data. Due to time constraints on the project, the investigation was limited to the use of SAS data acquired at evenly-spaced baselines.

1.4 Plan of Development

This dissertation is divided into chapters and a summary of each chapter is presented below.

Chapter 2 discusses 2D synthetic aperture radar imaging theory, by describing the different SAR modes, the SAR geometry. The 2D SAR data model is derived and explained. The SAR image processing issues are also discussed such as pulse type, matched filtering, range focusing and azimuth focusing. The chapter also reviews the main focusing algorithms used to obtain SAR images.

Chapter 3 extends the theory behind 2D SAR image formation to develop a 3D model for 3D SAR image formation based on the compressive sampling technique.

Chapter 4: presents an overview of the 3D SAS processor that was designed including different parameters of the systems that were chosen. It also describes the design considerations in building the 3D SAS processor such as the transducer beamwidth measurements, inverse filtering, circuit diagrams etc.

Chapter 5 describes methodology used in the 3D SAS data acquisition and processing simulation, such as the simulated pulse, the target area, the processing algorithm used etc.

Chapter 6 presents the results of the 3D SAS simulation to illustrate the results expected from the actual SAS system.

Chapter 7 presents the results obtained from the 3D SAS processor with 3D SAS images that demonstrate the effectiveness of the compressive sampling approach to SAS image reconstruction. A results of the simulated and real data are also compared.

Chapter 8 draws conclusions and makes recommendations for possible areas of improvement and future work.

Chapter 2

Principles of Synthetic Aperture Radar

2.1 Introduction

RADAR is an acronym for radio detection and ranging, and in the early days it was used for the detection and range determination of targets. Nowadays radar systems are capable of a wide range of tasks like tracking, imaging, identification, classification and isolation fo targets in the presence of unwanted interference from various sources.

Basically a radar system consists of a transmitter, an antenna, a receiver, a signal processor and some form of display device [13, 14]. The radar transmits electromagnetic (EM) waves in the radio frequency range towards a target of interest and receives these electromagnetic waves when they are reflected by the target[1]. Fig. 2.1 shows a simplified representation of a radar system. The transmitter generates the high power EM wave. The antenna radiates the wave generated by the transmitter towards the target through the atmosphere.

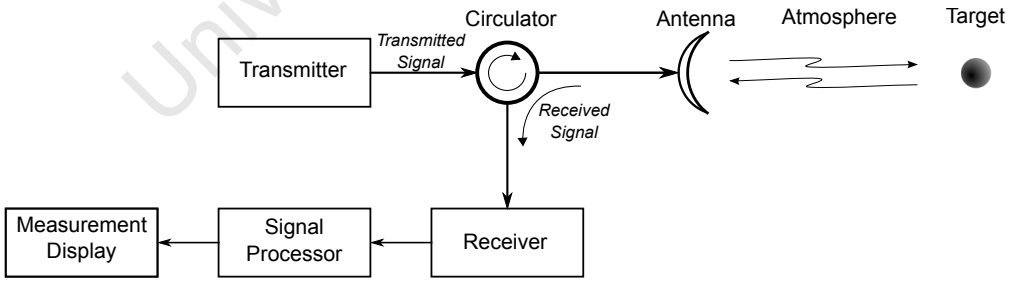

Figure 2.1: A basic representation of a radar system.

The EM wave which strikes the target is called the incident wave and part of it gets reradiated from the surface of the target. The reradiated wave called the reflected wave from both the target and any other object in the antenna's illumination region travels back to the antenna. The antenna detects and captures the reflected wave and applies it to the receiver circuit. The receiver circuit usually consists of a downconverter and

[1] A target is any object of interest that the radar illuminates. Terrain usually consisting of objects covering a large area such as vegetation, lakes, rivers, roads, etc can also be targets depending on the aim of the radar operator [13].

an analog to digital converter (ADC). The downcoverter is used to convert the received signal from the radio frequency down to an intermediate frequency (IF), while the ADC converts the received signal which is a continuous wave into a digital signal. The signal processor analyses the received signal to extract useful information about the target and displays its results or measurements on a display unit [14]. The circulator enables the transmitter and receiver to be connected to the same antenna, while providing isolation between the transmitter and receiver [14]. The reason for this is the transmitter generates the high power transmit signal and this signal is propagated into the atmosphere by the antenna. The transmitted signal is intercepted by the target as well as other objects in the illuminated region, such that the power of signal which is reflected back into the antenna is smaller than the power transmitted. The receiver is thus designed to detect small power levels, so without proper isolation, the high powered signal from the transmitter could damage sensitive receiver components [14].

The EM wave radiated by the antenna travels a distance R to the target. This distance is called the range. The reradiated waves from the target travel the same distance back to the antenna. It is possible to determine this range by measuring the time t it takes for the EM wave to travel to the target and back. Since EM waves travel as fast as light then the range to a target is given by [14, 13]:

$$R = \frac{ct}{2} \tag{2.1}$$

where c is the speed of light, t is the time in seconds for the two-way travel and R is the range in metres to the target.

The accuracy in calculating this range depends on the accuracy in measuring the time for the two-way travel [13].

Angular information of detected targets can be obtained by the use of directional antennas. These antennas radiate EM energy in a known direction. The energy reflected from the target to the antenna depends on the direction or pointing of the antenna [13]. The accuracy in determining the angular position of a target depends on the antenna beamwidth and the accuracy in measuring the antenna pointing [13]. With both range and angular information it is possible to locate a target in a 3D space [13].

Apart from target range measurement, a radar should be able to distinguish or resolve two or more closely spaced targets, this property is called resolution. Resolution of a radar is the minimum distance by which two targets must be separated so that they can be distinguished either in range, angle or doppler frequency [14]. Range resolution, δR is determined by the effective radar pulse width, T_p [15]. For a simple unmodulated pulse [14] for example a cosine wave of pulse width T_p, the range resolution is given by

$$\delta R = \frac{cT_p}{2} \tag{2.2}$$

so two targets separated by more than δR in range will be resolved in range while two

targets separated by less than δR will not be resolved in range. For example, for two targets to be resolved in range using a 1 millisecond long pulse, the targets must be at least 150 km apart. In practice we have no control over the spacing of targets, but we can choose the pulse width to be used in the radar to enable us tp achieve finer resolution. To achieve a finer resolution of say 0.15m, the pulse would have to be 1ns long. However it will be shown in a later section that short pulses have little energy which makes detection difficult [14].

Modern radar systems have shifted emphasis from detection and tracking of targets to the application of major radar functions such as two- and three-dimensional mapping, imaging, collision avoidance, military surveillance, earth resource exploration to mention a few. A typical imaging radar provides a two-dimensional mapping of targets in an illuminated volume, thus it represents a three-dimensional volume of targets in a two-dimensional image hence there is no resolution in the height dimension. Radar resolution in such case is made up of range resolution and azimuth or cross-range resolution [13]. Azimuth resolution refers to the ability of a radar to resolve two or more targets in the azimuth direction. In conventional radar, azimuth resolution is proportional to the divergence angle of the antenna beam pattern in the azimuth direction. For a planar shaped antenna, the divergence angle is inversely proportional to the antenna aperture size or the frequency of the radar [1]. Thus the larger the antenna aperture, the smaller the azimuth beamwidth and the higher the azimuth resolution. However there is a limit on the physical size of an antenna aperture [13]. This is the motivation for the use of synthetic aperture radar today. With synthetic aperture radar, high azimuth resolution can be achieved by signal synthesis.

2.2 SAR as a Large Synthetic Antenna Aperture

As mentioned earlier, in conventional side-looking side-aperture radar (SLAR) systems, azimuth resolution is proportional to the antenna's azimuth divergence angle, which is given by

$$\phi_{d(y)} = \frac{\lambda}{D_y} \tag{2.3}$$

where λ is the wavelength of the transmitted signal and D_y is the length of the real-aperture antenna parallel to the flight path.

Two targets at the same range, R can only be resolved in the azimuth direction if they are not both illuminated by the radar beam at the same time [3]. This means that the azimuth (or cross-range) resolution of the SLAR is

$$\Delta_y \approx R\phi_{d(y)} \approx R\frac{\lambda}{D_y} \tag{2.4}$$

Equation2.4 suggests that to obtain high resolution in the cross-range direction at a given

frequency, a very long antenna is required. The design and manufacture of such long antenna encounters problems that make their realization impossible.

SAR can be thought of as a way of creating a very large antenna without actually using a large physical antenna, by a process called aperture synthesis. In aperture synthesis, a small antenna with a widebeam (large divergence angle) is moved in a straight line (SAR baseline), such that the total distance travelled by the antenna is equivalent to a very large antenna of length $2L$ [14] having a divergence angle of

$$\phi_{d(y)} \approx \frac{\lambda}{2L} \tag{2.5}$$

and a cross-range resolution of

$$\Delta_y \approx R\phi_{d(y)} \approx R\frac{\lambda}{2L} \tag{2.6}$$

Thus a higher cross-range resolution is achieved by collecting data over longer distances. This view of SAR can however become problematic when the synthetic aperture length $2L$ becomes comparable with the range R from the scene. In this situation the scene of interest is in the near field of the synthetic aperture and can lead to spherical wavefronts at the aperture and other distortions.

2.3 SAR as a Signal Processing Problem

The SAR concept can be viewed as a linear signal processing system where a region of interest called a target region is composed of multiple scatterers each with reflectivity coefficients σ_n (n = 1, 2, 3,...). The target region can be modelled as a linear system with an impulse response given by equation (2.7) called the ideal target function [1]

$$f_0(x,y) = \sum_n \sigma_n \delta\left(x - x_n, y - y_n\right) \tag{2.7}$$

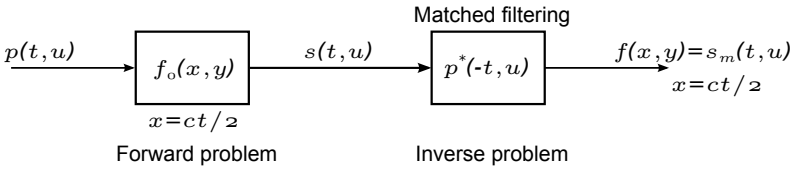

Figure 2.2: SAR concept as a linear system.

The SAR concept can thus be viewed as trying to determine the impulse response of the target region from the knowledge of its input [1], this is the inverse problem in Fig. 2.2. Image synthesis in SAR is composed of a two step procedure moving among three domains namely:

1. The object space: the domain in which a scene is represented by the coordinates

of the targets in the scene and their reflectivity coefficients. It is modelled as the impulse response of (2.7).

2. The data space: the domain in which radar measurements from the scene are represented . This is identified as the forward problem in Fig. 2.2.

3. The image space: this is final synthetic image.

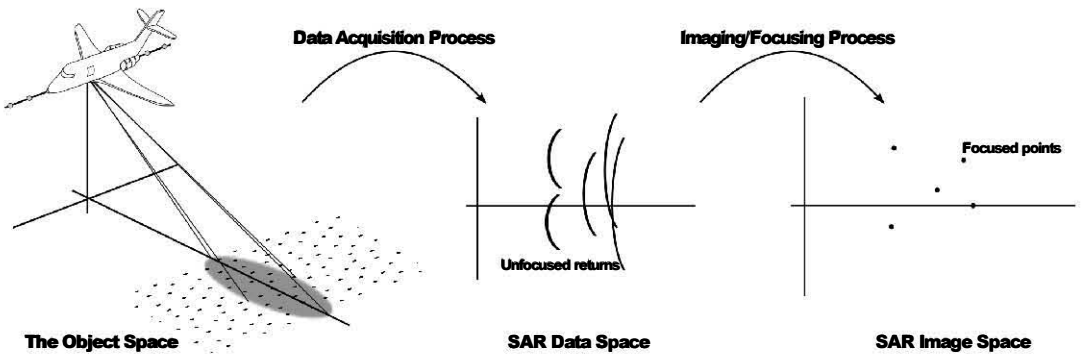

Figure 2.3: SAR signal processing domains.

The two main steps of SAR imaging are

1. Data acquisition: Detection, sampling and storing of echo signals from the target region at each position along the flight path. Parameters such as sampling rate, pulse repetition frequency, etc. chosen at this stage all affect the quality of the final SAR image. The process of data acquisition transforms the object space into the data space [14], illustrated in Fig. 2.3.

2. Image formation: This process is the transformation from the data space to the final SAR image (see Fig. 2.3). It is identified as the inverse problem in Fig. 2.2. It involves matched filtering the acquired data with the predicted responses from the scene of interest [14]. Many algorithms have been developed to perform SAR image formation such as the range-doppler algorithm [1], time-domain backprojection [1], two-dimensional fourier transforms [1], chirp scaling algorithm [16, 17] to mention a few. All these algorithms are exact implementations of or approximations to filtering that is matched to a point target response [14].

2.4 SAR modes

There are three common SAR imaging modes (Fig. 2.4). These modes differ mainly in the manner in which data acquisition is carried out: the stripmap mode, the spotlight mode and scan mode. In stripmap mode, the antenna maintains a fixed radiation pattern so that the area illuminated by the antenna is a strip which runs parallel to the direction of flight [13, 18, 1]. In spotlight SAR, a specific target area is constantly illuminated as the

radar moves in a straight line. This is achieved by mechanical or electronic beam-steering where the physical radar radiation pattern is focused on the same target area while the aircraft moves along the synthetic aperture. This mode of SAR is known to achieve very high resolution [13, 18, 1]. In scan-SAR mode, the radiation beam pattern is steered to illuminate a strip of a scene at any angle [13].

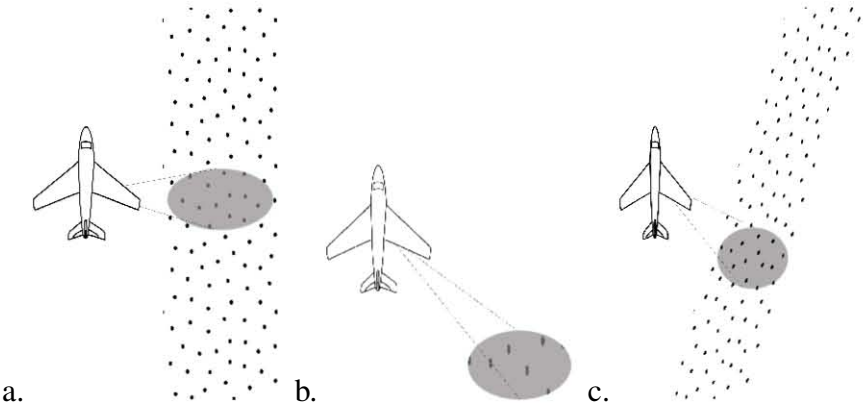

Figure 2.4: SAR modes: a. Stripmap-SAR. b. Spotlight-SAR. c. Scan-SAR.

This work focuses on the stripmap SAR mode and all derivations and discussions will be built up around this SAR mode.

2.5 The Radar Pulse

The choice of the pulse used in SAR is very important in achieving high resolution images. To achieve high resolutions, it would be logical to use very short monotone (single-frequency) signals called pulses. However short pulses contains very little energy that echoes from targets in the scene will have very low signal-to-noise ratio; making it very difficult for the radar receiver to detect them. Also there are practical limits on the peak signal power that can be transmitted. Modern SAR systems solve this problem by using long-duration phase-coded pulses such as the now universally accepted chirp pulse [3].

The chirp pulse is one whose instantaneous frequency is a linear function of time. In other words the frequency of a chirp pulse varies linearly over a given bandwidth with time. The analytic representation of the chirp pulse is

$$p(t) = a(t)e^{j2\pi\left(\beta t+\frac{1}{2}\alpha t^2\right)} \tag{2.8}$$

$$a(t) = \begin{cases} 1 & \text{for } 0 \leq t \leq T_p \\ 0 & \text{otherwise} \end{cases}$$

where T_p is the duration of the pulse.

The phase of the chirp pulse is a quadratic function of time and is given by

$$\phi(t) = 2\pi\left(\beta t + \frac{1}{2}\alpha t^2\right) \tag{2.9}$$

The instantaneous frequency of the chirp pulse is the derivative of its phase

$$f_{chirp}(t) = \frac{1}{2\pi}\frac{d}{dt}\phi(t) = \beta + \alpha t \tag{2.10}$$

α is the rate at which the frequency of the chirp pulse changes and is called the chirp rate. With $\alpha > 0$ the instantaneous frequency (Equation 2.10) is an increasing function of time and the chirp is said to be upsweep [1]. The minimum and maximum frequencies of the chirp pulse are

$$min(f_{chirp}(t)) = f_{chirp}(t)\mid_{t=0} = \beta \tag{2.11}$$

$$max(f_{chirp}(t)) = f_{chirp}(t)\mid_{t=T_p} = \beta + \alpha T_p \tag{2.12}$$

Hence the range of frequencies over which the chirp pulse is defined or the support band is given by

$$\begin{aligned} f &\in \left[min(f_{chirp}(t)), max(f_{chirp}(t))\right] \\ f &\in [\beta, \beta + \alpha T_p] \end{aligned} \tag{2.13}$$

The centre frequency of the chirp pulse is

$$f_c = \beta + \frac{(\beta + \alpha T_p) - \beta}{2} = \beta + \frac{1}{2}\alpha T_p \tag{2.14}$$

its total bandwidth $B_t = \alpha T_p$ and its baseband bandwidth is

$$\pm B_0 = \pm\frac{1}{2}\alpha T_p \tag{2.15}$$

The baseband bandwidth of the chirp pulse is the bandwidth after basebanding which is half the total bandwidth of the chirp signal. Basebanding of the analytic chirp pulse involves multiplication with a complex phasor $e^{j2\pi f_c t}$ in the time domain such that the chirp pulse becomes centred on 0 Hz in the frequency domain.

The advantage of the chirp pulse is that the duration of a chirp pulse can be varied independently of the desired bandwidth [19] and since the energy of a pulse is proportional to its length, the energy in the chirp signal can be set by generating a chirp pulse of appropriate length. This is also useful in obtaining the range profile of the imaged scene. The range profile of the scene is obtained by a process of matched filtering which will be discussed later in detail. According to matched filter theory, a high signal to noise ratio at the output of the matched filter is obtained when the input signal has a high energy. Thus high SNR gains are obtainable by using the long-duration chirp pulses as a sensing signal.

The length of the chirp pulse or pulse width T_p is constrained by the target region. The pulse width must not be longer than the round-trip delay between the radar and the closest point of the target region.

$$T_p \leq \frac{2R_{min}}{c}$$

where c is the speed of light and R_{min} is the distance from the radar to the closest point of the target region.

This requirement is particularly stringent for systems where a single antenna is used as both transmitter and receiver becauses echoes from closest targets that arrive at the antenna before the end of a transmit cycle will be lost if the duration of the pulse is longer than round-trip delay to the targets.

The time-bandwidth product of a chirp pulse is defined by

$$TBWP = B_t T_p = 2B_0 T_p = \alpha T_p^2 \tag{2.16}$$

where B_t is the total bandwidth over which the chirp pulse is swept. The time-bandwidth product of the chirp pulse affects the magnitude spectrum of the matched filter response. For chirp pulses with large TBWP > 100, their magnitude spectrum is approximately rectangular, hence the magnitude spectrum of the matched filter response is approximately rectangular and has a 3-dB bandwidth of approximately B_t [3].

2.6 Two-dimensional SAR Imaging

The synthetic aperture radar technique aims at obtaining a representation of the electromagnetic reflectivity properties of a target region in the multi-dimensional spatial domain of range (x), cross-range (y) and height (z). In this section we will develop the strip-map SAR model in the two-dimensional spatial domain of slant-range and cross-range. This domain is represented by (x,y). The term range will however still be used to refer to the slant-range in this section.

Consider a target region composed of stationary reflectors at coordinates given by (x_n, y_n) where $n = 1,2,3...$ Consider also a radar located at $(0,u)$ where u is used to represent the flight path of the radar and is called the synthetic aperture domain. Note that the coordinate y and u may not necessarily be the same depending on the properties of the target region and the mode of SAS that is implemented. The radar can either be broadside (Fig. 2.5) or squint (Fig. 2.6). In the broadside configuration, the radar radiates pulses orthogonal to the direction of flight. This is usually the case when the target region of interest is centred around the origin that is the cross-range interval $y_n \in [-Y_o, Y_o]$ [1]. In the squint configuration, the target region is positioned in the following interval $y_n \in [Y_c - Y_o, Y_c + Y_o]$.

The broadside target area is thus a special form of the squint target area with $Y_c = 0$.

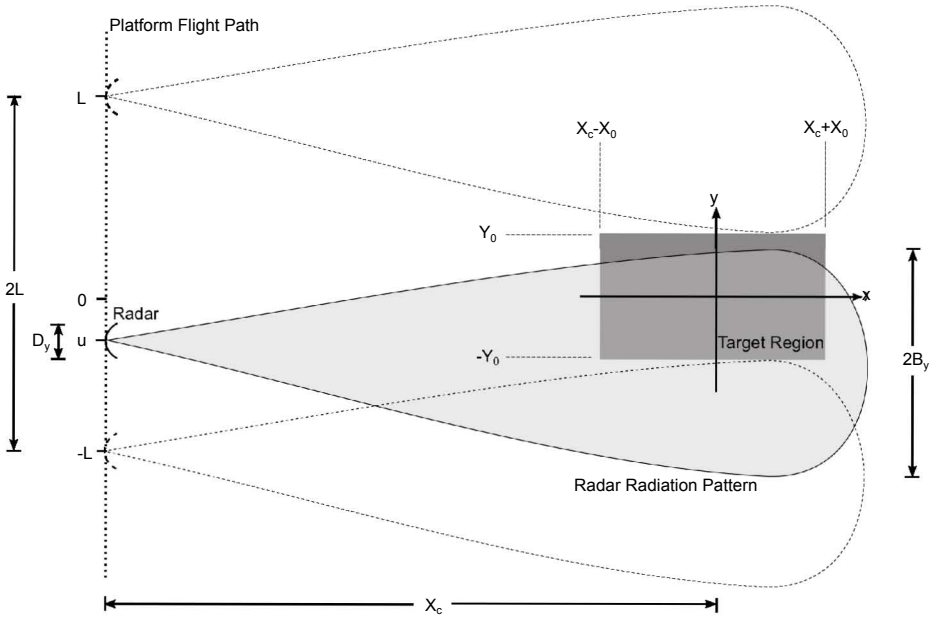

Figure 2.5: SAR imaging geometry for a broadside target area.

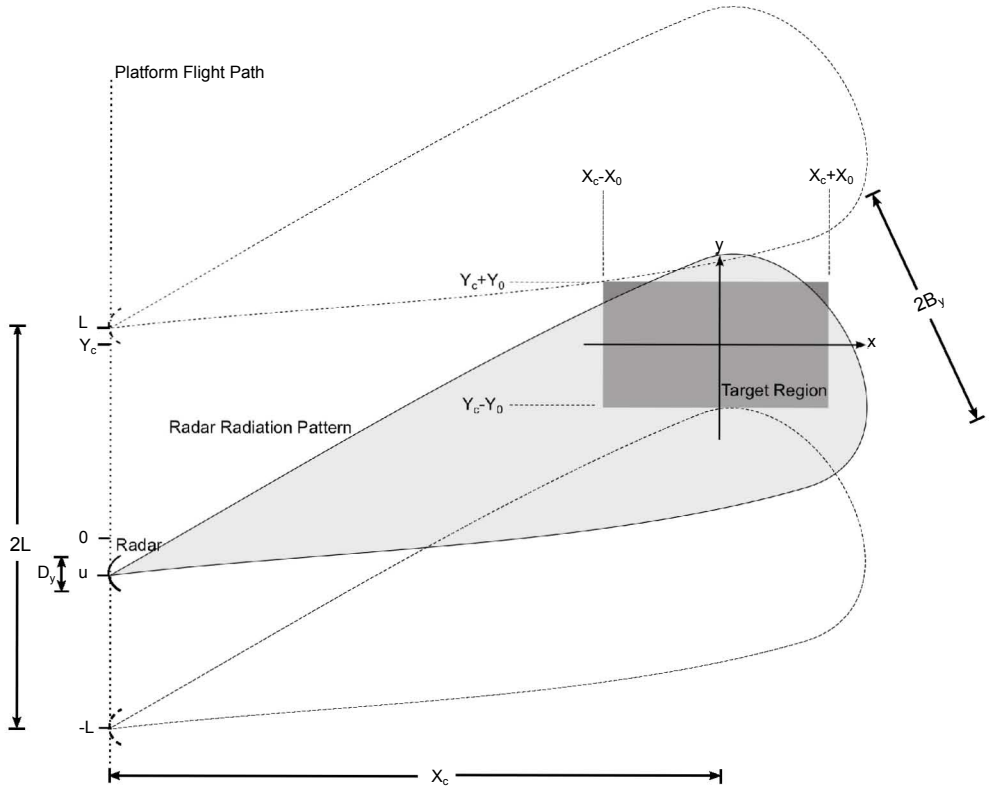

Figure 2.6: SAR imaging geometry for a squint target area.

The radiation pattern of the radar for its transmit-receive mode remains fixed as it moves along the synthetic aperture. The radiation pattern of the radar is represented mathematically as a function in the spatial domain (x,y) at a given fast-time frequency, f [1]. The radiation pattern at an arbitrary synthetic aperture position, u is given by

$$h_r(f,x,y-u) \tag{2.17}$$

It can also be expressed as an amplitude and phase function

$$h_r(f,x,y-u) = a_r(f,x,y-u)\,e^{-j\phi_r(f,x,y-u)}$$

The radiation pattern depends on the type of radar and its physical dimensions. If the antenna is an ideal transmitting/receiving element which transmits/receives equally in all directions, the radiation pattern is omni-directional and the amplitude function is inversely proportional to the square of the distance.

A given reflector at (x,y) is observable to the radar when the radar is in the following synthetic aperture interval

$$u \in [y-B_y, y+B_y]$$

where B_y is the radar half-beamwidth which is approximated by the mainlobe of the radar transmit-receive amplitude pattern $a_r(f,x,y)$ in the cross-range domain. Given the divergence (angular spread) of the radar beam, $\phi_{d(y)}$ the half beamwidth is given by

$$B_y = x\tan\phi_{d(y)}$$

Assuming that the target region we wish to image falls within the cross-range interval

$$y \in [-Y_o, Y_o]$$

where Y_0 is a chosen constant. Then the synthetic aperture interval over which the stripmap SAR data is acquired is

$$u \in [-L, L]$$

where $L = B_y + Y_o$.

2.6.1 The Stripmap SAR signal

The radar illuminates the target region with a long duration (large bandwidth) pulsed signal $p(t)$. The reflected pulses which are received by the radar is a function of time, t and the instantaneous position of the radar relative to the nth target at (x_n, y_n) and is given

by equation (2.18).

$$\begin{aligned} s(t,u) &= \sum_n \mathscr{F}_{(f)}^{-1}\left\{a_n(f,x_n,y_n-u)\,h_r(f,x_n,y_n-u)\right\} \circledast p(t-t_n) \qquad (2.18)\\ &= \sum_n \mathscr{F}_{(f)}^{-1}\left\{a_n(f,x_n,y_n-u)\,h_r(f,x_n,y_n-u)\right\} \circledast p\left(t-\frac{2\sqrt{x_n^2+(y_n-u)^2}}{c}\right) \end{aligned}$$

where t_n is the round-trip delay from the nth target to the radar, $a_n()$ is the nth target amplitude pattern and $\mathscr{F}_{(f)}^{-1}(\cdot)$ is the one-dimensional inverse Fourier transform with respect to the fast-time frequency f.

The target amplitude pattern $a_n(f,x_n,y_n-u)$ determines the observability of the nth target by the radar. If the nth target is an ideal omni-directional reflector then the target amplitude pattern is a constant σ_n and synthetic aperture interval over which the radar can "see" the target is given by

$$u \in [y_n - B_{yn}, y_n + B_{yn}] \qquad (2.19)$$

where

$$B_{yn} = x_n \tan\phi_{d(y)} \qquad (2.20)$$

is the radar half-beamwidth at the range x_n and $\phi_{d(y)}$ is the divergence angle of the radar beam. Note that this interval varies with the coordinates of the target as well as the radar parameters.

The motion of the radar along the flight path creates the synthetic aperture, u thus forming the 2D measured signal $s(t,u)$. The SAR signal can be expressed as a function of fast-time frequency f at any given synthetic aperture position u by taking the one-dimensional Fourier transform of the SAR signal (Equation 2.18) with respect to fast-time t.

$$\begin{aligned} s(f,u) &= \mathscr{F}_{(t)}\left\{s(t,u)\right\}\\ &= P(f)\sum_n a_n(f,x_n,y_n-u)\,h_r(f,x_n,y_n-u)\,e^{-j2k\sqrt{x_n^2+(y_n-u)^2}} \qquad (2.21) \end{aligned}$$

where $k = 2\pi f/c$ is called the wavenumber. The point along the synthetic aperture that corresponds to the cross-range coordinate of a nth target in the scene i.e the point where $u = y_n$ is called the closest point of approach of the radar to the nth target. At this point the round-trip delay to the target is minimum.

The time domain, t is usually called the fast-time domain because it corresponds to the time delay associated with the propagation of the echoed signals which propagate as fast as light. The fast-time frequency domain is denoted with f. The synthetic aperture domain, u is the spatial counterpart of the temporal slow-time domain, τ. The slow-time domain is so called because it corresponds to the velocity of the platform (aircraft or satellite) on which the radar is borne. The speed of the platform is much slower than the speed of the propagation of the echoed signals. Given a radar velocity of v_r, the slow-time

domain in the units of time in seconds is a scaled version of the synthetic aperture domain, u and is given by $\tau = \frac{u}{v_r}$. The spatial frequency of u is called the Doppler wavenumber, k_u, while the temporal frequency domain of τ is called the Doppler frequency domain.

The SAR measurement $s(t,u)$ is made at regularly spaced intervals of u with a sample spacing of $\triangle_u$. At each interval of the synthetic aperture domain, the radar illuminates the target area with short bursts of the signal $p(t)$. The number of bursts transmitted per second is called the pulse repetition frequency (PRF). The interval between two consecutive bursts is called the pulse repetition interval (PRI). The PRF and PRI are related by

$$PRI = \frac{1}{PRF}$$

The sample spacing in the synthetic aperture domain ($\triangle_u$) can be related to the speed of the radar platform and the slow-time sample spacing via

$$\begin{aligned} \triangle_u &= v_r \triangle_\tau \\ &= v_r \times PRI \\ \triangle_u &= \frac{v_r}{PRF} \end{aligned}$$

The pulse repetition frequency is a very important quantity in determining how far a target needs to be inorder to be located for accurate mapping in the final SAR image.

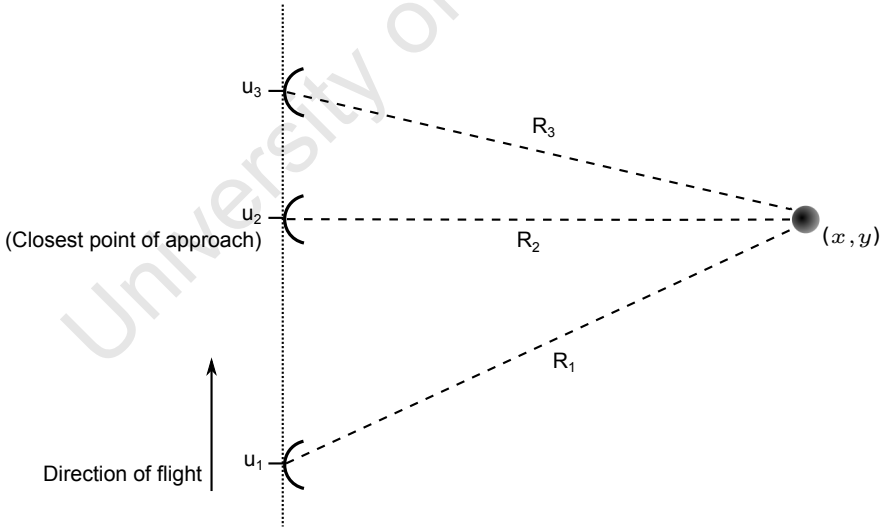

Figure 2.7: Shows how a targets SAR signature is measured in the $s(t,u)$ domain [1].

Consider a target located at (x,y) with a radar moving along a synthetic aperture, u (Fig. 2.7). Three arbitrary synthetic aperture positions u_1, u_2 & u_3 are shown with u_2 being the closest point of approach for this specific target. In a target region consisting of multiple targets, the closest point of approach will vary with each target. The range to the target in Fig. 2.7 at any synthetic aperture point u_i (i = 1, 2, 3...) is given by

$$R_i = \sqrt{x^2 + (y - u_i)^2}$$

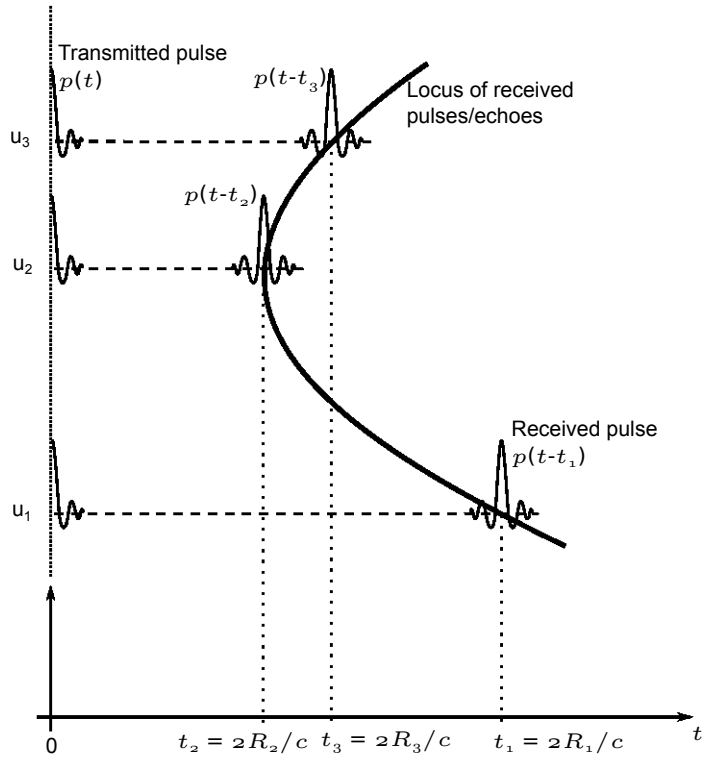

Figure 2.8: Half-hyperbolic locus of SAR echoes from a target [1].

The time it will take a signal to propagate from the radar to the target and back to the radar, or the round-trip fast-time delay is given by

$$t_i = \frac{2R_i}{c} = \frac{2\sqrt{x^2 + (y-u_i)^2}}{c}$$

In general the range to a target to located at (x,y) from any point on the synthetic aperture u is given by

$$R = \sqrt{x^2 + (y-u)^2}$$

and the corresponding round-trip delay is given by

$$t = \frac{2\sqrt{x^2 + (y-u)^2}}{c}$$

which is the equation of a half-hyperbola in the (t,u) domain

$$\begin{aligned} \frac{c^2}{4}t^2 &= x^2 + (y-u)^2 \\ \frac{c^2}{4}t^2 - (y-u)^2 &= x^2 \quad \text{for} \, t \geq 0 \end{aligned} \tag{2.22}$$

The locus of the SAR echoes from the target in Fig. 2.8 follows a half-hyperbola as given in (2.22). The pulse transmitted $p(t)$ at fast-time $t = 0$ from each synthetic aperture position is received again at the radar as a delayed version of the transmitted signal, $p(t -$

$t_i)$ where i = 1, 2, 3, ...

In practice it is not possible to generate a very narrow pulse $p(t)$ with sufficient energy to illuminate a target area. Most often the pulse $p(t)$ has a relatively long duration in the fast-time so visualizing the hyperbolic locus of the echoed signal in the (t,u) domain may be difficult. However by a process of pulse compression [3, 1], the visualization of the SAR (t,u) domain data as well as the signal to noise ratio of the echo signal can be improved.

The point target response (2.18 with $n = 1$) is dispersed in both the fast-time domain as a result of the structure of the transmitted pulse and in the synthetic aperture domain as a result of the multiple pulses that arrive at the target as the radar travels past it. The aim of synthetic aperture imaging is to "compress" these signals to a point, just like the target [3]. However in practice the finite bandwidth of the transmitter and the finite length of the synthetic aperture limits us to an approximate version of the target of nonzero width in the two-dimensional image. This can be explained further by looking at the frequency domain of the signals under consideration. The impulse response of the ideal target function (2.7) has infinite bandwidth in both the fast- and slow-time frequency domains (Fig. 2.9). The physical radar however has finite bandwidth and consequently the SAR acquisition process effectively "filters" all but a finite band of the target return frequencies. So by linear processing of the radar signals only a finite bandwidth approximation to the observed target region can be obtained .

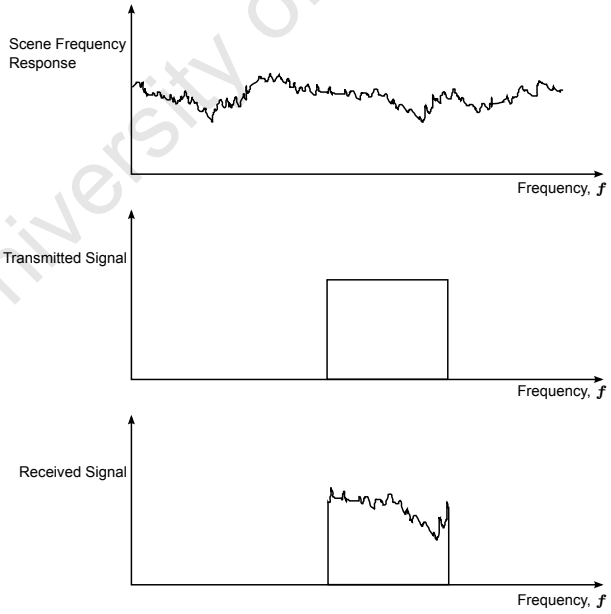

Figure 2.9: Frequency domain illustration of the "compressed" 2D SAR imaging.

The SAR image formation concept is thus to compress to a point the bandlimited radar returns of a point target inorder to reconstruct an approximate form of the ideal target function (2.7). This process is a two-dimensional compression problem (a fast-time compression and a slow-time compression). However by assuming that the range to a target remains constant during the time of one pulse width [3], this two-dimensional problem

can be decoupled into a sequence of two one-dimensional compression operations in each acquisition domain: one in the fast-time (range) domain and one in the slow-time (synthetic aperture) domain.

2.6.2 Range Compression

Recall the received signal of a SAR system (2.18). At each synthetic aperture position, the received signal is a sum of delayed chirp pulses from the individual targets in the target region. Because of the imaging geometry, SAR image formation can be split into two dimensions: focusing in the range direction and focusing in the cross-range direction. Compression in the range direction is carried out by compressing the received signal such that the long-duration time-delayed chirp pulses become a much narrower pulses. Range compression can be performed by implementing the matched filter [3, 14, 2] or the deconvolution filter [2, 3]. Some other methods for range compression include the Deramp or dechirp processing [1, 12], the step transform [12, 3]to mention a few.

Matched Filter

A matched filter is one whose filter coefficients are "matched" to the signal it is designed to detect, such that the maximum possible SNR is maintained [14]. Given an input signal $x(t)$ distorted by additive noise $n(t)$ with a power spectral density $S_{ni}(f)$ referred to the input of the matched filter. The matched filter $h(t)$ is designed such that the output signal to noise ratio (2.23) at an instant in time t_m is maximized [2].

$$\frac{|y(t_m)|^2}{\left|\overline{n_o(t)}\right|^2} = \frac{\text{Peak signal power at time } t_m}{\text{Average output noise power}} \tag{2.23}$$

For the case of white noise with a flat power spectral density $S_{ni}(\omega) = \eta/2$ the matched filter (Fig. 2.10) can be shown to be [3, 14, 2]:

$$\begin{aligned} h(t) &= kx^{\star}(-t+t_m) \\ H(f) &= kX^{\star}(f)\, e^{-j2\pi f t_m} \end{aligned} \tag{2.24}$$

where k is an arbitrary constant scaling factor which can be set to $k = 1$.

For the general case of noise that does not have a flat power spectral density, $S_{ni}(f)$. The matched filter (2.25) can be split into two filtering stages (Fig. 2.11). The first stage (2.26) is called a pre-whitening filter and it is designed to flatten out the power spectral density of the noise [2]. The second stage (2.27) is designed as a matched filter for white noise

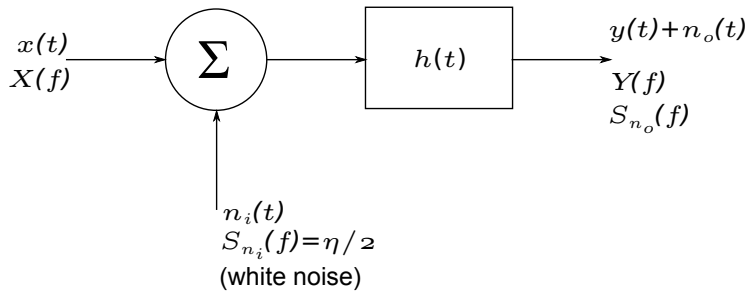

Figure 2.10: Matched filter [2].

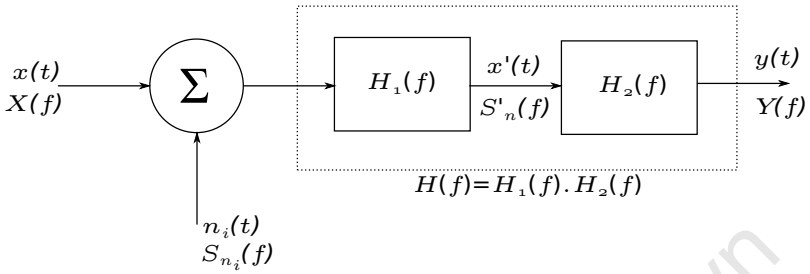

Figure 2.11: Matched filter for general case [2].

using matched filter theory with the output of the pre-whitening filter as the input signal.

$$H(f) = H_1(f)H_2(f) = \frac{X^{\star}(f)}{S_{ni}(f)} e^{-j2\pi f t_m} \tag{2.25}$$

$$H_1(f) = \frac{1}{\sqrt{S_{ni}(f)}} \tag{2.26}$$

$$H_2(f) = X'^{\star}(f)\, e^{-j2\pi f t_m} \tag{2.27}$$

The mathematical equations and derivations in the following section are adapted from [3]. The most common pulse used in transmission in SAR systems is the linear FM pulse (or chirp pulse).

$$p(t) = \cos\left(2\pi f_c t + \pi\alpha t^2\right), \qquad |t| \leq \frac{T_p}{2} \tag{2.28}$$

The received signal at the radar from point targets with ideal target reflectivity function σ_n at each point along the synthetic aperture is the impulse response (assuming a radar with omni-directional radiation pattern)

$$s(t,u) = \sum_n \sigma_n \cos\left[2\pi f_c\,(t-t_n) + \pi\alpha\,(t-t_n)^2\right] \tag{2.29}$$

The amplitude scaling factor $1/r_n^2 = 1/\sqrt{x_n^2+y_n^2}$ has been absorbed into the target reflectivity constant σ_n. The fast-time delay $t_n = \frac{2r_n(u)}{c}$ with

$$r_n(u) = \sqrt{x_n^2 + (y_n - u)^2} \tag{2.30}$$

Equation 2.29 can now be written to explicitly show the dependence on the synthetic

aperture coordinate, u.

$$s(t,u) = \sum_n \sigma_n \cos\left[2\pi f_c\left(t - {}^{2r_n(u)}/_c\right) + \pi\alpha\left(t - {}^{2r_n(u)}/_c\right)^2\right] \qquad \left|t - {}^{2r_n(u)}/_c\right| \leq {}^{\mathrm{T_p}}/_2 \tag{2.31}$$

The extent of the synthetic aperture over which $s(t,u)$ is effectively non-zero depends on the duration of illumination of the point target by the radar (2.19). At all points along the synthetic aperture, the received signal $s(t,u)$ is sampled in the fast-time domain at a little above the Nyquist rate which is typically greater than twice the bandwidth B_t of the radar pulse centred around the carrier.

Range compression then involves compressing the function (2.31) which is spread out in the fast-time domain, to a pulse at fast-time $t_n = {}^{2r_n(u)}/_c$. This process is repeated for every received signal over the range of synthetic aperture needed to form an image. The first stage of this operation is complex basebanding or I-Q demodulation which begins by a Fourier transformation of the received data $s(t,u)$ with respect to the fast-time, t. The complex basebanding is performed by deleting the negative or positive frequency components of the spectrum and shifting the remaining half to centre on zero frequency [3] (Fig. 2.12).

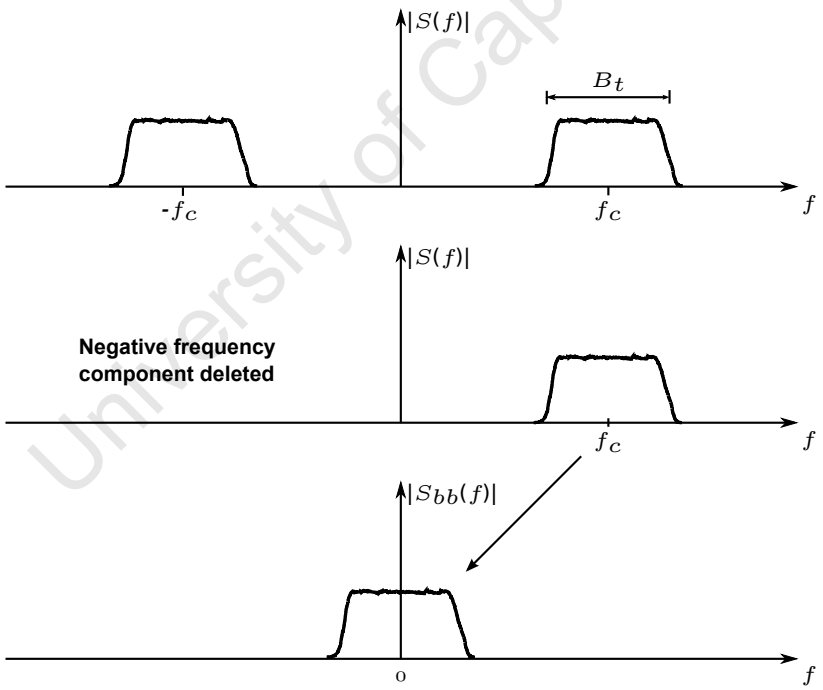

Figure 2.12: Complex basebanding or I-Q demodulation [3]

The resulting spectrum $S_{bb}(f,u)$ of the basebanded data now corresponds to the complex time function $s_{bb}(t,u)$ for each synthetic aperture position, u which from (2.31) is (ignoring an inessential constant):

$$s_{bb}(t,u) = \sum_n \sigma_n e^{-j\frac{4\pi}{\lambda}r_n(u)} e^{-j\pi\alpha\left(t-\frac{2}{c}r_n(u)\right)^2}, \qquad \left|t - \frac{2}{c}r_n(u)\right| \leq {}^{\mathrm{T_p}}/_2 \tag{2.32}$$

The fast-time Fourier transform of (2.32) is given by

$$\begin{aligned} S_{bb}(f,u) &= \mathscr{F}_{(t)}\left\{\sum_n \sigma_n e^{-j\frac{4\pi}{\lambda}r_n(u)} e^{j\pi\alpha(t-2r_n(u)/c)^2}\right\} \\ S_{bb}(f,u) &= \sum_n \sigma_n e^{-j\frac{4\pi}{\lambda}r_n(u)} e^{-j\frac{4\pi f}{c}r_n(u)} \mathscr{F}\left\{e^{j\pi\alpha t^2}\right\} \end{aligned}$$

Observe that the last exponential on the right hand side of the above equation is the complex basebanded version of the transmitted pulse (Equation 2.28), whose spectrum (except for a constant amplitude factor) is given by [3]

$$P_{bb}(f) = e^{j\frac{\pi}{4}\mathrm{sgn}(\alpha)} e^{-j\frac{\pi f^2}{\alpha}} \qquad |f-f_c| < |\alpha|T_p/2 = B_t/2 = B_0 \tag{2.33}$$

Therefore the spectrum of the basebanded impulse response is

$$S_{bb}(f,u) = e^{j\frac{\pi}{4}\mathrm{sgn}(\alpha)} e^{-j\frac{\pi f^2}{\alpha}} \sum_n \sigma_n e^{-j\frac{4\pi}{\lambda}r_n(u)} e^{-j\frac{4\pi f}{c}r_n(u)} \qquad |f-f_c| < B_0 \tag{2.34}$$

Chirp signals with large time-bandwidth product $B_t T_p = |\alpha| T_p^2$ (for example > 100) have rectangular amplitude spectrum. So assuming that the transmitted pulse has a large time-bandwidth product and consequently a constant amplitude spectrum, the compression filter is the matched filter

$$H_{mf}(f) = P_{bb}^{\star}(f) = e^{-j\frac{\pi}{4}\mathrm{sgn}(\alpha)} e^{j\frac{\pi f^2}{\alpha}} \qquad |f-f_c| < B_0 \tag{2.35}$$

Applying the filter to the baseband signal spectrum of Equation 2.34 gives

$$S_{mf}(f,u) = S_{bb}(f,u)H_{mf}(f) = \sum_n \sigma_n e^{-j\frac{4\pi}{\lambda}r_n(u)} e^{-j\frac{4\pi f}{c}r_n(u)}, \qquad |f-f_c| < B_0 \tag{2.36}$$

The corresponding matched filter output in the time domain is given by

$$s_{mf}(t,u) = B_t \sum_n \sigma_n e^{-j\frac{4\pi}{\lambda}r_n(u)} \mathrm{sinc}\left(\pi B_t\left(t - \frac{2r_n(u)}{c}\right)\right) \tag{2.37}$$

where $B_t = |\alpha| T_p$ is the transmitted pulse bandwidth and $\mathrm{sinc}(x) = \frac{\sin(x)}{x}$. Thus the output of the matched filter is a sum of time-shifted sinc functions. The time shift is dependent on the range to the particular point target which the sinc function represents.

The fast-time width of a sinc function in $s_{mf}(t,u)$ is $\delta t = \frac{1}{B_t}$ and is the result of range compression. The pulse width of the range compressed data is equivalent to a 3-dB range resolution of

$$\triangle_x = \frac{c}{2B_t} \tag{2.38}$$

For signals with small time-bandwidth products (say > 20), the amplitude spectrum of the range compressed signal is not exactly rectangular but still have the form $\mathrm{sinc}(x)$ in the

the time domain without sacrificing resolution provided the appropriate matched filter is used [3].

The collection of these pulses over the synthetic aperture constitutes the data for cross-range compression.

Deconvolution Filter

Range compression via the deconvolution filter can be described from the view point of the linear system model. The aim of range compression is to obtain the scene (or target region) impulse response in the range direction which is sometimes referred to the range profile at each synthetic aperture position u. This is the forward problem of Fig. 2.13. Consider the ideal complex range profile $\zeta_0(t)$ with an amplitude $\sigma_0(t)$ and phase $\varphi_0(t)$

$$\zeta_0(t) = \sigma_0(t)e^{j\varphi_0(t)} \tag{2.39}$$

Assume a pulse $p(t)$ modeling the transmitted signal of the SAR system is fed into the linear system $\zeta_0(t)$ which models the scenes ideal impulse response in the range direction at a given synthetic aperture position u. The output of the system, which is the received signal at the radar after basebanding is given by

$$s_{bb}(t) = \zeta_0(t) \circledast p(t) \tag{2.40}$$

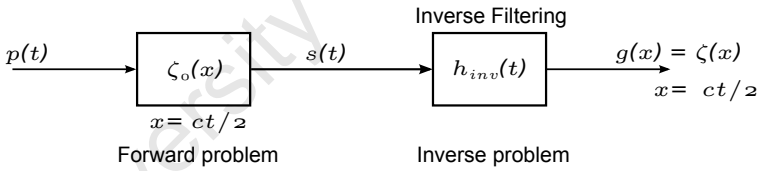

Figure 2.13: Forward and inverse problem for range compression.

Thus if we could design a linear filter $h_c(t)$ such that $p(t) \circledast h_c(t) = \delta(t)$, then we can recover the ideal range profile $\zeta_0(t)$ of the scene at a given synthetic aperture position. This is the inverse problem of Fig. 2.13. This might seem a difficult problem to solve in the time domain. By transforming the received signal $s_{bb}(t)$ to the frequency domain the problem does not look so daunting afterall (2.41).

$$S_{bb}(f) = \zeta_0(f)P(f) \tag{2.41}$$

From Equation 2.41 we see that the appropriate compression filter is[2]

$$H_c(f) = \frac{1}{P(f)}, \qquad P(f) \neq 0 \tag{2.42}$$

[2]Note that the matched filter $P^{\star}(f)$ and the inverse filter $1/P(f)$ are the same as long as the amplitude spectrum of $P(f)$ is unity or at least constant for example in a the linear FM pulse with large time-bandwidth product [3].

since $H_c(f)P(f) = 1$ in the signal band. This kind of filter is the "deconvolution filter" or the "inverse filter". It can also be thought of as a "spectral reconstruction" filter as it reconstructs the spectrum of the impulse response of the scene [2].

$$\begin{aligned} G(f) &= S_{bb}(f)H_c(f) = \zeta_0(f)P(f)\frac{1}{P(f)} = \zeta_0(f) \\ g(t) &= \mathscr{F}^{-1}\{G(f)\} = \zeta_0(t) \end{aligned}$$

In practice, the transmitted signal $p(t)$ is bandlimited, that is $|P(f)| \neq 0$ over a finite range of frequency. This makes the problem of finding the compression filter $H_c(f)$ ill-posed [3] as any solution will be non-unique. This can be solved by adding the condition that the filter $H_c(f)$ have zero amplitude outside the signal band that is

$$H_c(f) = \begin{cases} \frac{1}{P(f)} & -B_0 \leq f \leq B_0 \\ 0 & \text{elsewhere} \end{cases} \tag{2.43}$$

This operation results in a bandlimited version of the range profile $\zeta(t)$ which is an approximate version of the ideal range profile $\zeta_0(t)$.

$$\begin{aligned} G(f) &= \zeta(f)rect\left(\frac{f}{B_t}\right) \\ g(t) &= \zeta(t) \circledast B_t \text{sinc}\left(\pi B_t t\right) \\ g(t) &= \sigma(t)e^{-j\varphi(t)} \circledast B_t \text{sinc}\left(\pi B_t t\right) \end{aligned} \tag{2.44}$$

Hence the spectral reconstruction filter is the convolution of the sinc(x) with the impulse response of the scene. Consequently, the recovered impulse response will be a smeared version of the actual impulse response. Note that output of the deconvolution filter (2.44) is similar to the output of the matched filter (2.37). The 3-dB width of the sinc function is $\delta t = \frac{0.89}{B_t}$ [2] which corresponds to a range resolution of

$$\triangle_x = \frac{0.89c}{2B_t} \tag{2.45}$$

and is the result of range compression via inverse filtering [2].

Sidelobes and Filter Weighting

With the "ideal" reconstruction filter (2.43) one is able to reconstruct the complex reflectivity profile $\zeta(x)$ ($x = ct/2$) in view of the radar with the best resolution possible by linear processing [3]. However the reconstruction comes with high sidelobes. The first sidelobes of (2.44) are 13dB lower than the mainlobe. So if a target is 13-dB weaker than an adjacent target which is one resolution cell away, it's response will be masked by the sidelobe of its neighbour. The high sidelobes are a result of the rectangular structure of

the amplitude spectrum of the reconstruction filter (2.43). By applying a smooth tapering function (window function) to the amplitude spectrum so that the edges of the band gradually fall to zero, the sidelobes can be reduced. This however comes at a cost of degraded resolution as the mainlobe of the filter output broadens (Fig. 2.14).

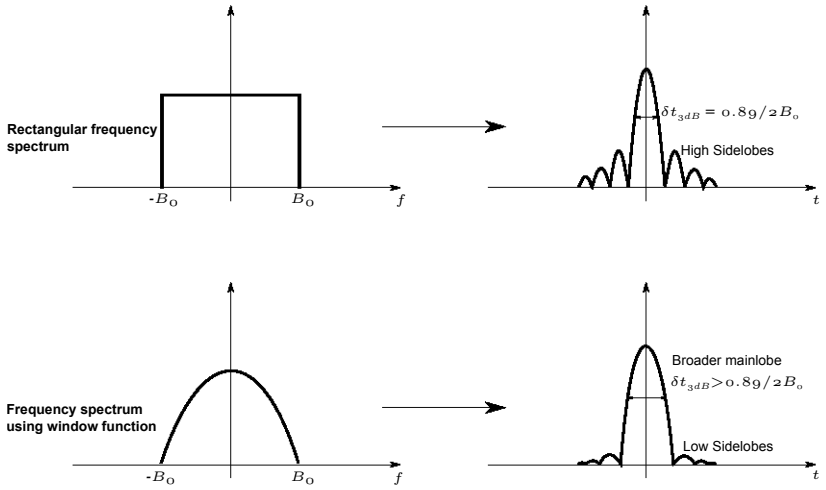

Figure 2.14: The effect of filter weighting on resolution [2].

The window function can be applied in the frequency domain so that the output spectrum of the reconstruction filter incorporating the window function becomes

$$G(f) = S_{bb}(f)H_c(f)W(f)$$

where $W(f)$ is the window function.

There are many window functions commonly used [2]. The Hamming window (2.46) for example is able to suppress the first sidelobe to -41dB below the mainlobe peak. It has a mainlobe broadening factor of 1.5 compared to that of a uniform spectral weighting [2]. The Hann window is another type of window which is able to suppress the first sidelobe to -31dB below the mainlobe peak and a mainlobe broadening factor of 1.6.

The Hamming window is:

$$W(f) = 0.54 + 0.46\cos\left(\frac{2\pi f}{B_t}\right) \tag{2.46}$$

The Hann window is:

$$W(f) = 0.5 + 0.5\cos\left(\frac{2\pi f}{B_t}\right) \tag{2.47}$$

over the interval $-B_0 \leq f \leq B_0$.

Choosing the right filter

In practice the deconvolution filter is often the better filter to employ than the matched filter for the following reasons [2]:

1. **Better-shaped output response:** The inverse filter in combination with a window function provides a processed point target response with low sidelobes identical to $\mathscr{F}^{-1}\{W(f)\}$. The loss in SNR as a result of windowing to reduce the sidelobes is not a bad trade-off for the improvement in the shape of the response. Using the matched filter alone does result in an optimized SNR however, the output response contains high sidelobes. Windowing can be applied to the output of the matched filter but the result will not be a perfect response.

2. **Compensation for transducer/system effects:** In practice, the received signal spectrum is modified by the transducer since it has its own frequency response as well as the system effects. Therefore the received signal spectrum will be distorted in both amplitude and phase which could significantly worsen the sidelobe levels at the output of the filter. Inverse filtering can compensate for these distortions by including the frequency response of the transducer and the system in the filter design, although the bandwidth of the filter has to be carefully set to avoid increase in the noise level at the output.

2.6.3 Azimuth Compression

The mathematical derivations in this section are based on the [3]. Consider the range compressed signal (2.37) which is repeated below with some constants omitted for simplicity.

$$s_{mf}(t,u) = \sum_n e^{-j\frac{4\pi}{\lambda}r_n(u)} \text{sinc}\left(t - \frac{2r_n(u)}{c}\right)$$

For a given synthetic aperture position (say, $u = u_i$) and the nth point target, the peak of $\left|s_{mf}(t,u_i)\right|$occurs at a point in time $t_n = 2r_n(u_i)/c$. At this particular time, the value of $s_{mf}(t,u)$ is

$$s_{mf}(t_n,u_i) = e^{-j\frac{4\pi}{\lambda}r_n(u_i)} \tag{2.48}$$

Collecting all the values of (2.48) from all the synthetic aperture positions where the target is effectively in view of the radar, can be considered to be samples at spatial position u_i of a function of synthetic aperture, u [3].

$$s_{mf}(u) = e^{-j\frac{4\pi}{\lambda}r(u)} \tag{2.49}$$

The values of (2.49) form locus in the two-dimenstional (t, u) plane (Fig. 2.15). The radar returns which were once dispersed in two dimensions have been compressed in one-dimension via range compression. The next operation in order to achieve the point target response is to compress this one-dimensional path to a point at (x_n, y_n) which is the original target position, this is called azimuth compression [3]. This signal (2.49) is the Doppler signal received from the point target as the radar moves past it. The aim of azimuth compression and indeed the aim of the so-called range-Doppler processing

algorithm is effectively to compress the Doppler signature of the target [3].

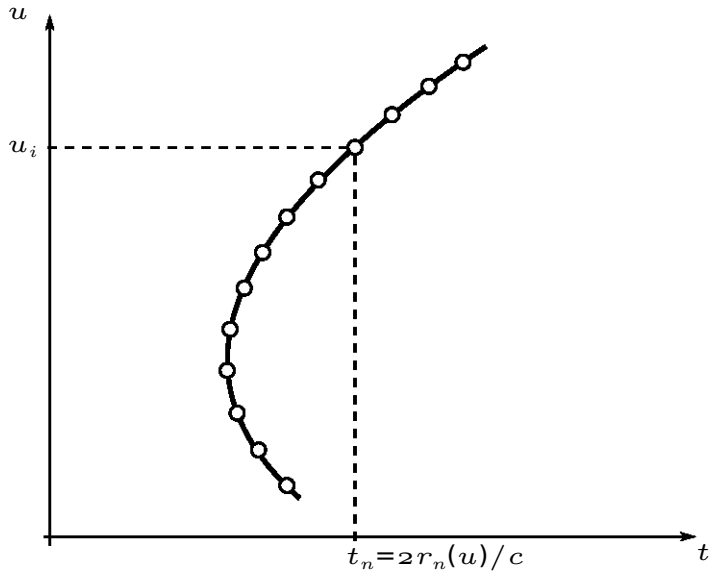

Figure 2.15: Locus of range compressed SAR data from a point target [3].

This compression operation would be implemented as a correlation of the azimuth signal (2.49) with a reference azimuth signal in the time domain. However the challenge to obtaining this reference signal is the fact that the azimuth signal is dependent on $r(u)$ which is a nonlinear function of synthetic aperture u and depends on the target coordinates (x_n, y_n). Thus reference signal used in any instance would be a range-varying reference signal as it would depend on the point in the final SAR image we wish to resolve. Implementing the correlation in the time-domain is computationally inefficient. Considerable processing gains can be achieved by implementing azimuth compression as a matched filter and is the method which is commonly employed [3].

The range $r_n(u)$ to an nth target at the coordinates (x_n, y_n) can be expanded as a Taylor series around $u = y_n$ and is expressed as

$$r_n(u) \approx r_n(y_n) + \dot{r}_n(u - y_n) + \frac{1}{2}\ddot{r}_n(u - y_n)^2 + \ldots \tag{2.50}$$

where $r_n(y_n) = x_n$ is the range to the target when the radar is at closest point of approach that is when $u = y_n$ (2.30).

From the phase of the synthetic aperture signal (2.49) we can obtain the spatial-Doppler frequency and the spatial-Doppler rate

$$\begin{aligned} \phi(u) &= -\frac{4\pi}{\lambda} r(u) \\ \frac{1}{2\pi}\frac{d}{du}\phi(u) &= k_{uD} = -\frac{2}{\lambda}\dot{r}(u) \\ \frac{1}{2\pi}\frac{d^2}{du^2}\phi(u) &= k_{uR} = -\frac{2}{\lambda}\ddot{r}(u) \end{aligned} \tag{2.51}$$

where k_{uD} and k_{uR} are the respective spatial-Doppler frequency and spatial-Doppler rate

associated with the spatial coordinate u.

The leading coefficients of (2.50) can therefore be derived from (2.51) as

$$\dot{r}_n = -\frac{\lambda}{2} k_{uDc}, \qquad \ddot{r}_n = -\frac{\lambda}{2} k_{uR} \tag{2.52}$$

Substituting these values into the synthetic aperture signal (2.49) and assuming that the quadratic expansion of $r(u)$ is sufficient we get

$$s_{mf}(u) = e^{-j\frac{4\pi}{\lambda}x_n} e^{j2\pi\left[k_{uDc}(u-y_n)+\frac{1}{2}k_{uR}(u-y_n)^2\right]} \qquad |u-y_n| < B_{yn} \tag{2.53}$$

where B_{yn} is the spatial extent over which the n*th* target is effectively in view by the radar that is the radar half-beamwidth at range x_n (2.20).

Observe that (2.53) is the equation of a linear FM signal in the spatial coordinate u, with a spatial shift y_n, center frequency k_{uDc} and rate k_{uR} and by a similar technique used in range compression, azimuth compression operation can be realized by using the reference signal [3]:

$$h_c(u) = e^{-j2\pi\left(k_{uDc}u+\frac{1}{2}k_{uR}u^2\right)} \tag{2.54}$$

This operation can be performed as a matched filter over the synthetic aperture for each range x_n of the image. With a time-bandwidth product of 20 or more [3], the correlation operation yields an output whose magnitude is a pulse given by

$$|f(u)| = 2B_{yn}\left|\operatorname{sinc}\left(2\pi k_{uR}B_{yn}\left(u-y_n\right)\right)\right|$$

and the peak of the pulse occurs at $u = y_n$, the cross-range position of the target.

The 3-dB width of the compressed pulse is nominally

$$\triangle_u = \frac{1}{K_B}$$

where

$$K_B = 2\left|k_{uR}\right| B_{yn}$$

is the spatial-Doppler bandwidth [3].

Range Migration

Range migration is a consequence of the SAR operation. It is visible in the fact that the range compressed radar returns at different synthetic aperture positions do not lie in the same range resolution cell in the processed SAR data as was illustrated in Fig. 2.15. Consequently the azimuth signal needed for azimuth compression must be extracted from different range resolution cells. The locus of these range cells in the data is specified by

the curve of $r(u)$ (2.50).

$$\begin{aligned} r_n(u) &= r_n(y_n) + \dot{r}_n(u-y_n) + \frac{1}{2}\ddot{r}_n(u-y_n)^2 \\ &= x_n + \frac{\lambda k_{uDc}}{2}(u-y_n) + \frac{\lambda k_{uR}}{4}(u-y_n)^2 \end{aligned}$$

The linear component of the locus is called the range walk [3] and is the difference in range to a target between the point when the target enters the antenna beam and when it leaves the beam [20]. The quadratic component of the locus is called the range curvature. The sum of the range walk and the range curvature or the difference $\triangle r = r_n(u) - x_n$ constitutes range migration.

The severity of range migration depends on the parameters of the system. In severe cases, range migration would have to be compensated by a range migration compensation operation. Range migration would not need compensation if the maximum distance $|\triangle r|$ is less than a quarter of a range resolution cell, $\triangle_x$ [3]. For the case of a squinted beam with squint angle θ_s, this criterion equates to

$$\frac{\lambda x_n}{\triangle_u}\left(|\sin\theta_s| + \frac{\lambda}{8\triangle_u}\right) < \triangle_x \tag{2.55}$$

For a broadside beam ($\theta_s = 0$), the criterion becomes

$$\left(\frac{\triangle_u}{\lambda}\right)^2 > \frac{x_n}{8\triangle_x} \tag{2.56}$$

There are different azimuth processing techniques that employ some method of range migration compensation. For example in time-domain correlation processing, data to be compressed in azimuth is extracted directly from memory along a curved locus which is dependent on the range to a target x_n.

Depth of Focus

The parameters (k_{uDc}, k_{uR}) of the azimuth reference signal in (2.54) depend on the range x_n. Using an incorrect value of k_{uDc} leads to a loss of signal to noise ratio [3], which may be tolerable to an extent. However if the value of k_{uR} is not the same as the value in the signal being compressed can cause severe loss of azimuth resolution (defocusing) [3]. The range interval over which the same reference signal (2.54) can be used without intolerable defocusing is called the depth of focus [20]. [3] shows that depth of focus is given by

$$|\delta x_n| < \frac{x_n}{4|k_{uR}|B_{yn}^2} = \frac{(\triangle_u)^2}{2\lambda} \tag{2.57}$$

2.6.4 Bandwidth of the SAR signal

The SAR signal (2.18) has a two-dimensional bandwidth. The analysis of the two-dimensional bandwidth is useful to determine the Nyquist sampling rate to avoid aliasing during acquisition and processing of the SAR signal. Also the point spread function of a target depends on the two-dimensional spectral support of the SAR signature of the target as well as the resolution of the SAR system [1].

Assume that the target amplitude pattern is independent of the fast-time frequency and the target coordinates, then the SAR signal of the nth target in the (f,u) is given by

$$s_n(f,u) = P(f)\,\sigma_n a_r(f,x_n,y_n-u)\,e^{-j2k\sqrt{x_n^2+(y_n-u)^2}}$$

By method of stationary phase, the Fourier transform of this signal with respect to slow time is given by [1]

$$S_n(f,k_u) = P(f)\sigma_n A_r(f,k_u)e^{-j\sqrt{4k^2-k_u^2}x_n}e^{-jk_u y_n}$$

The spectral support of $S_n(f,k_u)$ in the Doppler wavenumber domain k_u is set by the support band of the radar amplitude pattern in the same domain [1], so that

$$k_u \in \left[-2k\sin\phi_{d(y)}, 2k\sin\phi_{d(y)}\right] \tag{2.58}$$

Note that this support band is dependent on the physical properties of the radar but independent of the target coordinates. [1] showed that for a radar with planar aperture whose divergence angle is given by

$$\phi_{d(y)} = \arcsin\left(\frac{\lambda}{D_y}\right) \tag{2.59}$$

where D_y is the length of the radar in the cross-range direction and λ is the wavelength, the spectral support in the slow-time Doppler domain is invariant of the radar fast-time frequency and can be approximated by the main lobe of the radar beam pattern which is

$$k_u \in \left[\frac{-4\pi}{D_y}, \frac{4\pi}{D_y}\right]$$

The spectral support of $S_n(f,k_u)$ in the fast-time frequency domain is dictated by the bandwidth of the radar signal which is given by

$$f \in [f_c - B_0, f_c + B_0] \tag{2.60}$$

2.6.5 Data Acquisition Considerations

Fast-time Sampling

Given a radar swath with r_{min} and r_{max} as the closest and farthest radial ranges from the radar respectively. The time of arrival at the receiving radar of the echo from a target at a radial range r_{min} is given by

$$T_s = \frac{2r_{min}}{c} \tag{2.61}$$

The time of arrival of the trailing edge of the echo signal from a target at a radial distance r_{max} is given by

$$T_e = \frac{2r_{max}}{c} + T_p \tag{2.62}$$

where T_p is the pulse width of the transmitted signal.

Thus sampling of the return echoes of the SAR signal should be made within the following fast-time time interval $t \in [T_s, T_e]$. The interval $[r_{min}, r_{max}]$ is called the range gate of the SAR system. The values of r_{min} and r_{max} can be determined from the parameters of the SAR system such as the beamwidth of the radar in the range and cross-range domains.

The fast-time sampling rate of the SAR A/D converter is governed by the Nyquist sampling criterion for bandpass signals [1, 2]: bandpass signals must be sampled at a frequency greater than twice the bandwidth of the signal. Since the bandwidth of the radar signal is B_t the A/D fast-time sample spacing must be

$$\triangle_t < \frac{1}{2B_t} \tag{2.63}$$

The number of fast-time samples within the fast-time interval $t \in [T_s, T_e]$ is

$$N = 2\left\lceil \frac{T_e - T_s}{2\triangle_t} \right\rceil$$

where $\lceil q \rceil$ denotes the smallest integer which is larger than q.

Slow-time Sampling

Recall the slow-time Doppler support of the SAR signal (2.58) at a given fast-time frequency, f.

$$k_u \in \left[-2f \sin\phi_{d(y)}, 2f \sin\phi_{d(y)}\right]$$

This support region is a lowpass signal in the slow-time Doppler domain. At a given fast-time frequency, the Nyquist sampling criterion for lowpass signals such as this requires that the sampling rate in the synthetic aperture u domain be greater than twice the highest

slow-time Doppler frequency component [2, 1], this gives a sample spacing of

$$\triangle_u \leq \frac{2\pi}{4k\sin\phi_{d(y)}} = \frac{\lambda}{4\sin\phi_{d(y)}} \tag{2.64}$$

For a radar with a divergence angle $\phi_d = 90^o$, the sample spacing reduces to

$$\triangle_u \leq \frac{\lambda}{4}$$

For a planar radar aperture with a divergence angle given by (2.59), the slow-time sampling interval is [1]

$$\triangle_u \leq \frac{D_y}{4} \tag{2.65}$$

2.6.6 Image Reconstruction Algorithms

Many algorithms have been developed for SAR image reconstruction and each algorithm is optimized for a given SAR system and geometry [21]. The main aim of the SAR reconstruction algorithm is to compress the SAR radar returns $s(t,u)$ of targets which are dispersed in both fast-time and synthetic aperture domains to a point in the spatial domains of range and cross-range that represents the complex reflectivity function $f(x,y)$ of the targets. A summary of few of these algorithms is given below

The Time Domain Correlation and Time Domain Backprojection

In the time-domain correlation algorithm, the target function $f(x,y)$ is reconstructed on a point-by-point basis by a correlation of the of the SAR signal $s(t,u)$ with a reference SAR signal $s_0(t,u)$ from an ideal point reflector at point of interest [3, 21, 1, 22]. Since the data $s(t,u)$ is sampled, the correlation is executed as a two-dimensional sum over the available discrete values of (t,u).

$$s_m(t,u) = s(t,u) \circledast p^{\star}(-t)$$

where $p^{\star}(-t)$ is the complex conjugate of the time-reversed transmitted signal. The time-domain backprojection algorithm also performs image focusing on a point-by-point basis. In this algorithm, a point is focused by coherently summing the fast-time matched-filtered data $s_m(t,u)$ along the hyperbolic locus formed by a target which is assumed to be located at the point of interest.

To reduce the numerical errors, interpolation is usually carried out on the measured signal $s(t,u)$ both the fast-time and slow-time domains. These algorithms are therefore computationally inefficient and time-consuming, and are mainly used for calibration purposes.

The Exact Transfer Function Algorithm

This is the Fourier domain implementation of the time-domain correlation algorithm. It is the simplest of the Fourier-based algorithms. The measured SAR data is matched-filtered with a reference SAR signal from an ideal point target at the point of interest in the two-dimensional frequency domain.

$$F_n(f,k_u) = S(f,k_u)S_n^{\star}(f,k_u)$$

where $F_n(f,k_u)$ is the two-dimensional Fourier transform of the point spread function of the nth target, $S(f,k_u)$ is the two-dimensional Fourier transform of the SAR signal with respect to slow-time and fast-time and $S_n(f,k_u)$ is the two-dimensional Fourier transform of the nth target SAR signal with respect to fast-time and slow-time.

The inverse Fourier transform of the product gives the point spread function of the nth target at coordinates (x_n,y_n). Processing gains can be obtained by using a common matched filter for a range of points within the same depth of focus. However this introduces phase errors in the reconstructed image which may be intolerable for interferometric and bathymetric processing [21].

The Range-Doppler Algorithm

This algorithm works in the range-Doppler wavenumber domain of the range compressed signal $S_m(t,k_u)$ hence the name range-Doppler. It is a two-step algorithm that involves range migration correction then azimuth compression.

Range migration correction is performed by a k_u dependent time (or range) shift given by [22]:

$$\triangle t \approx -\frac{ck_u^2}{8\pi f_c^2}x$$

where x is the range. For accurate range migration correction, this algorithm requires precise interpolation. If precise interpolation is achieved and a constant range x is used, the range migration correction is equivalent to a k_u-dependent linear phase shift in the two-dimensional Fourier domain [22].

Azimuth compression is performed by a one-dimensional matched filtering in the Doppler-wavenumber domain k_u by a spatial Doppler chirp [22, 21] which is given by

$$e^{j\left(\sqrt{\left(\frac{2\pi f_c}{c/2}\right)^2-k_u^2}x-\frac{2\pi f_c}{c/2}\right)} \approx e^{-j\frac{ck_u^2}{8\pi f_c}x}$$

The merit of this algorithm is that all pixels at the same range can be reconstructed by a single compression in the range-Doppler domain. Thus unlike the previous two algorithms, the range-Doppler algorithm reconstructs the target function on a range line -by-range line basis.

The range-Doppler algorithm works reasonably well with SAR systems that have small squint angles and whose physical antennas have small spatial bandwidth in both the range and Doppler domains. In such systems the range chirp is constant with the slow-time Doppler frequency k_u. However this ceases to be so with large squint and spatial bandwidth systems and the range chirp contains a secondary k_u-dependent term which can be eliminated by a process called secondary range compression (SRC) [23, 22, 21].

The Wavenumber Algorithm

The wavenumber algorithm and its derivatives are derived from the wave propagation theory, although it has been shown that it can also be derived directly from time-domain correlation algorithm [22]. This algorithm has three main steps. First, the range compressed SAR data $s_m(t,u)$ or the raw data $s(t,u)$ is transformed into the fast-time frequency f and Doppler-wavenumber k_u domains via a 2D Fourier transform to give $S_m(f,k_u)$ or $S(f,k_u)$ respectively. Second, there is a change of variables called Stolt mapping where the fast-time frequency domain and the slow-time Doppler domains are transformed into the spatial frequency domains of range k_x and cross-range k_y respectively. This process involves precise interpolation. The Stolt map is given by

$$\begin{aligned} k_x &= \sqrt{4k^2 - k_u^2} \\ k_y &= k_u \end{aligned}$$

where $k = 2\pi f/c$.

Prior to interpolation, a spatial basebanding operation is performed. This process is equivalent to the time domain basebanding which effectively strips a signal of the carrier component. Spatial basebanding is implemented as a phase multiplication (the first exponential in 2.66) which translates the entire swath down to the origin of the spatial coordinates.

$$F(k_x,k_y) = \mathbf{S}\left\{ S(f,k_u)\, e^{j\sqrt{4k^2-k_u^2}X_c} e^{-j2\pi f T_c} \right\} \tag{2.66}$$

where X_c is the range to the centre of the target region, $T_c = 2X_c/c$ and $\mathbf{S}\{\cdot\}$ is the Stolt mapping operator. The second phase function restores the fast-time origin back to the actual fast-time zero that is $t = 0$ [1].

In the third and final operation, the spatial target function $f(x,y)$ is obtained by a two-dimensional inverse Fourier transform of $F(k_x,k_y)$.

This algorithm, just like the range-Doppler algorithm is relatively inefficient because of the need for interpolation which if not precise could lead to numerical errors which degrade the final image quality. There are efficient derivatives of the wavenumber algorithm which do not require interpolation as the interpolation is replaced with a phase multiplication in the fast-time frequency, slow-time Doppler domains. However these algorithms carry restrictions on the size of the swath width relative to the average slant-range and the

relative bandwidth of operation which are not fufilled in most SAS systems [21].

The Chirp-Scaling Algorithm

This algorithm was developed out of the need to eliminate the interpolation process that is common to the range-Doppler and the wavenumber algorithms, which if not performed accurately leads to poor image quality [16]. It combines some features of the range-Doppler and wavenumber algorithms along with some additional features [16] to achieve SAR focusing. It uses the fact that range migration is the result of a k_u-dependent range scaling factor in the range-Doppler domain. This algorithm exploits the linear FM signal structure of the transmitted pulse to reduce the SAR image reconstruction to a sequence of Fourier transformations and phase multiplications. Unlike most algorithms which start processing with the range-compressed data $s_m(t,u)$, the chirp-scaling algorithm begins with the raw SAR data $s(t,u)$ [16, 17, 24]. It starts with a 1D Fourier transform in the synthetic aperture domain of the raw SAR data to yield $S(t,k_u)$. This is then chirp-scaled by multiplying with a mild phase-only frequency chirp. This aim of this operation is to force the range-migration phase term of all reflecting targets to be equal to the range-migration phase term of a reference target. This eliminates the range factor in the range-migration phase term so that range-migration correction can be performed by a single range-invariant phase multiply. The scaled data is then Fourier transformed in the range direction to yield the two-dimensional spectrum $S(f,k_u)$ where bulk range-migration correction, pulse compression and secondary range compression (SRC) are performed. The range-compressed signal is then transformed back into the range-Doppler domain $S(t,k_u)$ where azimuth compression is performed as well as the removal of a residual phase function which was introduced by the previous operations. A final 1D inverse Fourier transform of the data in the slow-time domain and a rescaling of coordinates yields the an estimate of target function $f(x,y)$.

The chirp-scaling algorithm is more efficient than the range-Doppler and wavenumber algorithms as it does not require interpolation. [25] showed that the efficiency of the chirp-scaling algorithm could be improved further by starting with the range-compressed SAR data $s_m(t,u)$ through the fact that the uncompensated SRC chirp in the range-Doppler data is sufficient to accomplish the SAR reconstruction and in a case where the SRC chirp is not sufficient, a differential range chirp could be inserted into the compressed data.

2.6.7 Limitations of SAR Imaging

There are geometric distortions inherent in SAR image formation. These geometric distortions arises primarily from the fact that the SAR is a ranging device which generates a cross-track reflectivity profile based on the radar to target range distance [3]. One such geometric distortion is the target elevation error, where the point spread functions of two or more targets at the same azimuth position but different elevations are placed in the

same range resolution cell of the SAR image because they are at the same range distance from the radar (Fig. 2.16).

Foreshortening is another type of geometric distortion and it occurs when the slope of the terrain of interest is less than the incidence angle of the radar beam [3]. As illustrated in Fig. 2.16, foreshortening causes the slope of segment ab to appear compressed (points a_i, b_i) in the SAR image.

Layover is a geometric distortion that occurs for steep terrain where the slope of the terrain is greater or equal to the incident angle of the radar beam (Fig. 2.16). Because point b appears closer to the radar than point a, the signature (b_i) of point b in the radar image "lays over" that of point a (a_i). This effect is commonly observed in mountainous areas where the top of the mountain is closer in slant-range than its base, so that the point spread function of the mountain's peak appears at a nearer range cell in the SAR image.

Shadowing is an effect which is related to layover. It occurs when a particular target slopes away from the radar at an angle greater or equal to the incident angle of the radar beam (Fig. 2.16). As a result the shadowed region does not reflect any signal back to the radar and will not be visible in the SAR image.

2.7 Comparison between SAS and SAR systems

The aim of any synthetic aperture imaging is to estimate the complex reflectivity function of a terrain of interest. However the parameters of a given systems affects the signal processing techniques employed in reaching this goal. The main differences between SAR systems and SAS systems are summarized below

- Speed of propagation: Radar signals travel at approximately $3 \times 10^8\,\mathrm{m}s^{-1}$ while acoustic signals travel at the speed of sound which depends on the medium of propagation. The speed of sound is approximately $340\,\mathrm{m}s^{-1}$ and $1500\,\mathrm{m}s^{-1}$ [21] in air and water respectively.

- Bandwidth: Most SAR systems are characterized by narrow bandwidth transmissions where the bandwidth is small compared to the centre frequency of operation. SAS systems on the other hand are wideband systems, typically having bandwidths in the kHz range at kHz centre frequencies.

- Platform velocity: Spaceborne SAR travels at speeds up to $7500\,\mathrm{m}s^{-1}$ while SAS travel at usually $1\,\mathrm{m}s^{-1}$ [21].

- Swath width to range ratio: Spaceborne SAR systems usually have a swath width to slant-range ratio of about 1:10. This ratio is about 1:1 in SAS systems.

- Range of propagation: SAR systems are capable of imaging over larger distances in air than their SAS counterparts. For instance the average slant range for spaceborne SAR systems is about 900km and about 500m for underwater SAS.

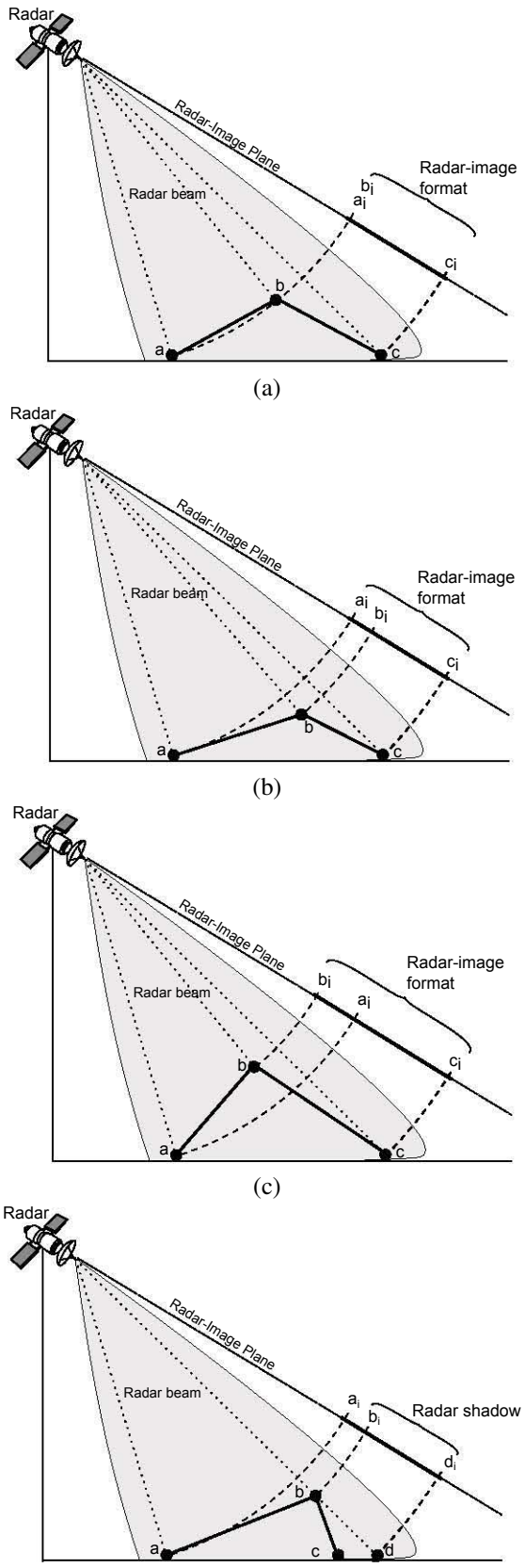

Figure 2.16: Geometric distortions of SAR imaging: a. Target elevation error b. Foreshortening c. Layover d. Shadow

- Processing algorithm: Processing of SAS images requires algorithms that can efficiently process large beamwidth, large bandwidth data which is peculiar to SAS data.

Chapter 3

The SAR Tomography and Compressive Sensing

Single-pass SAR systems generate two-dimensional (2D) SAR images of a given target region. These images only represent a projection of the 3D reflectivity properties of the scene onto the 2D range and cross-range domains. SAR tomography extends the synthetic aperture principle into the elevation domain for 3D imaging by using a stack of SAR data obtained from multiple acquisitions with slightly different viewing angles to reconstruct the reflectivity information of the imaged scene in the elevation direction. Focused 3D images are obtained by spectral analysis of each azimuth-range pixel in the stack as long as the range migration caused by the different viewing angles is much smaller than the range resolution [26, 27]. Various 3D imaging techniques exist such as the use of Interferometric SAR (InSAR) which relies on the use of the phase difference between SAR images acquired from two or more passes over the same scene but slightly different viewing angles [28, 4, 5]. However it requires phase unwrapping of the measured wrapped phase differences that can be critical for areas with large geometric distortions such as foreshortening and layover. Also InSAR assumes that the scattering mechanism appears only at the surface level thus obtaining scatterer distribution along the height direction is not possible. The result of InSAR is only an estimate of the scene digital elevation model in the presence of volumetric scattering [4]. The use of a polarimetric SAR interferometry was proposed by [29]. In this technique, it is possible to resolve different scattering mechanisms within the 2D SAR resolution cell. However imaging of targets with the same scattering mechanism spread out over different heights is impossible. Spectral estimation techniques for 3D imaging techniques have been proposed [30]. With this algorithm it is possible to resolve different scattering mechanisms in the same 2D resolution cell using only a few passes, however is works based on the assumption that only a small number of scatterers are present within the investigated cell.

There are also SAR tomographic techniques which provide an estimation of the reflectivity distribution along the elevation direction [1]. These techniques require an aperture

[1] "Elevation" direction refers to the direction orthogonal to the slant-range plane.

synthesis in the elevation direction which can be performed by using several multipass acquisitions of the same scene [5]. However there are two limitations that must be tackled by these algorithms [5]:

1. The number of acquisitions is usually much lower than is required for full-resolution elevation aperture synthesis and in most practical cases the spacing between the acquisitions will be irregular. This introduces a degree of ill-conditioning in the processing for the image focusing in the elevation directions as the number of unknowns exceeds the number of equations.

2. The spatial resolution in the height direction [2] is limited by the range and elevation resolutions. While the range resolution depends on the transmitted signal bandwidth, the elevation resolution depends on the spatial extent of the synthesized elevation aperture which in most cases is not sufficiently large enough for appreciable resolution.

The first problem mentioned above can be solved by exploiting spectrum estimation strategies such as the truncated singular value decomposition (TSVD) [7] and spectral estimation techniques or the non-uniform sampling theorem [6]. TSVD-based tomography works on single-look (full 2D resolution) images and follows a deterministic approach but cannot achieved elevation resolutions higher than the nominal resolution obtainable with a given elevation aperture size. Spectral estimation techniques allow an increased elevation resolution but use multi-look images which have lower range and cross-range resolutions. They also require an estimate of the number of scatterers and unknown covariance matrix [5]. Other techiques also exist like the aforementioned which work on single-look images but not capable of producing elevation-focused images with a resolution higher than the nominal resolution. However [5] proposed the tomographic compressive sampling techniques (TCS) which enhances the elevation resolution achievable with a given synthesized elevation aperture extent with single-look images. It assumes that a low number of scatterers with different elevations are present in the same range-azimuth (cross-range) resolution cell by exploiting compressive sampling [8, 9, 10, 31].

In this chapter the 3D SAR model is derived based on [5]. A basic introduction to compressive sampling is given as well as deriving a model for reconstructing the elevation dimension of the 3D scene using compressive sampling.

3.1 The 3D SAR Model

Consider the acquisition geometry shown in Fig. 3.1 that consists of P (odd) parallel SAR passes over a target region. This type of SAR acquisition is called multipass SAR. The P passes form the P synthetic apertures u_p $(p = 1, 2, 3, ..., P)$ in the cross-range

[2] "Height" direction refers to the direction orthogonal to the ground plane.

direction which are supposed to be parallel to a reference synthetic aperture. Let $P/2$ be the reference pass which defines the cross-range u and range x directions that is the slant plane (x, u). The orbits may not necessarily be coplanar and uniformly spaced (Fig. 3.2). Let $s_{\|p}$ be the spacing between the pth orbit and the reference orbit measured in a direction parallel to the viewing angle, and let $s_{\perp p}$ be the spacing between the pth orbit and the reference orbit measured in the direction orthogonal to the viewing angle (Fig. 3.2).

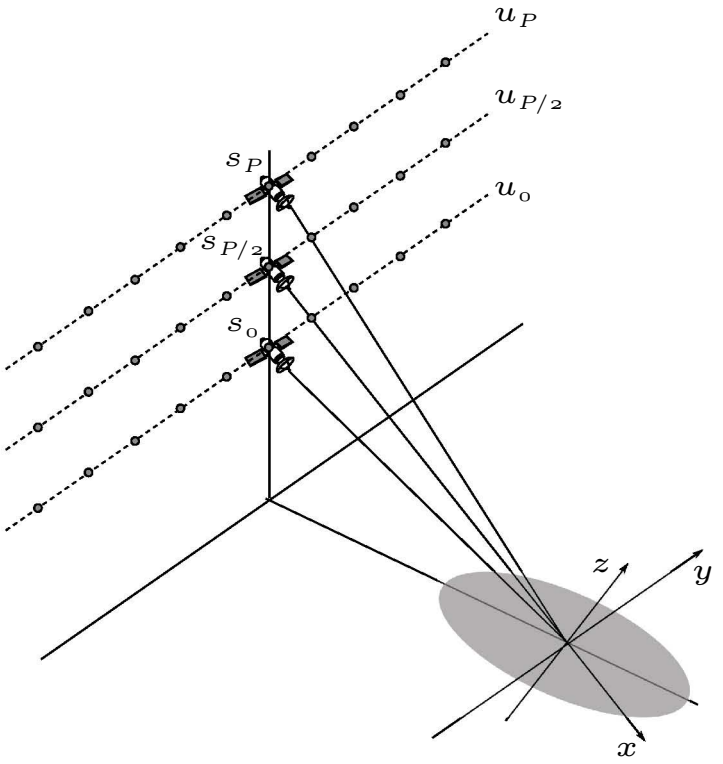

Figure 3.1: Multipass SAR geometry

L_s is the half-size of the in-orbit (elevation) aperture or half-baseline and θ_v is the viewing angle measured as the angle between the vector joining the reference orbit to the centre of the target region and the unit vector orthogonal to the ground plane. The illuminated elevation region falls within the interval

$$z \in [-Z_0, Z_0]$$

Consider three targets A, B and C shown in Fig. 3.2 which all lie in the same range-azimuth resolution cell. In each pass, the radar moves along the synthetic aperture, u_p and transmits coherent phase modulated pulses in the range direction, x at regular intervals along the synthetic aperture. The elevation profile of each target in the scene is intrinsically integrated into the return echoes. The signals acquired along each orbit are processed using classical 2D focusing techniques to obtain the estimate of the 2D scene reflectivity. The stack of range-azimuth focused images are then coregistered with sub-pixel accuracy and phase compensated to account for errors introduced by atmospheric propagation and possible height deformations on the ground [5]. Each pixel in the range-

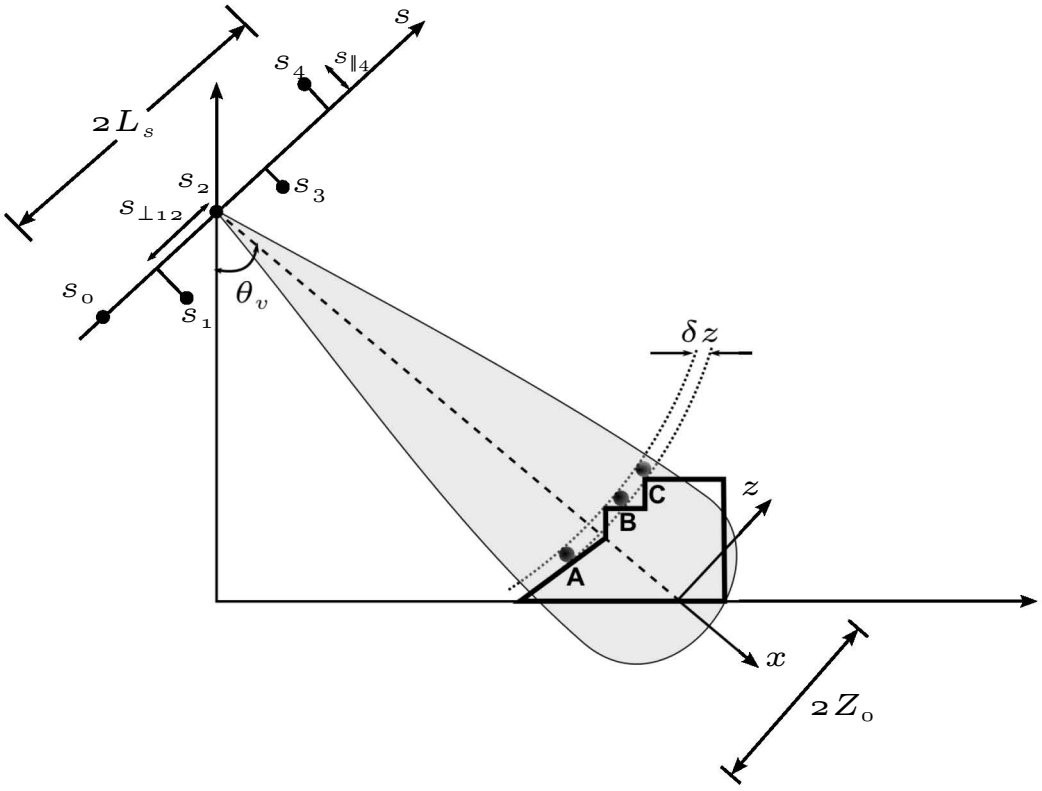

Figure 3.2: Multipass SAR geometry in the range-elevation (x,s) plane

azimuth coordinate of the focused image acquired by the pth orbit with orthogonal baseline $s_{\perp p}$ is given by the integral superposition of the contributions of all the targets lying in the corresponding range-azimuth resolution cell but located at different elevation coordinates, z. These contributions are summed up (3.1) with different phase factors depending on the range $R(s_p, z)$ between the target and the pth sensor.

$$g(x,u,s_p) = \int_{-Z_0}^{Z_0} \gamma(x,u,z) e^{-j\frac{4\pi}{\lambda}R(s_p,z)} dz \qquad -L_s \le s_p \le L_s \tag{3.1}$$

where λ is the wavelength and $\gamma(x,u,z)$ is the 3D scene reflectivity function. Note that a sensor-dependent amplitude weighting function has been neglected in the above equation for simplicity. If the in-orbit baseline span, $2L_s$ is small compared to the range to the target, then the range function $R(s_p, z)$ in (3.1) can be expanded by Taylor series to give

$$R(s_p,z) = x + \frac{\left(z - s_{\perp p}\right)^2}{2x} + s_{\| p}$$

Therefore (3.1) becomes

$$g(x,u,s_p) = e^{-j\frac{4\pi}{\lambda}\left(x+s_{\| p}\right)} \int_{-Z_0}^{Z_0} \gamma(x,u,z) e^{-j\frac{2\pi}{\lambda x}\left(z-s_{\perp p}\right)^2} dz \tag{3.2}$$

For the sake of simplicity, dependence of the signal g and γ on range and azimuth coordinates will be ignored since (3.2) can be written for each pixel of coordinates x and u,

in the stack of range-azimuth focused images. So for each pixel (x, u) we have a $P+1$-dimensional elevation vector $g(s_p)$, whose pth generic element is given by

$$g(s_p) = e^{-j\frac{4\pi}{\lambda}\left(x+s_{\|p}\right)} \int_{-Z_0}^{Z_0} \gamma(z) e^{-j\frac{2\pi}{\lambda x}\left(z-s_{\perp p}\right)^2} dz \tag{3.3}$$

The quadratic phase factor of (3.3) is due to the Fresnel or paraxial approximation [4]. This distortion can be compensated by multiplying the received signal with the conjugate phase factor that corresponds to the echo of a target located at the centre elevation, that is $e^{j\frac{4\pi}{\lambda}R(s_p,0)}$. This process is called deramping and the result is

$$g(s_p) = \int_{-Z_0}^{Z_0} \gamma(z) e^{-j\frac{2\pi}{\lambda x}z^2} e^{j\frac{4\pi s_{\perp p}}{\lambda x}z} dz \tag{3.4}$$

The z^2-dependent phase factor in (3.4) corresponds to the residual video phase [5, 4] and it is associated to the curvature of the incident wavefront which corrupts the phase of the final image which is irrelevant if only the magnitude is of interest. In cases where it is important to preserve the phase, it can be compensated by a post-processing phase compensation. For simplicity, the residual video phase will be absorbed into the 3D reflectivity function $\gamma(z)$, so that the equation to be considered becomes

$$g(s_p) = \int_{-Z_0}^{Z_0} \tilde{\gamma}(z) e^{j2\pi\frac{2s_{\perp p}}{\lambda x}z} dz = \int_{-Z_0}^{Z_0} \tilde{\gamma}(z) e^{-j2\pi\xi_p z} dz = \mathscr{F}\left\{\tilde{\gamma}(z)\right\}|_{\xi_p} \tag{3.5}$$

where $\xi_p = -2s_{\perp p}/\lambda x$ is the spatial elevation frequency and $\tilde{\gamma}(z) = \gamma(z)e^{-j\frac{2\pi}{\lambda x}z^2}$ is the one-dimensional scene reflectivity function in the elevation domain including the residual video phase. Note that (3.5) is the Fourier transform of the 3D reflectivity function therefore an estimate of the 3D reflectivity function $\tilde{\gamma}(z)$ can be obtained by taking the inverse Fourier transform of $g(s_p)$. This can easily be implemented with fast Fourier transform algorithms (FFT). However this operation requires uniform sampling of the involved signals at a rate which satisfies the Nyquist sampling criterion, which if violated will cause aliasing and high-level sidelobes in the reconstructed image. The 3D reflectivity function in (3.5) can also be estimated by spectral estimation techniques under the condition that the range migration caused by the different viewing angles of the acquisition along the elevation aperture is much smaller than the range resolution. Consequently the restriction on the elevation extention of the ground scene to be imaged is given by

$$Z_0 \ll \frac{\triangle_x X_c}{4L_s} \tag{3.6}$$

This condition is easily satisfied in spaceborne SAR since the range X_c is far greater than the baseline span L_s and the range resolution $\triangle_x$ is small. However with SAS, the range is comparable to the baseline span. In such systems a compromise has to be made in order for the above condition to be satisfied. For example, one can decrease the range resolution

in order to alleviate the effect of range migration from different viewing angles.

3.2 Sampling Requirements and Resolution

When the FFT technique is used, the ground elevation coordinate, z in (3.5) has to be sampled uniformly with a sample spacing $\triangle_z$ such that [5]

$$\triangle_z = \frac{\lambda X_c}{2N_z\triangle_s} = \frac{\lambda X_c}{4L_s} \tag{3.7}$$

where $\triangle_s$ is the in-orbit elevation sampling interval and N_z is the number of samples in the discrete version of the 3D reflectivity function i.e. $\tilde{\gamma}(n_z\triangle_z)$ and of the transformed sequence $g(n_z\triangle_s)$. This corresponds to an in-orbit elevation spacing of

$$\triangle_s = \frac{\lambda X_c}{2N_z\triangle_z} = \frac{\lambda X_c}{4Z_0} \tag{3.8}$$

The 3-dB elevation resolution obtainable by the inversion of (3.5) is related to the maximum orthogonal baseline extent $2L_s$ [5] and is given by

$$\triangle_z = \frac{\lambda X_c}{4L_s} \tag{3.9}$$

In most practical cases, the above conditions are seldom satisfied as the orbits are usually not uniformly spaced along the s-domain also the number of acquisitions (number of orbits) M_z is far less than N_z. However by exploiting the sparsity of the signal $\tilde{\gamma}(z)$ (that is there are only a few scatters with different elevations in one range-azimuth resolution cell), it is possible to obtain a very satisfactory reconstruction of the signal even with a few and randomly spaced acquisitions within the synthetic elevation aperture [5].

3.3 Compressive Sampling

Compressive sampling also known as compressive sensing is a model-based framework for data acquisition and signal recovery that is based on the principles of sparsity and incoherence. Sparsity which is associated to the signal of interest means that the signal is sparse or compressible, having a concise representation in a given basis. Incoherence is associated to the sensing modality [9] and it expresses the idea that objects having a sparse representation in the sparsity basis must be spread out in the domain in which they are acquired similar to the way a dirac impulse in the time domain is spread out in the frequency domain and vice versa. If a signal of interest meets the above conditions then by taking only a few linear non-adaptive measurements, its full-length can be recovered by l_1-norm minimization. In the context of the discussion of 3D SAR reconstruction, sparsity requires that only a small number of fixed targets exist in the same range-azimuth

resolution cell. For detailed derivation of the compressive sampling theorems the reader is referred to [9, 31, 32]. The compressive sampling approach to estimating the reflectivity profile in the elevation direction will now be discussed.

Let $\hat{\gamma}(z)$ be a finite resolution estimate of the scene reflectivity function $\tilde{\gamma}(z)$ in the elevation domain (3.5) at a given azimuth and range position. Consider a set of vectors $\{\psi_i(z)\} \in \mathbb{R}^{n_z}$ with $i = 1, 2, 3, ..., N_z$ called the sparsity basis that provides a S-sparse resprresentation of $\hat{\gamma}(z)$, this means that $\hat{\gamma}(z)$ can be written as a linear combination of S basis vectors (with $S < N_z$)

$$\hat{\gamma}(z) = \sum_{i=-N_z/2}^{i=N_z/2} \alpha_i \psi_i(z) = \sum_{k=1}^{S} \alpha_{i_k} \psi_{i_k}(z) \tag{3.10}$$

where the set $\{i_k\}$ are the indices of the vectors and $\{\alpha_{i_k}\}$ are the corresponding complex weighting coefficients.

There are various basis functions which can be used to represent and compress natural signals, images and other data for instance the DCT, Gabor frames and wavelets [8, 9, 31]. Let the sinc basis function be used to represent the estimate of elevation reflectivity function with a 3-dB resolution ρ_z, so that the sparsity basis takes the form

$$\psi_i(z) = \text{sinc}\left(\frac{\pi(z - i\rho_z)}{\rho_z}\right) \tag{3.11}$$

To achieve super-resolution estimate of the reflectivity function we consider $\rho_z = \triangle z/\eta$ where $\eta \geq 1$ is the super-resolution factor indicating the resolution increment with respect to the nominal 3-dB resolution given by (3.9). Uniformly sampling $\hat{\gamma}(z)$ at the points $z_{n_z} = n_z\rho_z = n_z\triangle z/\eta$ with $n_z = -(N_z - 1)/2, ..., (N_z - 1)/2$ to give $\hat{\gamma}$, an $N_z \times 1$ column vector collecting such samples, and by stacking the basis functions $\psi_i(z)$ as columns into an $N_z \times N_z$ sparsity basis matrix, (3.10) can be written in matrix notation as

$$\hat{\gamma} = \Psi\alpha \tag{3.12}$$

where α is the $N_z \times 1$ column vector of complex weights with S nonzero elements. Note that with the given sampling points, the matrix Ψ becomes the identity matrix. From (3.12) one can notice that once the complex weighting vector α is known, an estimate of the elevation reflectivity function can be obtained.

The next question is how to determine the complex weight vector α since there is no direct measure of the N_z coefficients? The answer leads to the introduction of the measurement matrix. Since no direct measure of the N_z coefficients in α_i is available but only a number $M_z < N_z$ linear projections of the 3D reflectivity function measured as samples of the signal $g(s_p)$ (3.5). The relationship between the measure data $g(s_p)$ and the vector $\hat{\gamma}$ can be written by discretizing (3.5) with a uniform sample spacing of $z_{n_z} = n_z\rho_z$ and approximating the integral with a summation and $\tilde{\gamma}(z)$ with its finite resolution estimate,

$\hat{\gamma}(z)$:

$$\frac{1}{\rho_z} g(s_p) \approx \sum_{-N_z/2}^{N_z/2} \hat{\gamma}(z_{n_z}) e^{-j2\pi\xi_p z_{n_z}} \tag{3.13}$$

Except for an inessential multiplicative constant (3.13) can be written in matrix notation as

$$\mathbf{g} = \Phi\hat{\gamma} \tag{3.14}$$

where $\mathbf{g}$ is the $M_z \times 1$ column vector and Φ is an $M_z \times N_z$ measurement matrix of N_z-long M_z measurement row vectors φ_p^T, whose generic element pn_z is given by

$$\{\Phi\}_{pn_z} = \frac{1}{\sqrt{N_z}} e^{-j2\pi\xi_p z_{n_z}} = \frac{1}{\sqrt{N_z}} e^{-j2\pi\xi_p \rho_z n_z} \tag{3.15}$$

Since $M_z < N_z$ in (3.14), the recovery of signal $\hat{\gamma}$ from the measurements $\mathbf{g}$ is ill-posed. However, based on CS theory, given the M_z-vector measurements of $\mathbf{g}$ the recovery algorithm can be formulated by solving an l_1-norm minimization problem [5, 8, 9, 31, 10]

$$\hat{\alpha} = \arg\min \|\alpha\|_1 \quad \text{subject to } \mathbf{g} = \Phi\Psi\alpha. \tag{3.16}$$

This optimization problem is what [31] refers to as basis pursuit and it can be solved with traditional linear programming techniques. Observe that (3.16) expresses an underdetermined system of linear equations with a non-unique solution, however CS theory shows that when an incoherency property between Φ and Ψ, it is possible to recover the S-largest $\hat{\alpha}_i$ with overwhelming probability from a number of measurements that satisfies the following inequality

$$M_z \geq C \cdot \mu^2(\Phi, \Psi) \cdot S \cdot N_z \cdot (\log N_z)^4 \tag{3.17}$$

where C is a small positive constant and S is the number of nonzero coefficients of the signal, and $\mu(\Phi, \Psi)$ is the coherence between the sensing basis Φ and the representation basis Ψ that is defined as

$$\mu(\Phi, \Psi) = \max_{p,i} \frac{\left|\langle \varphi_p, \psi_i \rangle\right|}{\|\varphi_p\|_2 \|\psi_i\|_2} \tag{3.18}$$

Coherence measures the largest correlation between any two elements of Φ and Ψ and it can be shown [5, 9] that the coherence is bounded by the following interval

$$\frac{1}{\sqrt{N_z}} < \mu(\Phi, \Psi) < 1 \tag{3.19}$$

so that when μ is close to its mininum value, $(1/\sqrt{N_z})$ the bases Φ and Ψ are completely different, and when μ approaches the upper bound of 1 then the bases are very similar and more measurements (3.17) would be required for accurate estimation of the S-largest

α. With the given sampling interval, the representation basis Ψ is the identity matrix $\mathbf{I}$ and the sensing basis given by (3.15), μ attains its minimum value of $1/\sqrt{N_z}$ [5].

Compressive sampling is concerned with low coherence pairs [9]. This incoherency property describes that fact that inorder to measure the sparse signal α efficiently, the measurement matrix Φ should spread out the information of highly localized sparse signals in the entire projection space and thereby making them insensitive to undersampling, otherwise the reconstruction of non-zero coefficients will be biased towards certain positions [10].

The optimization problem given in (3.16) is valid in the absence of noise. However in reality, the measured signal $\mathbf{g}$ will contain some noise. The matrix notation in (3.14) can be modified to account for noise

$$\mathbf{g} = \Phi\Psi\alpha + \mathbf{w} \tag{3.20}$$

where $\mathbf{w}$ is a complex Gaussian vector with zero mean and uncorrelated elements [5]. The solution to the optimization problem now come from constraining the l_2-norm of the error in measurements to be less than some threshold ε

$$\hat{\alpha} = \arg\min \|\alpha\|_1 \quad \text{subject to } \|\Phi\Psi\alpha - \mathbf{g}\|_2 \leq \varepsilon \tag{3.21}$$

where ε is a small positive number. The first condition in (3.21) is the same as in the noiseless case, l_1-minimization to enforce the sparseness of α. The second condition forces the solution to be consistent with the data $\mathbf{g}$. [31] calls this equation a constrained basis pursuit denoising problem. The choice of the regularization parameter ε specifies a unique solution path $\hat{\alpha}(\varepsilon)$ and should be chosen based on the noise statistics [5].

Equations (3.16) and (3.21) cannot be solved analytically and for real or complex numbers. An appropriate transformation of the data has to be performed before numerical solutions can be found [33]. This is an area of mathematical programming which deals with the optimization of constrained functions [33]. The transformation of both real and complex valued data is described in detail in [33]. The data in the minimization problem of (3.16) are complex valued so a description for complex valued transformation as derived by [33] follows. However there a various solvers that have be developed to solve basis pursuit problems (3.16) and basis pursuit denoising problems (3.21) even with complex variables such as SPGL1 [34, 35].

l_1-norm minimization of complex valued problems

Equation (3.16) is a part of a family of constrained functions that take on the general form [33]:

$$\min_{\mathbf{S}} \sum_i |S_i|, \; i = 1, ..., N \qquad \text{subject to} \qquad \mathbf{HS} = \mathbf{X} \tag{3.22}$$

where $|S_i|$ denotes the amplitude of S_i and $\mathbf{X} \in \mathbb{K}^M$, $\mathbf{H} \in \mathbb{K}^{M \times N}$, $\mathbf{S} \in \mathbb{K}^N$, $\mathbb{K} = \mathbb{C}$.

l_1-norm minimization problems of (3.22) with complex numbers can be transformed to a second order cone programming (SOCP) problem [33]. For complex numbers, (3.22) is equivalent to

$$\min t \in \mathbb{R} \qquad \text{subject to} \qquad \mathbf{X} = \mathbf{HS}, \text{ and} \qquad |\mathbf{S}|_1 \leq t \tag{3.23}$$

which can be rewritten as the SOCP problem

$$\min_{\hat{\mathbf{S}}} \hat{\mathbf{c}}^T \hat{\mathbf{S}} \quad \text{subject to} \quad \hat{\mathbf{X}} = \hat{\mathbf{H}}\hat{\mathbf{S}}, \left| \begin{bmatrix} \Re(S_i) \\ \Im(S_i) \end{bmatrix} \right|_2 \leq t_i \quad \forall i \tag{3.24}$$

by defining

$$\hat{\mathbf{S}} = \begin{bmatrix} t_1 \\ \Re(S_1) \\ \Im(S_1) \\ . \\ . \\ . \\ t_N \\ \Re(S_N) \\ \Im(S_N) \end{bmatrix} \in \mathbb{R}^{3N}, \quad \hat{\mathbf{c}} = \begin{bmatrix} 1 \\ 0 \\ 0 \\ . \\ . \\ . \\ 1 \\ 0 \\ 0 \end{bmatrix} \in \mathbb{R}^{3N}$$

$$\hat{\mathbf{X}} = \begin{bmatrix} \Re(\mathbf{X}) \\ \Im(\mathbf{X}) \end{bmatrix} \in \mathbb{R}^{2M}$$

$$\hat{\mathbf{H}} = \begin{bmatrix} \mathbf{0} & \mathbf{0} \\ \Re(\mathbf{h_1}) & \Im(\mathbf{h_1}) \\ -\Im(\mathbf{h_1}) & \Re(\mathbf{h_1}) \\ . & . \\ . & . \\ . & . \\ \mathbf{0} & \mathbf{0} \\ \Re(\mathbf{h_N}) & \Im(\mathbf{h_N}) \\ -\Im(\mathbf{h_N}) & \Re(\mathbf{h_N}) \end{bmatrix}^T \in \mathbb{R}^{3M \times 3N}$$

where $\mathbf{h_i}$ is a vector formed from the ith row or column of $\mathbf{H}$.

Equation (3.24) can be solved numerically with programs like SeDuMi [36].

Chapter 4

Three-dimensional SAS Processor Design

This chapter describes the design of the 3D SAS processor. It also describes the parameters used in the simulation of the SAS system.

4.1 System Overview

The design of the multiple transducer single-pass SAS imaging system must take the following requirements into account:

1. The required operating frequency range, bandwidth, and sampling rate in both fast-time and slow-time directions.
2. The SAS system must have an output channel which would be used to transmit an analog signal at a sufficiently high sampling rate.
3. Multiple input channels that can receive and sample echoes at a sufficiently high rate.
4. The ability to simultaneously transmit and receive over the output and input channels respectively with rigid control over the timing of transmission and reception of signals.
5. A digitally controlled mechanism to move the transducers along a straight track.

The 3D SAS processor must be able to meet the above requirement in a coordinated manner. With the above requirements, the design of the 3D SAS processor can be divided into four sections. The block diagram of the SAS imaging system showing these different sections is shown in Fig. 4.1.

The PC is used to control the platform position and the data acquisition. Control signals are sent to the control chain via the digital output channels of the data acquisition card

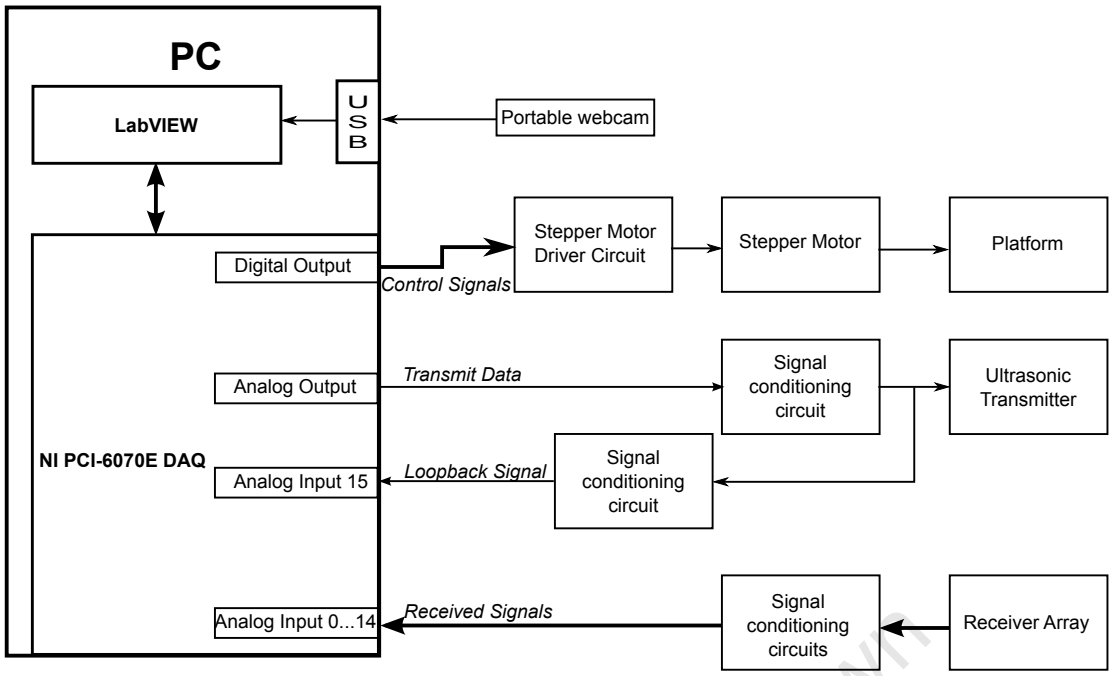

Figure 4.1: Block diagram of the 3D SAS imaging system.

to position the platform at a point on the synthetic aperture. At each point along the synthetic aperture, a chirp signal is generated in LabVIEW and output via the analog output channel of the data acquisition card. The signal passes through an analog signal conditioning circuit built on a piece of veroboard and fed into the output transducer. The transmit signal fed into the output transducer is "looped back" and recorded on an input channel of the data acquisition card. This is the transmit chain of Fig. 4.1. On the receive chain, the echoed chirp from targets in the target region is sensed by the receiving transducers and passed on to separate signal conditioning circuits. The resultant signal from each line is then sampled by the data acquisition card and stored as one row of data in the SAS data matrix for the given transducer. This acquisition process is performed at each position along the synthetic aperture. Once all the data has been acquired over all positions on the synthetic aperture, the stored SAS data is processed in two stages: 2D focusing of the SAS data from each transducer using classical 2D focusing technique, and 3D focusing using the compressive sampling technique.

4.1.1 The Transmit Chain

The transmit chain consists of the analog output channel of the data acquisition card, a signal conditioning circuit and the ultrasonic transmitter. It was designed to operate at a frequency of 42kHz with a total bandwidth of 4kHz. The signal to be transmitted is output from the data acquisition card's analog output channel and is passed through an amplification and bandpass filtering circuit before being transmitted by the ultrasonic transducer. Fig. 4.2 shows the circuit diagram of the signal conditioning circuit used in the transmit chain.

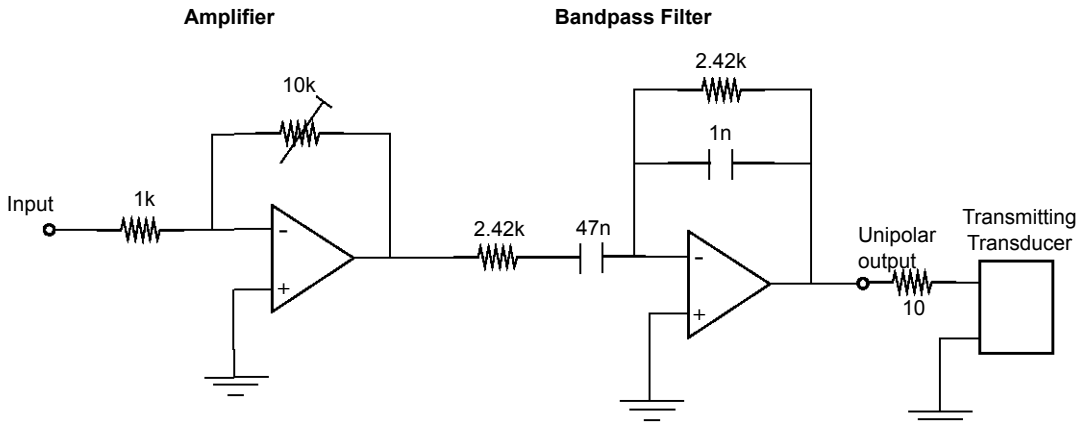

Figure 4.2: Circuit diagram of the unipolar output chain of the 3D SAS imaging system.

The amplification circuit is an LM837 op-amp connected in negative feedback mode to give a maximum adjustable voltage gain of 10. The LM837 op-amp was chosen because it is a low noise op-amp with a high slew rate and a large gain bandwidth product of 25MHz. An active bandpass filter was built using the LM837 with a high pass cut-off frequency of about 1.4 kHz (the series resistor (2.42 kΩ) and capacitor (47nF)) and a low pass cut-off frequency of about 65.8 kHz (the feedback capacitor (1nF) and resistor (2.42 kΩ)). The gain (G), cut-off frequencies (f_{co}), resistance and capacitance values are governed by (4.1) and (4.2). Decoupling capacitors (47μF and 1nF) were connected between the supply rails and ground. The transmit board was powered off +/- 12V DC.

$$f_{co} = \frac{1}{2\pi RC} \tag{4.1}$$

$$G = \frac{R_f}{R_i} \tag{4.2}$$

where R_f is the feedback resistance and R_i is the input resistance.

In order to drive the ultrasonic transmitter with more power a bipolar amplification stage was designed using two LM837 op-amps with one connected in the non-inverting configuration while the other in the inverting configuration (Fig. 4.3). This circuit however was prone to oscillations and was therefore not used.

A loopback signal conditioning circuit was also designed to record the transmitted signal for use as a compression filter during range compression (Fig. 4.4). The circuit had to attenuate the high powered transmit signal generated from the unipolar output in order to remain within the limits of the NI PCI-6070E input voltage range.

Fig. 4.5 shows the signal conditioning circuit for the transmit chain that was built on a veroboard.

4.1.2 The Receive Chain

The receive chain consists of the ultrasonic receiver array, an array of signal conditioning circuits and the analog input channels of the data acquisition card. The array was made up

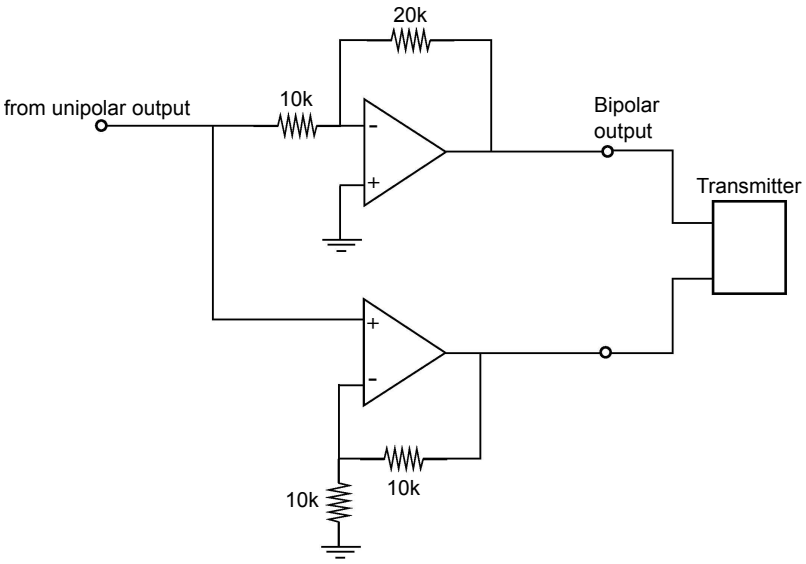

Figure 4.3: Circuit diagram of the bipolar output chain.

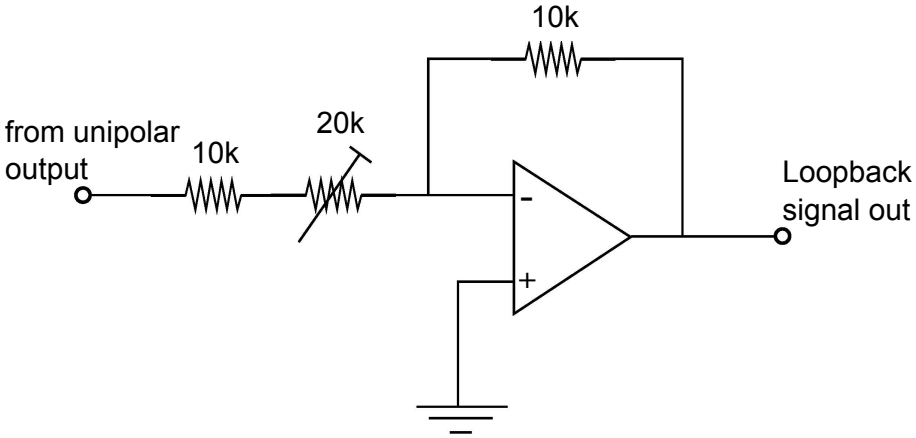

Figure 4.4: The loopback circuitry.

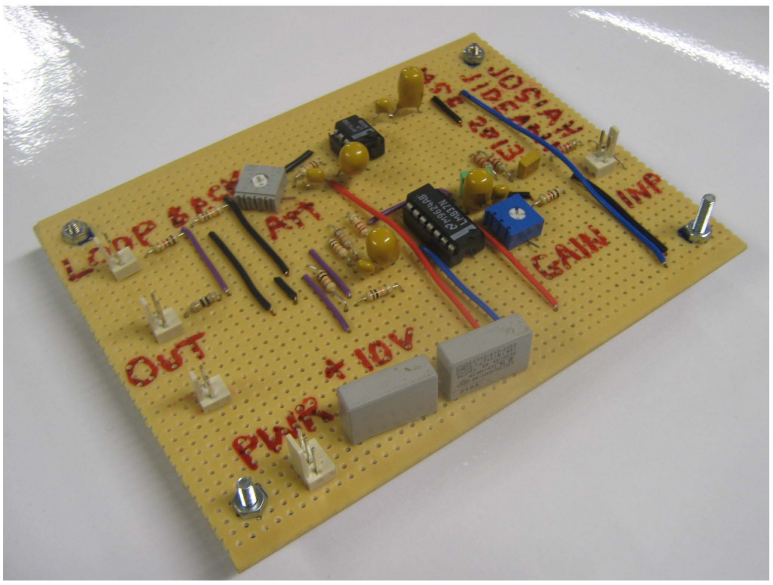

Figure 4.5: The transmit circuit module

of 15 receive transducers (Fig. 4.6). Fig. 4.7 is a photograph of the actual transducer array. The signal conditioning circuit consists of a bandpass filter and an amplifier to increase the level of the signal to enable accurate detection by the analog to digital converter in the data acquisition card. The LM837 was the heart of the signal conditioning circuit. It was connected in inverting configuration with bandpass filtering with a gain of 22 (Fig. 4.8). Using (4.1) and (4.2) the appropriate resistor and capacitor values were chosen for a low- and high-pass cutoff frequencies of about 72 kHz and 10 kHz respectively. This circuit was built for all 15 channels on veroboard (Fig. 4.9).

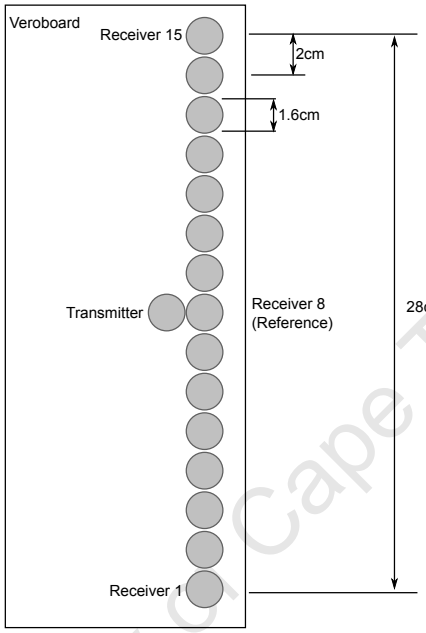

Figure 4.6: The transducer array setup.

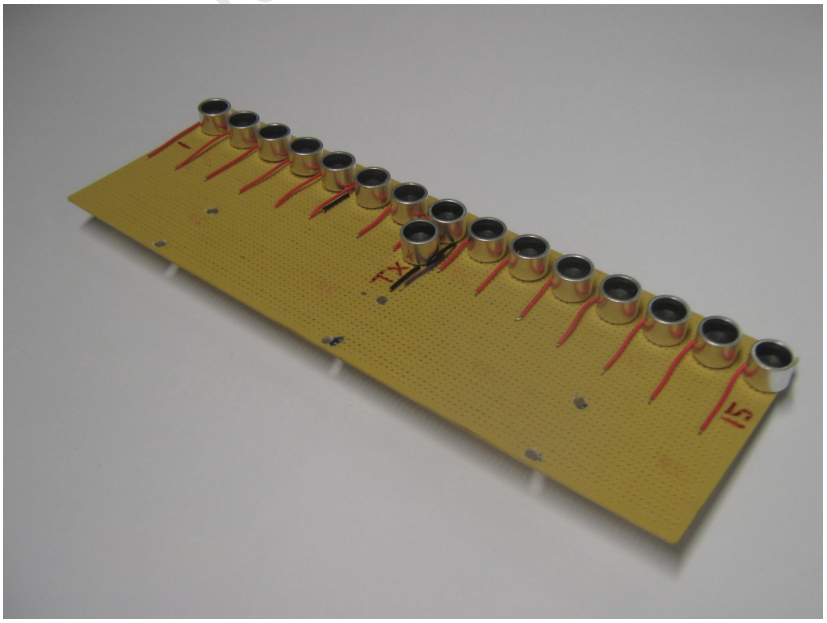

Figure 4.7: Picture of the transducer array.

The ultrasonic transducers (Fig. 4.10) used in both transmit and receive chains were 16mm ultrasonic transducers with a frequency response centred approximately around

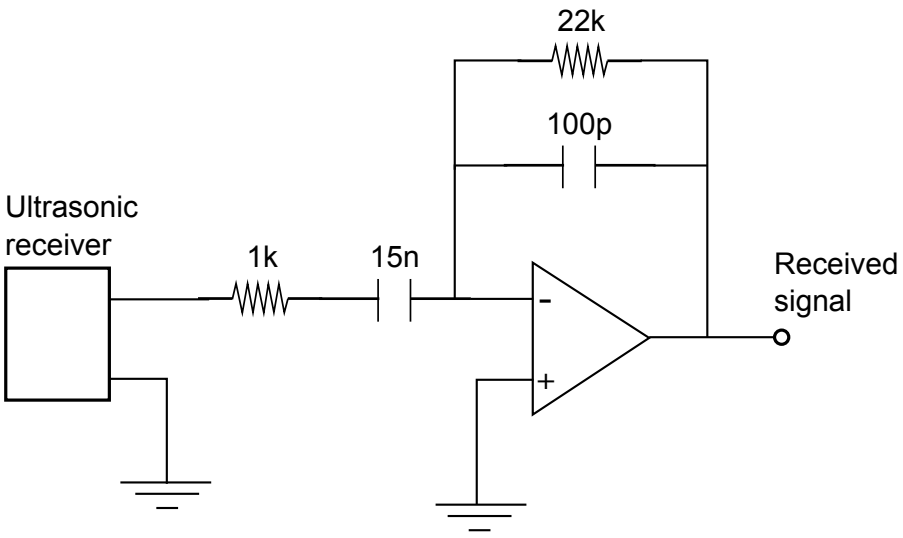

Figure 4.8: The amplifier circuit in an input chain.

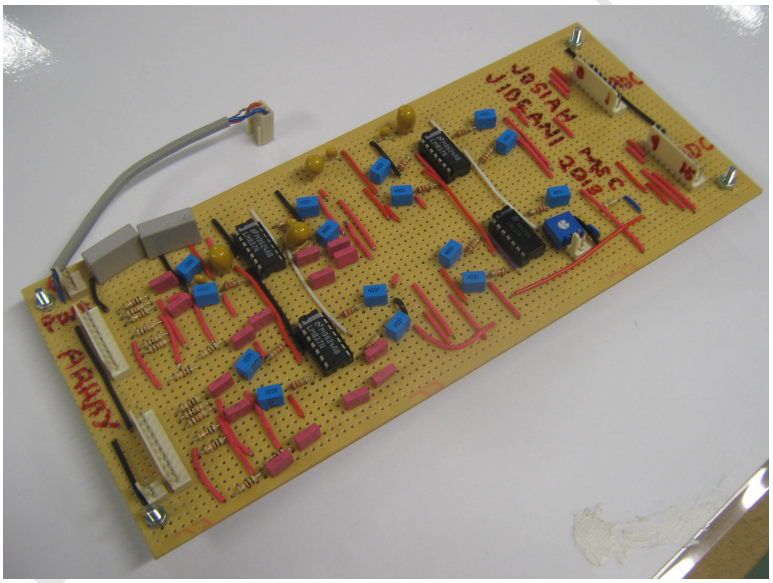

Figure 4.9: The receiver circuit module

Figure 4.10: The ultrasound sensor.

40kHz. For 3D SAS imaging, 15 transducers were used as receivers in the receive chain while one was used as a transmitter in the transmit chain.

4.1.3 The Control Chain

The control chain consists of a platform, a stepper motor, a stepper motor driver, and two digital output channels of the data acquisition card. The platform (Fig. 4.11a) which carries the ultrasonic transducers was mounted on a 2.0m long metal rail structure (Fig. 4.11b) designed for the university.

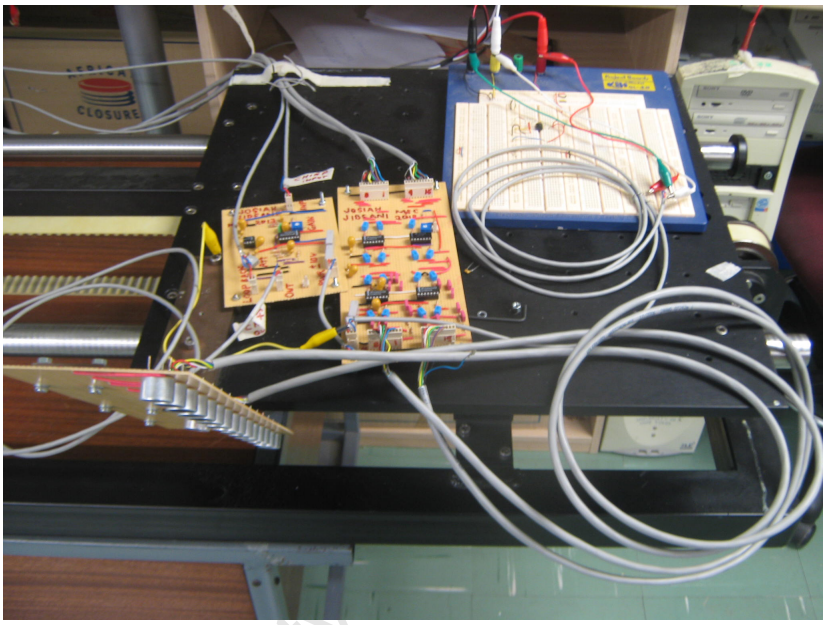

(a)

(b)

Figure 4.11: Photograph of the SAS platform and support structure.

With the aid of the stepper motor, the platform could be moved in a straight line to generate a synthetic aperture length of about 1.4m. The stepper motor was the SLO-SYN M093-FC11 stepper motor with a nominal DC voltage of 2.65V and 5.5A per winding

and it was driven by the G201 Step-Motor Drive. A pulse width modulation (PWM) signal was output from one of the digital output channels of the data acquisition card and fed into the stepper motor driver circuit. The direction of movement of the platform could be controlled from a graphic user interface designed in LabVIEW and the direction signal was output from the second digital output channel. The minimum step length of the motor was measured to be about 1.235mm. The speed of movement along the track was also measured to be about 8.72mm/s.

4.1.4 The Data Acquisition Card

The NI PCI-6070E data acquistion card was used to digitize the ultrasonic signals from the transducers on transmission and reception. It is a PCI multifunction DAQ with the ability for synchronous transmission and reception on multiple channels. Some of the properties [37] of the card which makes it suitable for the required task are

1. 16 analog inputs with 12-bit input resolution and a maximum sampling rate of 1.25 MS/s.
2. 8 digital input/output lines.
3. 2 analog output channels.

The digital output channels of the NI PCI-6070E card was also used to control the motion of the platform as well as perform synchronized transmission and reception of ultrasonic signals.

4.1.5 LabVIEW

LabVIEW is a system design software designed by National Instruments to provide tools necessary to create and deploy measurement and control systems through hardware integration. It uses a graphical programming language called G, to create programs using block diagrams instead of the common textual-based programs so that most programming actions are described using graphical symbols. LabVIEW contains an extensive library of functions and subroutines for common programming tasks, data acquisition, instrument control, data analysis, data presentation, data storage and other conventional program development tools [38]. LabVIEW programs are called virtual instruments (VIs) because they look and operate like actual instruments [38]. A virtual instrument consists of the interactive user interface and the source code. The interactive user interface or the front panel simulates the front panel of a real instrument as it contains things likes push buttons, toggle switchs, controls and indicators. The source code called the block diagram is the actual G code that runs in the background of the VI. The block diagram supplies a pictorial solution to a programming problem [38]. LabVIEW supports the concept of modular programming in the fact that a VI can contain another VI called a subVI thus

making it possible to write top-level programs or subprograms within other programs or subprograms. The reader is referred to [38] for a detailed tutorial of LabVIEW. In this work a VI (Fig. 4.12) was designed for the SAS data acquisition process via integration with the NI PCI-6070E data acquisition card. Other VIs were designed for the calibration of the transducer array frequency response and the transducer beamwidth measurement.

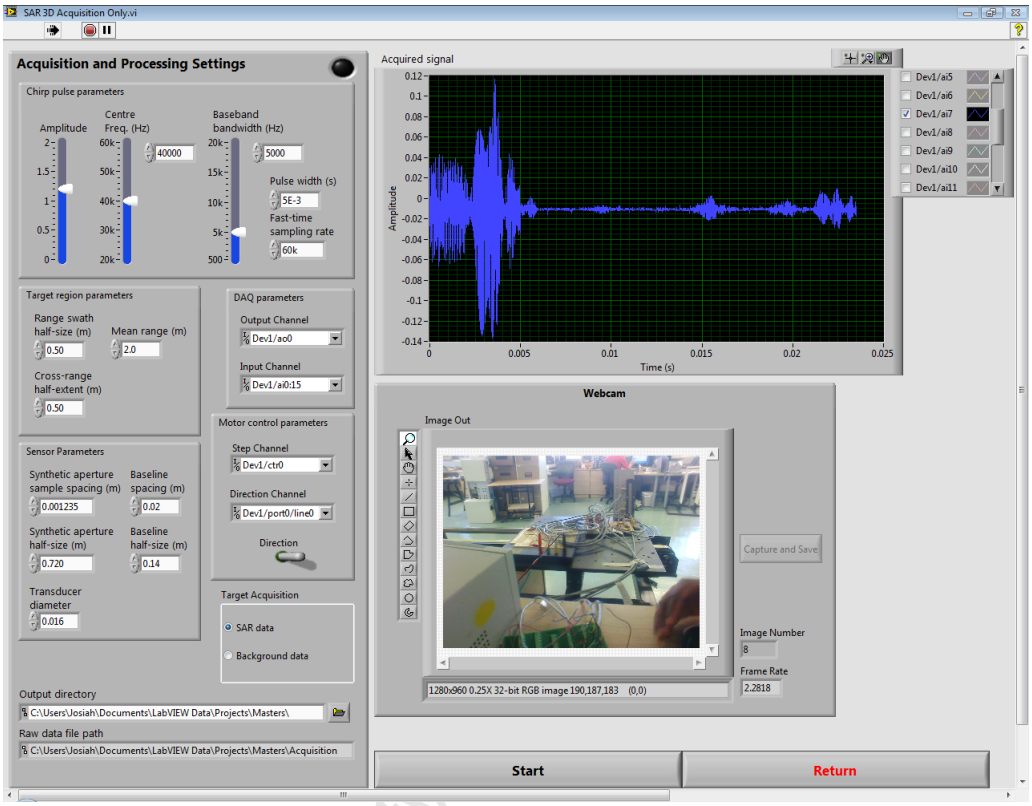

Figure 4.12: Multi-channel SAS data acquisition VI designed in LabVIEW

4.2 Fast-time Pulse Compression via Inverse Filtering

In this section the implementation of fast-time pulse compression (range compression) via inverse filtering is described. A theoretical background to inverse filtering also known as the deconvolution filter was discussed in Section 2.6.2. Fig. 4.13 shows the SAS transmit-receive process a linear system at any given point along the synthetic aperture.

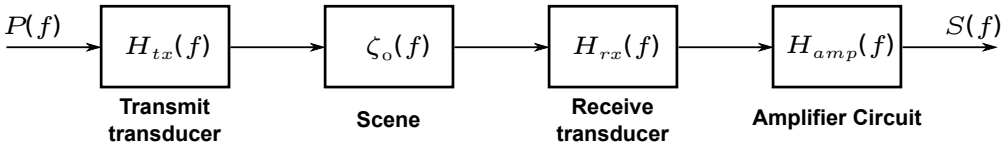

Figure 4.13: System model of the SAS transmit-receive chain.

Let $p(t)$ represent the transmitted signal which is fed into the ultrasound transmitter after amplification and recorded via the loopback line of Fig. 4.1, then $P(f)$ is the Fourier domain equivalent of $p(t)$. $H_{tx}(f)$ and $H_{rx}(f)$ represent the frequency response of the

transmitter and receiver transducers respectively while $H_{amp}(f)$ represents the frequency response of the amplifier circuit. If $\zeta_0(f)$ represents the ideal one-dimensional scene impulse response in the fast-time frequency domain, then the recorded signal $S(f)$ can be written in terms of the transmitted signal and the impulse response as:

$$S(f) = P(f) \cdot H_{tx}(f) \cdot H_{rx}(f) \cdot H_{amp}(f) \cdot \zeta_0(f) \qquad \text{for } f_c - B_0 \leq f \leq f_c + B_0$$

If the amplifier has a flat amplitude response over the frequency of operation, then the recorded signal can be written as

$$S(f) = P(f) \cdot H_s(f) \cdot \zeta_0(f) \quad \text{for } f_c - B_0 \leq f \leq f_c + B_0$$

where $H_s(f) = H_{tx}(f) \cdot H_{rx}(f)$ is the impulse response of the transmitter-receiver pair in the frequency domain. To recover a bandlimited version of the impulse response of the scene, an inverse filter is applied to the recorded signal $S(f)$:

$$\zeta(f) = S(f) \cdot H_c(f) \cdot H_d(f)$$

where $\zeta(f)$ is the bandlimited version of the scene impulse response in the fast-time frequency domain,

$$H_c(f) = \begin{cases} \frac{1}{P(f)} & f_c - B_0 \leq f \leq f_c + B_0 \\ 0 & otherwise \end{cases}$$

and

$$H_d(f) = \begin{cases} \frac{1}{H_s(f)} & f_c - B_0 \leq f \leq f_c + B_0 \\ 0 & otherwise \end{cases}$$

Fig. 4.14 shows a system model of the inverse filtering process. The recorded signal S(f) can be converted down to baseband by quadrature demodulation prior to inverse filtering.

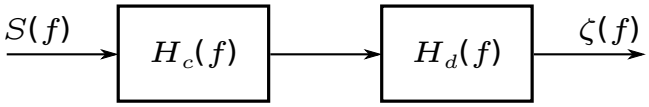

Figure 4.14: System model of range compression via inverse filtering.

The following steps were taken to implement fast-time compression via inverse filtering at each azimuth position:

- The received echos were sampled at a rate which satisfied the Nyquist sampling criterion to avoid aliasing in the received signal spectrum.
- The received data was Fourier transformed in and converted to complex baseband format.

- The inverse filter was applied in the frequency domain to compensate for all linear system effects that convolved into the received signal. The process of obtaining the inverse filter is described the next section.
- The Hann window (2.47) was applied to reshape the spectrum inorder to reduce sidelobes which would appear in the time domain.
- The resulting data was inverse Fourier transformed to obtain the compressed base-banded version of the signal in the time domain.

4.3 System Measurements

4.3.1 Channel Frequency Responses

To obtain the impulse responses of all the transceiver channels in the system, $H_{si}(f)$, a transmitter was placed directly opposite the receiver array and at a distance of about 2.0m. One-hundred long-duration chirp pulses with a bandwidth of about 10kHz centred on the 40kHz were intermittently transmitted to the receiver array to simulate an ideal point target response. The average of the transmitted and received signals were stored and processed to obtain the transducer frequency responses with minimal noise. The system model for this configuration is similar to Fig. 4.13. The recorded signal is a delayed version of the transmitted signal which is distorted in amplitude and phase by the impulse response of the transducer pair (the transmitter and the *i*th receiver). So the received signal at the *i*th receiver can be written in the frequency domain as

$$S_i(f) = P(f) \cdot H_{si}(f) \cdot e^{-j\frac{2\pi f \cdot d_i}{c}}$$

where d_i is the distance between the transmitter and the *i*th receiver. Note that since we assume a point target response, $\zeta(f) = 1$ that is why $\zeta(f)$ is omitted from the equation above. The frequency response of the channels can therefore be obtained by

$$H_{si}(f) = \begin{cases} \frac{S_i(f)}{P(f) \cdot e^{-j\frac{2\pi f d_i}{c}}} & -B_0 \leq f - f_c \leq B_0 \\ 0 & otherwise \end{cases}$$

where $B_0 = \frac{B_t}{2}$ is the baseband bandwidth of the transmitted signal.

The frequency responses of all channels were stacked into a 2D array and used to design the inverse filter which compensates for the system frequency response in the range compression stage. Fig. 4.15 shows a plot of the magnitudes and phases of the frequency response from all channels. Fig. 4.16 shows the frequency response of the reference channel. It can be observed that the channels have similar frequency responses and narrow bandwidth (≈4kHz). Note that the frequency responses of the channels contain the

combined responses of both transmitter and the respective receiver at the given channel.

4.3.2 Transducer Beam Pattern

The beam pattern of the transducers was determined by fastening the transmitter onto the shaft of a stepper motor (Fig. 4.17) and rotating it through 360^o in front of the receiver which was placed at about 1.5m away. The stepper motor rotated in 1.8^o steps. At each step, a chirp pulse with centre frequency of 40kHz and bandwidth of 10kHz was transmitted, recorded from the receiver and stored as one row of a matrix data. Each row of data was then matched filtered to obtain the peak values of the magnitude signal. These values were then plotted on a polar plot against each azimuth position. Fig. 4.18 shows the polar plot of the transducer beam pattern from which one can deduce a divergence angle of about 55 degrees measured from the point where the power drops to about half the maximum value.

4.4 System Parameters

4.4.1 Target region

The SAS imaging was carried out indoors in a laboratory, so the size of the target region was chosen based on the characteristics of the system components and the amount of space available. An area of $1\,\mathrm{m}^2$ in the slant-range and azimuth plane was chosen as the target region. The mean slant range of the target region was chosen as $2\,\mathrm{m}$.

4.4.2 Operating frequency and bandwidth

The transducer frequency response measurements in Section 4.3.1 was used to determine the effective operating frequency and bandwidth that could be used for 3D SAS imaging. There was not much freedom in selecting a centre frequency as the transducers have a narrow bandwidth around 40kHz so this was chosen as the centre frequency and a bandwidth of 4kHz was chosen. This corresponds to a range resolution of $\delta x_{3dB} = \frac{0.89c}{2B_t} \approx 3.78$cm.

4.4.3 Fast-time sampling rate

The fast-time sampling rate was chosen so that it satisfies the Nyquist sampling criterion for bandpass signals and which would satisfy the data acquisition cards mulitplexing settling time. Based on the Nyquist criterion the minimum sampling rate for a signal with a bandwidth, B_t is $f_s > 2B_t$. With the chosen bandwidth this condition amounts to $f_s > 8\,\mathrm{kHz}$. The maximum sampling rate possible when sampling on one analog input channel of the NI PCI-6070E is 1.25MS/s. Sampling on multiple channels simultaneously reduces this rate so that the maximum possible rate is given by $f_s < \frac{1.25\times10^6}{N}$, where N is

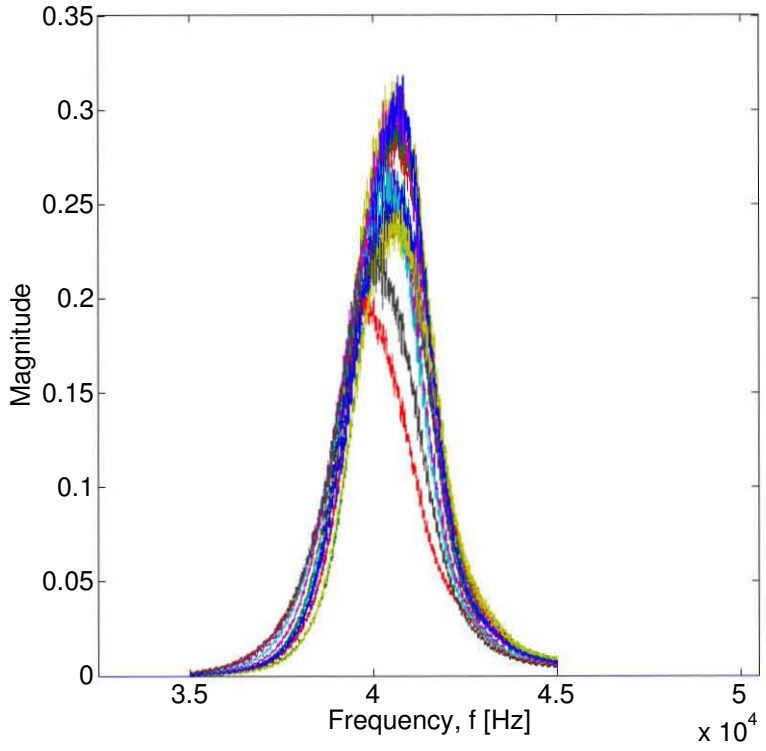

(a)

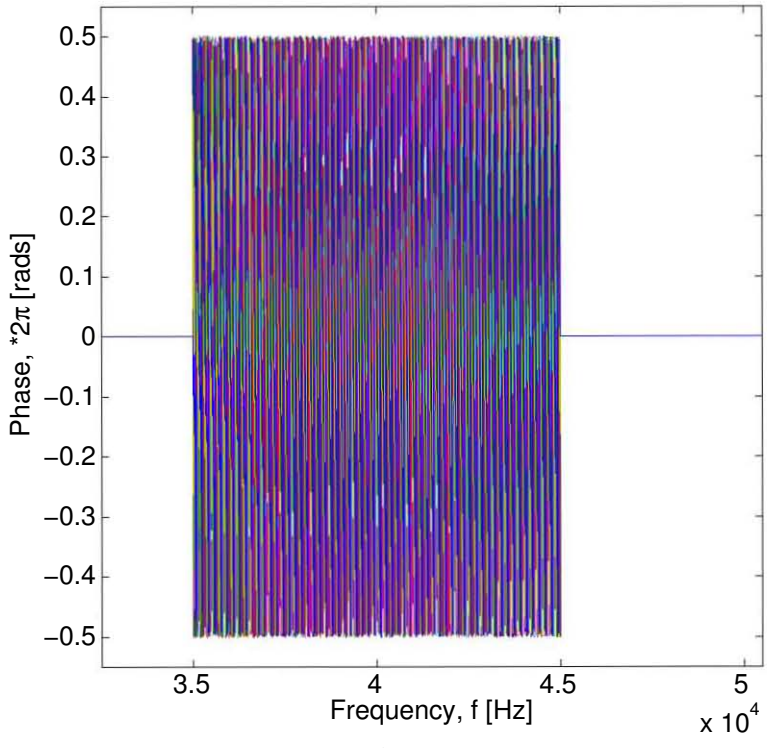

(b)

Figure 4.15: Frequency response of the 15 channels superimposed (a). Magnitude. (b). Phase

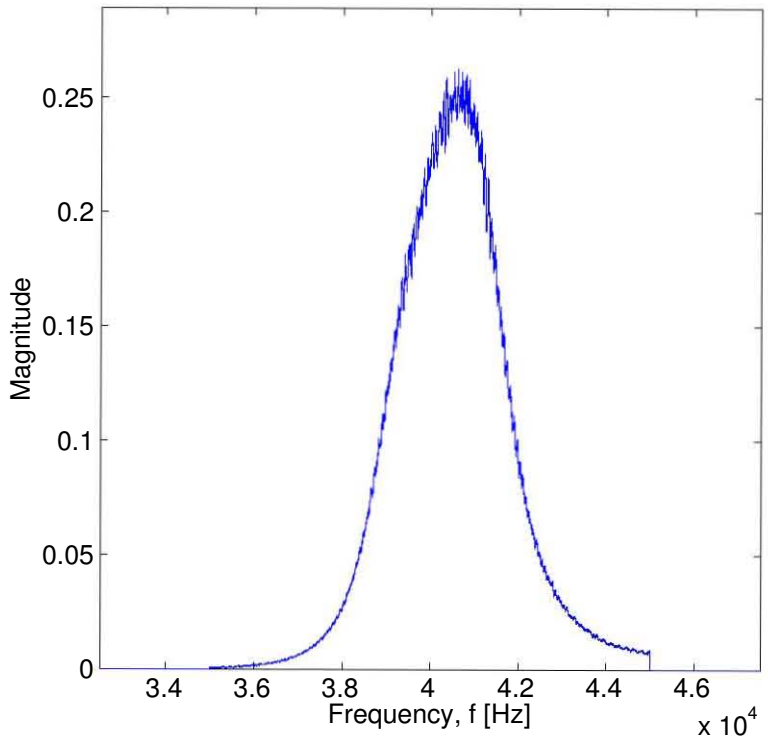

(a)

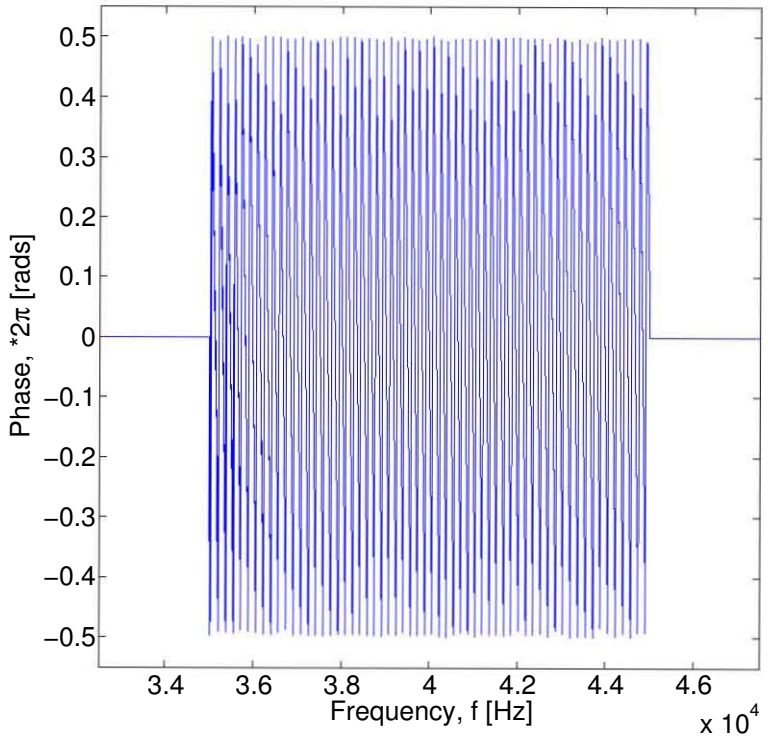

(b)

Figure 4.16: Frequency response of the reference channel (a). Magnitude. (b). Phase

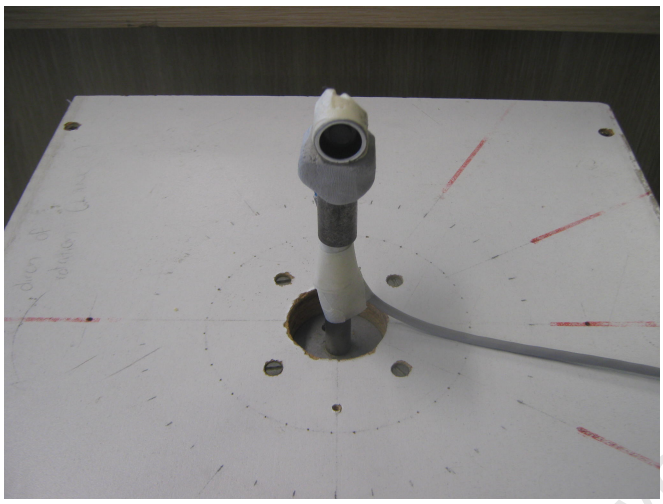

Figure 4.17: The transducer mounted on the shaft of a motor to determine its beam pattern.

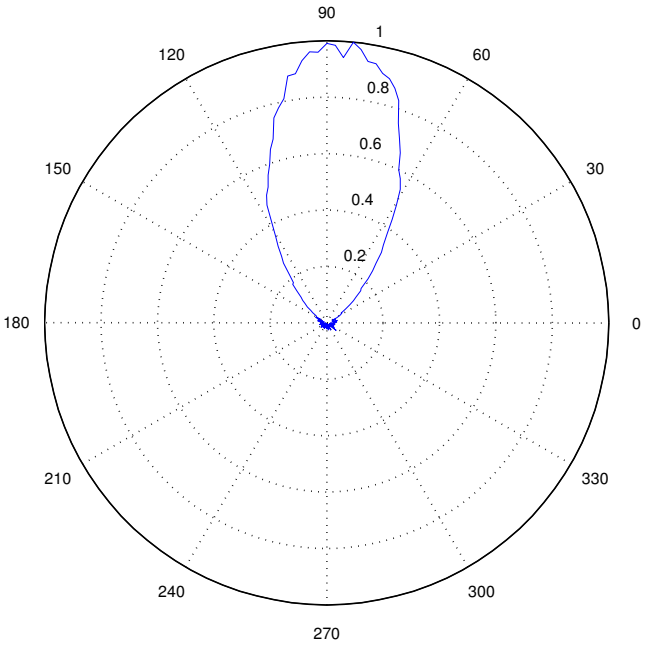

Figure 4.18: Polar plot of the transducer beam pattern measured at 40kHz

the number of channels. For the case of $N = 16$ (15 receive channels + 1 transmit loop-back channel), $f_s < 78.1\,\text{kHz}$. However by also taking the settling time of the multiplexer into consideration, a sampling frequency of $f_s = 60\,\text{kHz}$ was chosen.

4.4.4 Synthetic aperture sampling interval

The step frequency of the stepper motor was matched to the pulse repetition frequency thus implementing stop-and-go sampling in the synthetic aperture direction so that each synthetic aperture sample corresponds to a new position in the scene. The distance between each step of the stepper motor was measured by taking the average of the distance travelled by the platform over 1000 steps and was found to be to be about $\triangle_u = 0.1235\text{cm}$.

4.4.5 Pulse width

The chirp pulse was used in the system and the length of the chirp pulse or pulse width T_p is constrained by the target region. The pulse width must not be longer than the round-trip delay between the radar and the closest point of the target region [19] $T_p \leq \frac{2r_{min}}{c}$, where c is represents the speed of light and r_{min} is the distance to the closest point of the target region. The minimum range of the target region in this system was $r_{min} = 1.5\text{m}$ to give a maximum pulse width of $T_p < 9\,\text{ms}$. Also since the energy in the transmitted pulse is proportional to the length of the pulse, it would not be desirable to make T_p too small. So to satisfy the above conditions and to maintain a time-bandwidth product of $B_t T_p \geq 20$ a pulse width of 5ms was chosen.

4.4.6 Transducer array baseline and spacing

A total of 15 receivers were arranged in a vertical linear array with a spacing of $\triangle_s = 0.02\text{m}$ measured from the centre of each receiver. The baseline span of the array was therefore $2L_s = 0.28\text{m}$. A single transmitter was placed along-side the middle receiver that was used as the reference for 3D SAS imaging. The rest of the receivers were arranged uniformly and equally on both sides of the reference receiver (Fig. 4.6).

Table 4.1 shows the system parameters used in the 3D SAS imaging system.

Table 4.1: Parameters of the 3D SAS system.

Parameters	**Symbol**	**Value**	**Unit**
Centre frequency	f_c	40	kHz
Bandpass bandwidth	B_t	4	kHz
Baseband bandwidth	$B_0 = \frac{B_t}{2}$	2	kHz
Fast-time sampling rate	f_s	60	kS/s
Pulse propagation velocity	c	340	ms^{-1}
Pulse width	T_p	5×10^{-3}	s
Target region half-size in the range domain	X_0	0.5	m
Target region mean range	X_c	2	m
Target region cross-range half-size	Y_0	0.5	m
Squint angle	θ_s	0	deg
Synthetic aperture sampling interval	$\triangle_u$	1.235×10^{-3}	m
Synthetic aperture half-size	L	0.72	m
In-orbit sampling interval	$\triangle_s$	0.02	m
In-orbit elevation aperture half-size	L_s	0.14	m
Number of receiving transducers/baselines	M_z	15	-
View angle	θ_v	32	deg
Transducer diameter (excluding external casing)	D_y, D_z	0.014	m

Chapter 5

Three-dimensional SAS Simulation Setup

The parameters of the SAS system used in the simulation are given in Table 5.1 and are the same parameters of the real SAS system.

Table 5.1: Parameters of the 3D SAS system used in simulation.

Parameters	Symbol	Value	Unit
Centre frequency	f_c	40	kHz
Bandpass bandwidth	B_t	4	kHz
Baseband bandwidth	$B_0 = \frac{B_t}{2}$	2	kHz
Fast-time sampling frequency	f_s	400	kS/s
Pulse propagation velocity	c	340	ms^{-1}
Pulse width	T_p	5×10^{-3}	s
Target region half-size in the range domain	X_0	0.5	m
Target region mean range	X_c	2	m
Target region cross-range half-size	Y_0	0.5	m
Squint angle	θ_s	0	deg
Synthetic aperture sampling interval	$\triangle_u$	1.235×10^{-3}	m
Synthetic aperture half-size	L	0.72	m
In-orbit sampling interval	$\triangle_s$	0.02	m
In-orbit elevation aperture half-size	L_s	0.14	m
Number of receiving transducers/baselines	M_z	15	-
Transducer diameter (excluding external casing)	D_y, D_z	0.014	m

5.1 The Target Region

The simulated target region was a $1m^2$ swath which spanned 1m in both slant-range and cross-range directions, and contained a set of point targets with the same reflectivity amplitude and phase. The target region was in broadside view of the transducers so there was zero squint angle. The echo signal from each target was received by an array of 15

transducers moving along a 1.44m long synthetic aperture so that a stack of 2D raw SAS data was acquired and stacked to form a 3D matrix of SAS data.

5.2 The Chirp Pulse

The analytic form of the chirp pulse was used in the simulation and is given by

$$p(t) = e^{j2\pi(\beta t+\alpha t^2)} \qquad \text{for } 0 \leq t \leq T_p \tag{5.1}$$

The instantaneous frequency of the chirp pulse can be obtained from the derivative of the phase.

$$f_{chirp}(t) = \frac{d}{dt}\left[\beta t + \alpha t^2\right] = (\beta + 2\alpha t) \qquad [\text{Hz}]$$

Observe that the instantaneous frequency is a function of time. The values of α and β of the chirp sets the range of frequencies over which the chirp pulse is swept as well as the chirp rate. In this work the chirp was set to sweep between 38kHz to 42kHz.

5.3 Data Acquisition and Signal Processing

Return echoes acquired by each transducer as the platform moved along the synthetic aperture were sampled and stored in a 3D array. The following sampling parameters were selected with respect to the reference transducer (the middle transducer in the array) and were used for all other transducers in the array.

5.3.1 Fast-time Domain Sampling and Processing

Fast-time Sampling Interval

The fast-time samples were collected over the fast-time interval that covers the returns from all the simulated point targets within the swath. Suppose that the closest and farthest radial range distances of the target region are r_{min} and r_{max}, respectively. The first echoed signal arrives at the receiving radar at the fast-time

$$T_s = \frac{2r_{min}}{c}$$

The echo signal from the farthest reflector in the target region terminates at the fast-time

$$T_e = \frac{2r_{max}}{c} + T_p$$

Thus the fast-time interval over which the fast-time measurements of the SAS signal were

recorded was

$$t \in \left[T_e, T_f\right]$$

The range gate $[r_{min}, r_{max}]$ was determined from the beamwidths of the transducers in the range and cross-range directions. A general expression for the range gate in terms of the largest range swath is given by [1]

$$[X_c - X_{0max}, X_c + X_{0max}]$$

where X_c is the midpoint of the target region in the range direction and $2X_{0max}$ is the maximum size of the range swath. For a transducer with effective diameter D_x in the range direction, the half-size of the maximum range swath is

$$X_{0max} \approx \frac{X_c \lambda_{max}}{D_x}$$

The maximum half-beamwidth in the cross-range domain for a transducer with diameter D_y in the cross-range is given by

$$B_{ymax} \approx \frac{(X_c + X_{0max})\,\lambda_{max}}{D_y}$$

Therefore, the maximum sonar footprint of the transducers defines the range gate $[r_{min}, r_{max}]$ via

$$\begin{aligned} r_{min} &= X_c - X_{0max} \\ r_{max} &= \sqrt{(X_c + X_{0max})^2 + B_{ymax}^2} \end{aligned}$$

Fast-time Sample Spacing

The fast-time sample spacing must satisfy the Nyquist criterion for bandpass signals, which is that the fast-time sampling rate must be greater that twice the bandwidth of the signal therefore the fast-time sampling interval is

$$\triangle_t < \frac{1}{2B_t}.$$

The number of fast-time samples therefore within the fast-time gate $t \in \left[T_e, T_f\right]$ is

$$N = 2\left\lceil \frac{T_e - T_s}{\triangle_t} \right\rceil$$

where $\lceil x \rceil$ denotes the smallest integer which is larger than x. This operation might increase the duration of the fast-time gate such that if the sampling start time is kept fixed, the end time becomes

$$T_e = T_s + (N-1)\,\triangle_t$$

In the SAS simulation, a fast-time sampling rate of 40kS/s was chosen which was 10 times the signal bandwidth.

Fast-time baseband conversion

The simulated SAS returns which are time-shifted- and phase-shifted versions of the chirp pulse as a result of the target reflectivity properties was converted to baseband by multiplication with the phase function $e^{-j2\pi f_c t}$. This strips away the carrier component from the SAS returns so that fast-time frequency interval of the SAS returns becomes $f \in [-B_0, B_0]$.

Fast-time compression via Inverse Filtering

In the simulations, the frequency response of the transducers were assumed to be ideal and were thus not included in the simulations. Fast-time pulse compression was carried out by inverse filtering. The inverse filter was designed from a baseband version of transmitted chirp pulse shifted by some time $T_c = \frac{2X_c}{c}$, which corresponds to the two-way propagation delay of a point target at the centre of the swath that is at coordinates $[X_c, 0]$. After inverse filtering, the compressed pulse has a -3-dB width of $\delta t = {}^{0.89}/_{B_t}$. This corresponds to a range resolution of $\delta x = {}^{0.89c}/_{2B_t} = 3.78$ cm.

5.3.2 Slow-time Domain Sampling

The slow-time Doppler support of a stripmap SAS signal at a given fast-time frequency is [1]

$$k_u \in \left[-2k \cdot sin\phi_{d(y)}, 2k \cdot sin\phi_{d(y)}\right]$$

where $k = {}^{2\pi f}/_{c}$ is the Doppler wavenumber and $\phi_{d(y)}$ is the divergence angle (or beamwidth) of the transducer. This support is a baseband region in the slow-time Doppler domain and therefore the Nyquist sampling constraint in the synthetic aperture u domain applies, that is

$$\triangle_u \leq \frac{2\pi}{4k \cdot sin\phi_d} = \frac{\lambda}{4sin\phi_d}$$

In the case of a transducer with diameter D_y in the cross-range direction, the divergence angle is approximated by

$$\phi_d = \arcsin\left(\frac{\lambda}{D_y}\right)$$

Therefore the slow-time Nyquist sampling criterion becomes

$$\triangle_u \leq \frac{D_y}{4}$$

The transducers were 16mm in diameter including the external casing, but a circular aperture of diameter of 14mm. This translates to a slow-time sampling interval of $\triangle_u \leq$

3.5mm. This criterion is satisfied by the system because the step size of the motor used in this work was measured to be about 1.235mm.

5.4 SAS Image Reconstruction

5.4.1 2D SAS Image Reconstruction: Accelerated Chirp Scaling Algorithm

The accelerated chirp scaling algorithm [21], derived from the chirp scaling algorithm [24, 16, 17] was implemented in the simulation to reconstruct a SAS image of a scene. The main difference between the two algorithms is that while the latter works on raw SAR data, the former works on fast-time compressed synthetic aperture data. This algorithm was chosen because of its use of only phase multiplies and Fourier transforms (implemented digitally as fast fourier transforms (FFTs)) to reconstruct a scene unlike the range-doppler algorithm that requires interpolation which is both computationally intensive and prone to numerical errors. The accelerated chirp scaling algorithm therefore provides a fast and accurate synthetic aperture image reconstruction.

Chirp scaling as a synthetic aperture imaging technique removes the range variance of the target impulse responses by scaling the phase centers of all target echoes so that they all follow the same locus in the range-Doppler domain. In the original chirp scaling algorithm developed by [16, 17] the range chirps due to the echoes of the transmitted chirp pulse are used to carry out chirp scaling. However the accelerated chirp scaling algorithm developed by [21] uses the uncompensated secondary range compression (SRC) linear FM signal in the range-Doppler domain of the pulse compressed data to perform chirp scaling. It begins with a Fourier transform of the range compressed data in the cross-range direction to yield the range-Doppler domain. Then the phase centers of the target responses away from a chosen reference range are chirp scaled so that their loci are identical to that of the reference range. The rest of the algorithm then follows the chirp scaling algorithm without the unnecessary pulse compression phase multiply. Fig. 5.1 shows a flowchart of the accelerated chirp scaling algorithm. Refer to the cited literature in this section for the detailed derivation of the algorithm.

Given a transducer with diameter D_y in the cross-range domain, the theoretical cross-range resolution after 2D processing is $D_y/2$. With an effective diameter of 14mm, the theoretical resolution of the SAS system in the cross-range domain is 7mm. In simulating the 3D SAS system, the 2D stripmap SAS data acquired from each receiving transducer in the transducer array was processed using the accelerated chirp scaling algorithm to obtain a 2D stripmap SAS image of the target region. The stack of 2D processed SAS images were then coregistered prior to 3D focusing.

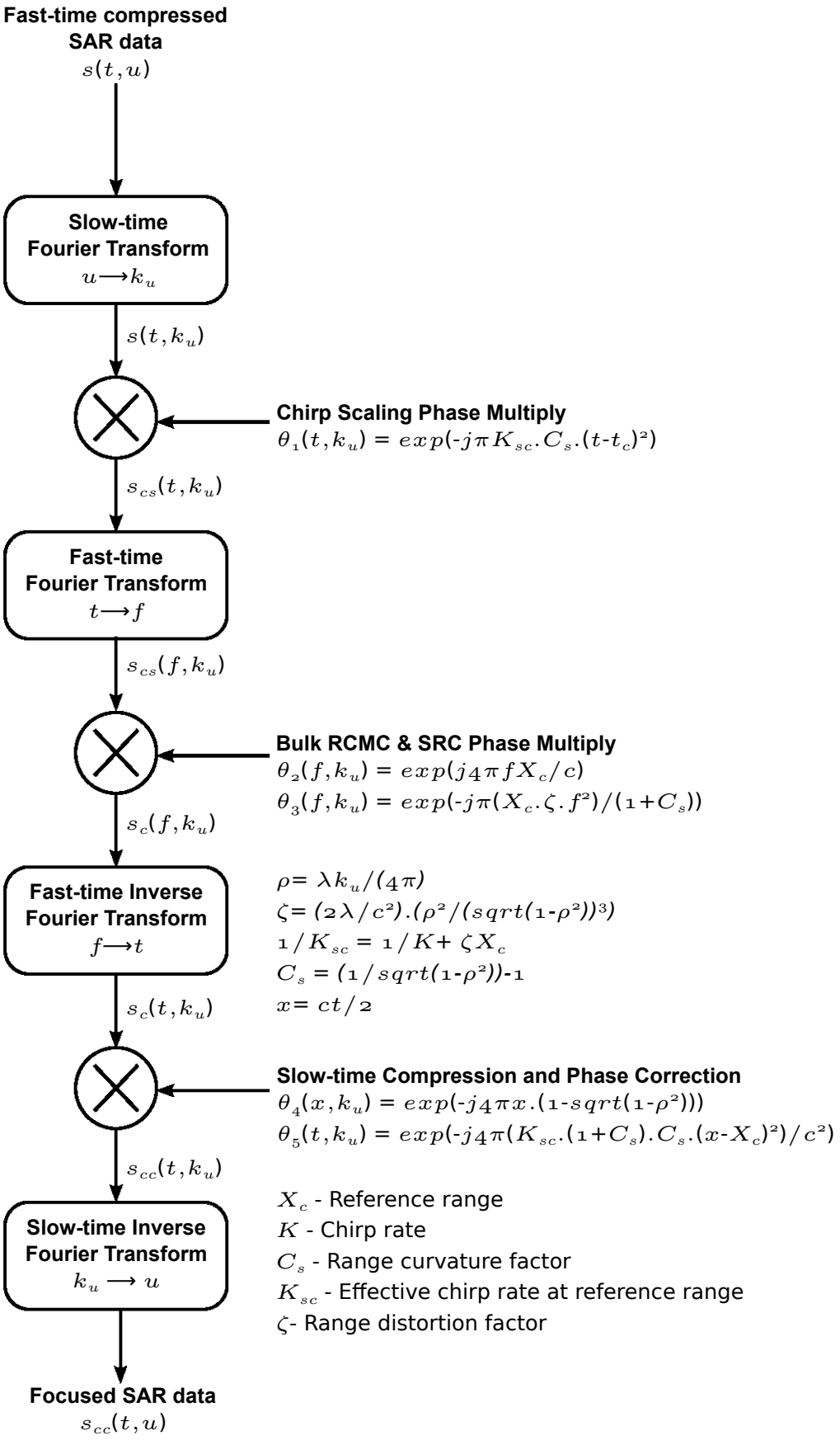

Figure 5.1: Block diagram of the accelerated chirp scaling algorithm .

5.4.2 Image Registration

Two SAS images of the same scene obtained from different viewing angles will need to undergo geometrical alignment in order to obtain certain information about the scene. This geometrical alignment is called image registration. Geometric errors between two SAS images arise as a result of variations in acquisition geometry such as altitude and velocity to mention a few. These distortions can generally result in translation, rotation, scaling, stretching and shearing in one image with respect to the other. Image registration is a vital step in interferometric synthetic aperture imaging which is used to obtain high-resolution digital elevation maps (DEM) in remote sensing applications. An incorrect alignment of two images even on a subpixel basis causes a coherence loss between the two signals and this coherence loss has a large impact on the quality of the final DEM [39]. Image registration is also important for 3D synthetic aperture imaging using compressive sampling, because the technique assumes that the returns of a target lies in the same azimuth-range cell in a stack of 2D images. An image registration algorithm therefore seeks to transform one image such that its pixel positions align with or are represented by the same pixel positions in another image. The image used as a reference is called the reference or master image and it is left unchanged. The image to be transformed is called the slave image. In general, the registration process is performed in two steps [40]:

1. Coarse matching: where the integer shifts (the whole-number of pixels) between the two images in the range and azimuth is computed.

2. Fine matching: where the computed shifts in range and azimuth are sub-pixelic (fractions of one pixel).

There are numerous image registration algorithms with each suited for a specific purpose [41]. These algorithms differ in the type of distortion they are designed to correct, the information (magnitude, phase, edges, segments or regions) in the images that is to be used for matching, the metric of similarity between the two registered images. The details of the various algorithms is outside the scope of this work, the reader is referred to [41, 39, 40] for a description of different image registration algorithms.

In selecting a suitable image registration algorithm one must consider the application for which image registration is required. In addition to the requirements aforementioned, some applications require phase-preserving image registration algorithms. For instance in interferometric synthetic aperture imaging, image registration must be phase preserving since the phase is used to obtain DEMs. Likewise, the compressive sampling techniques uses the phase of the images to reconstruct the reflectivity profile in the elevation direction so therefore any image registration algorithm must preserve the phase of the registered images. A survey of different image registration algorithms led to the discovery of the FFT-based image registration algorithm by [42]. It is a correlation based algorithm that uses the correlation between the two images for registration. This algorithm was chosen for image registrations because it was fast and accurate.

The registration algorithm [42] is implemented as MATLAB function with three inputs: the master image, the slave image and the sub-pixel accuracy required. It produced five main outputs: the normalised root mean square error between the two images, the global phase difference, the number of column shifts executed, the number of row shifts executed and the Fourier transform of the registered image. In the simulation, the 2D SAS magnitude-image obtained from the middle transducer in the array was chosen as the master image and the magnitude-images from the other transducers along the elevation baseline were chosen as slaves. The image registration was however performed manually by using two of the outputs of the registration function: the number of column and row shifts required. The registration was performed by multiplying the slave image by phase functions derived from the number of row and column shift in the 2D frequency domain (that is the Doppler range-frequency domain). So that the registration affects both the magnitude and phase of the slave image. A sub-pixel accuracy of 1/10 was chosen as this is the typical value used in image registration [43]. All registered images were stacked together for the final stage of the 3D reconstruction.

5.4.3 3D Image Reconstruction: Inverse Fast Fourier Transform

After registering and stacking the 2D SAS images, the pixels in the same range-azimuth resolution cell form a 15-element one-dimensional array whose generic form is given by (3.3) and rewritten here for convenience

$$g(s_p) = e^{-j\frac{4\pi}{\lambda}\left(x+s_{\parallel p}\right)} \int_{-Z_0}^{Z_0} \gamma(z) e^{-j\frac{2\pi}{\lambda x}\left(z-s_{\perp p}\right)^2} dz$$

The quadratic phase term in the equation is a distortion factor that is compensated for by deramping, which is implemented by multiplying the 15-element array by the phase term of a reference target at the centre of the elevation swath. After deramping, the equation of the array becomes

$$g(s_p) = \int_{-Z_0}^{Z_0} \gamma(z) e^{-j\frac{2\pi}{\lambda x}z^2} e^{j\frac{4\pi s_{\perp p}}{\lambda x}z} dz$$

As was shown in Section 3.1 by assuming that the quadratic phase term is absorbed into the reflectivity function $\gamma(z)$, the reflectivity profile in the elevation direction can be recovered by taking the inverse fourier transform of the data.

$$g(s_p) = \int_{-Z_0}^{Z_0} \tilde{\gamma}(z) e^{j2\pi\frac{2s_{\perp p}}{\lambda x}z} dz = \int_{-Z_0}^{Z_0} \tilde{\gamma}(z) e^{-j2\pi\xi_p z} dz = \mathscr{F}\left\{\tilde{\gamma}(z)\right\}|_{\xi_p}$$

where $\xi_p = -2s_{\perp p}/\lambda x$ is the spatial elevation frequency.

To appreciate the resolution capabilities of the compressive sampling technique, we perform elevation reconstruction simulations using this FFT-based techniques. The stack of registered 2D SAS images are assumed to be obtained along a single-pass system with a total orthogonal baseline span of $2L_s = 28$cm. The theoretical resolution (-3dB width

of the point spread function) in the elevation direction (3.9) is $\triangle_z$ =2.4cm, which corresponds to a height resolution $\triangle_h = \triangle_z \sin\theta_v = 1.2$cm. With the chosen synthetic elevation spacing, the elevation half-extension of the ground scene using (3.8) is $Z_0 = 17$ cm.

5.4.4 3D Image Reconstruction: Compressive Sampling

For tomographic compressive sampling, selecting the super-resolution factor η and the regularization parameter, ε in (3.21) is important. In selecting the super-resolution factor, one must note that a higher super-resolution factor results in increased elevation resolution therefore large values of η are desirable. However increasing η also increases N_z according to (3.17) and also the minimum number of measurements, M_z required for reliable solution increases. The upper limit on η for a fixed value of M_z is given by [5]

$$\eta_{up} \leq \frac{\lambda X_c}{8L_s \cdot Z_0} \exp\left[\left(\frac{M_z}{C \cdot S}\right)^{1/4}\right] \tag{5.2}$$

where C is a constant that depends on the measurement and sparsity matrixes Φ and Ψ, and it can be empirically estimated by numerical simulations [5]. In this work, $C \approx 0.714$.

The regularization parameter ε controls the tradeoff between the sparsity of the solution and the closeness of the solution to the measured data. It is therefore an important to select a suitable value because if not properly set then the optimization problem in (3.21) will either not fully reconstruct the sparse vector α and omit some targets or it will falsely represent significant portion of the noise as targets in the scene. When the additive noise is zero mean and Gaussian with variance σ^2 a good selection which makes the true α feasible with high probability is [5]

$$\varepsilon = \sqrt{2\log N_z}\sigma \tag{5.3}$$

In the simulation, the optimization problems (3.16) and (3.21) were solved numerically using SPGL1, a solver for large-scale sparse reconstruction [34, 35]: a MATLAB toolbox that solves basis pursuit, basis pursuit denoising and Lasso problems even on complex variables. Fig. 5.2 shows the block diagram of the algorithm used for compressive sampling reconstruction.

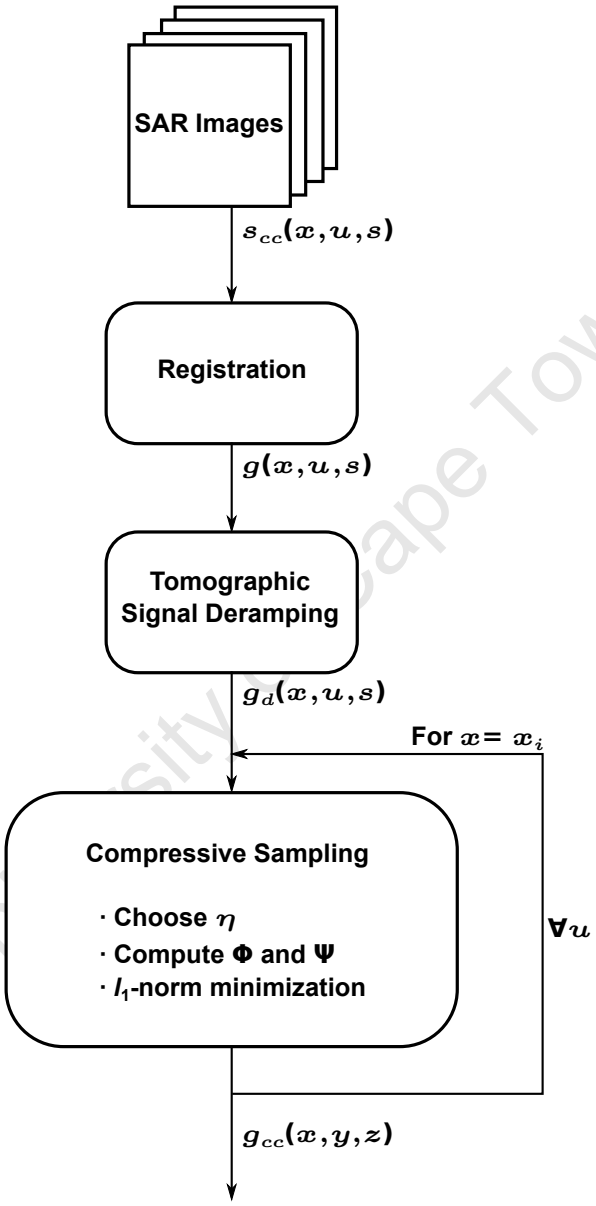

Figure 5.2: Block diagram of the compressive sampling processing.

Chapter 6

Three-dimensional SAS Simulation Results and Discussion

In this chapter the results of a 3D SAS simulation written in MATLAB are presented. It serves to illustrate the processing required for 3D SAS image reconstruction as described in Chapter 3 and to serve as a standard against which results from the actual SAS system can be compared.

6.1 The Transmitted Pulse

Fig. 6.1a & 6.1b show the transmitted chirp pulse in the time and frequency domain respectively simulated at a fast-time sampling rate of 40 kS/s which is $10B_t$. From the figures the duration ($T_p = 0.05\,\text{s}$), the centre frequency ($f_c = 40\,\text{kHz}$) and the bandwidth ($B_t = 4\,\text{kHz}$) of the pulse are clearly visible.

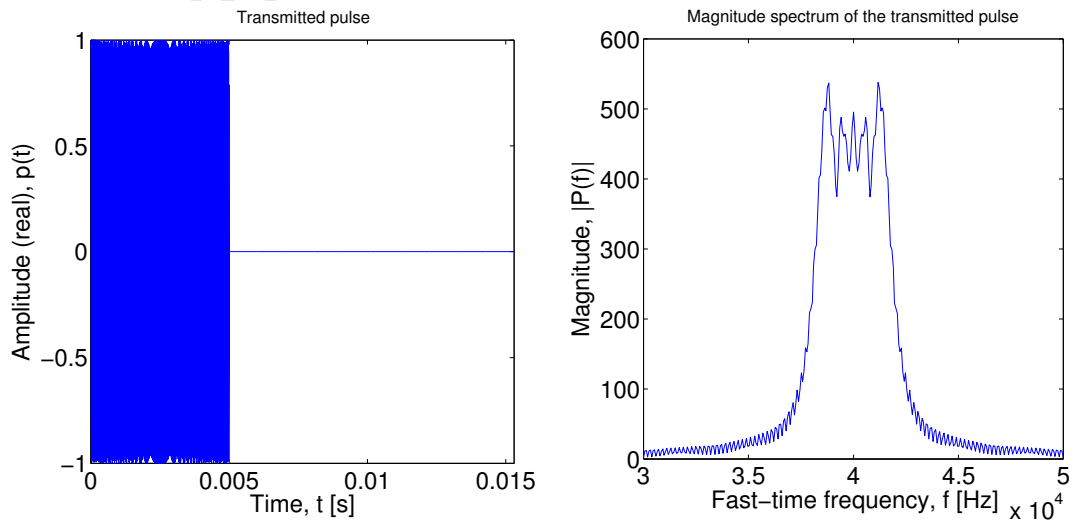

(a) (b)

Figure 6.1: The simulated chirp pulse in the (a). time domain and (b). frequency domain

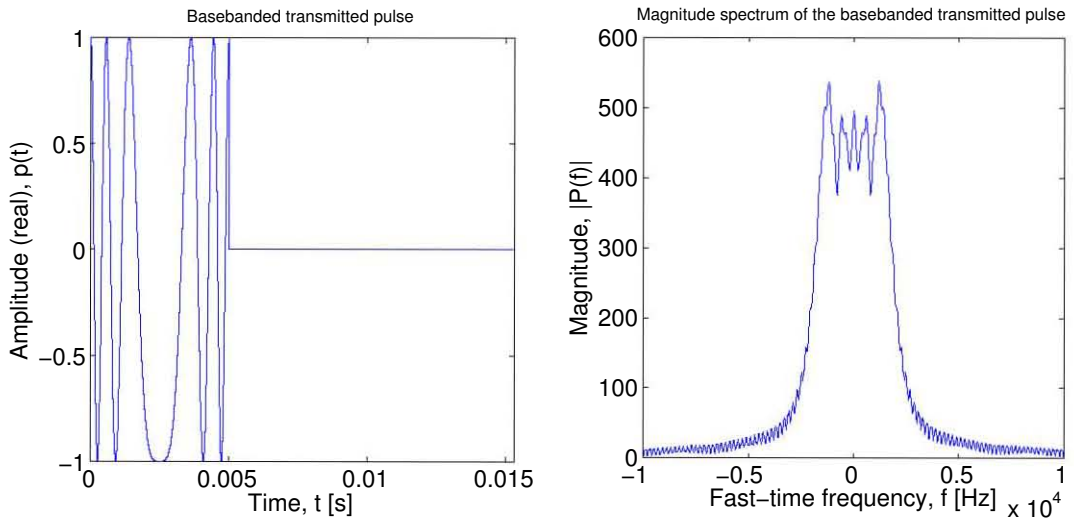

(a) (b)

Figure 6.2: Basebanded chirp pulse in the (a). time domain and (b). magnitude spectrum

In the baseband version of the chirp pulse (Fig. 6.2a & 6.2b), the chirp pulse has been stripped of the carrier and is now centred on 0 Hz.

6.2 Two-dimensional SAS Imaging

The results of 2D SAS imaging are presented to illustrate the SAS imaging concept as well as demonstrate the effectiveness of the chirp scaling algorithm in SAS image reconstruction. In the 2D SAS geometry, only one receiver and one transmitter are used.

6.2.1 Single Target Simulation

The Target Region

Fig. 6.3 shows the simulated target region in the 3D and azimuth-range domains containing a single target located at the centre of the scene $[X_c, Y_c, Z_c]$. The target region falls within the interval $[X_c - X_0, X_c + X_0]$ in range where X_c = 2m, X_0 = 0.5m and within $[Y_c - Y_0, Y_c + Y_0]$ in the cross-range where Y_c = 0m and Y_0 = 0.5m, and within $[Z_c - Z_0, Z_c + Z_0]$ in elevation where Z_c = 0m and Z_0 = 0.2125m as computed using (3.8). This is therefore a broadside target region since it is centred on zero in the cross-range domain that is Y_c = 0. The target in the scene was set to have a complex reflectivity of unity.

The SAS data and range compression

In typical 2D SAS imaging, SAS data is recorded along a single baseline using one sensor. Fig. 6.4a is an image of the simulated response from the single target. The image is the real part of the basebanded echoed chirp signal that is received by the transducer as it

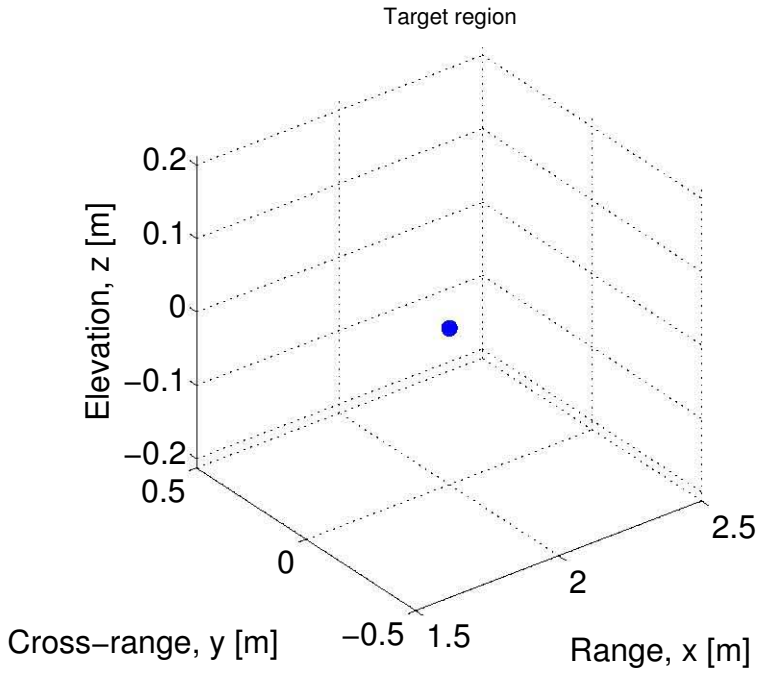

(a) 3D target region

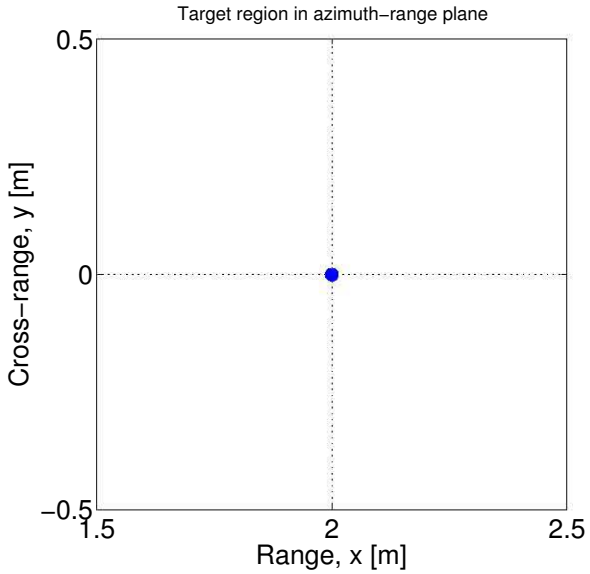

(b) Target region viewed in the azimuth-range domain

Figure 6.3: The simulated 2D target region with a single target placed at the centre of the scene

moves along the synthetic aperture (the vertical axis). Fig 6.4b shows the response from the target after pulse compression. One can observe the hyperbolic locus of the response that describes the variation in range to the target as a function of the position of the sensor along the synthetic aperture.

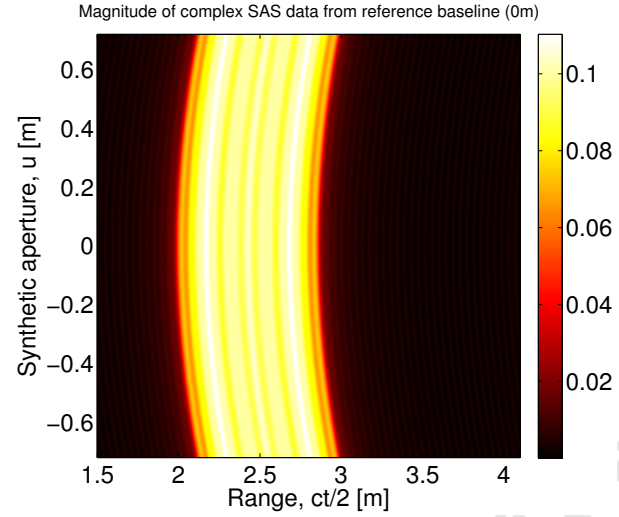

(a)

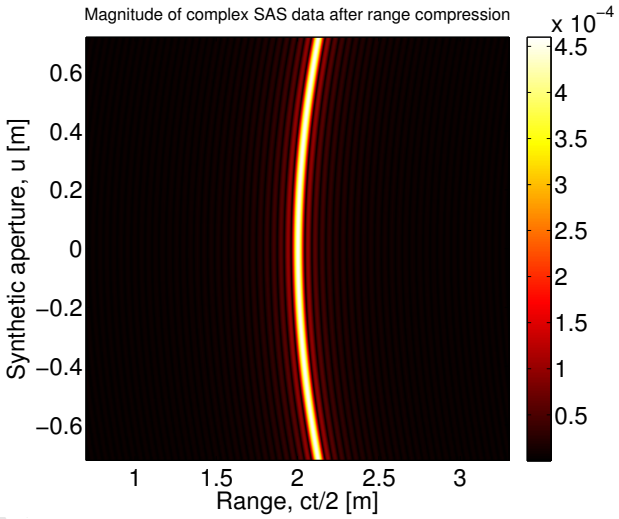

(b)

Figure 6.4: SAS response from the target scene containing a single target (a). The simulated response from a single target. (b). Pulse-compressed response from a single target

Pulse compression was achieved using the inverse filter designed from the transmitted chirp pulse as described in Section 4.2. Fig. 6.5 shows the magnitude and phase of the inverse filter designed from the chirp pulse in the frequency domain. Fig. 6.6 shows the magnitude and phase of the output of the inverse filter which was used to compress the SAS returns from the target at the centre of the target region. The magnitude of the output is the same as the sinc function as expected. Also the phase of the output is flat over the mainlobe. Note the unstable regions in the phase that is caused by small numerical deviations which causes the phase to jump rapidly between the interval $[-\pi, \pi]$. Since the impulse response of the transmitter and receiver were not included in the simulation,

there was no need to design an inverse filter to cancel out their effect on the SAS data during range compression.

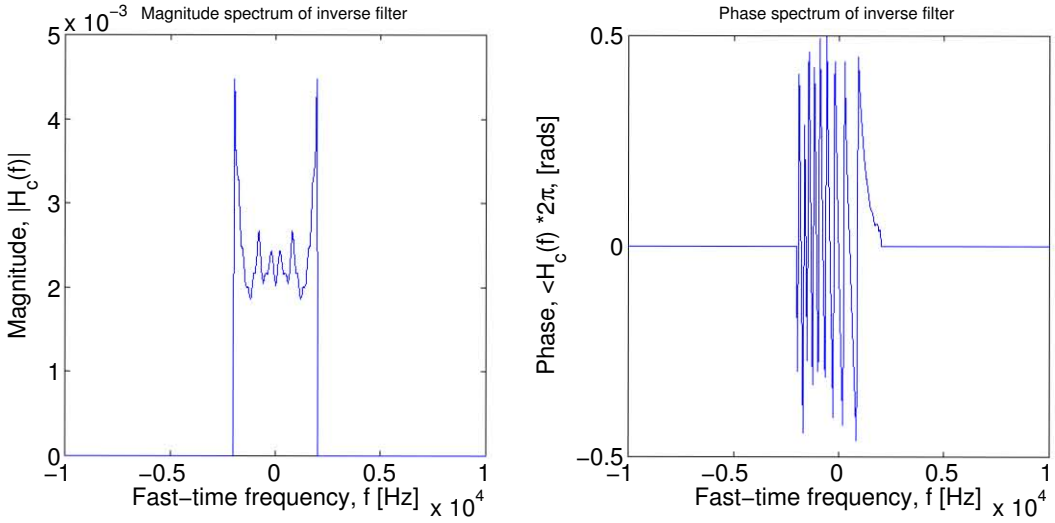

(a) (b)

Figure 6.5: The inverse filter designed from the transmitted pulse (a). Magnitude spectrum. (b). Phase

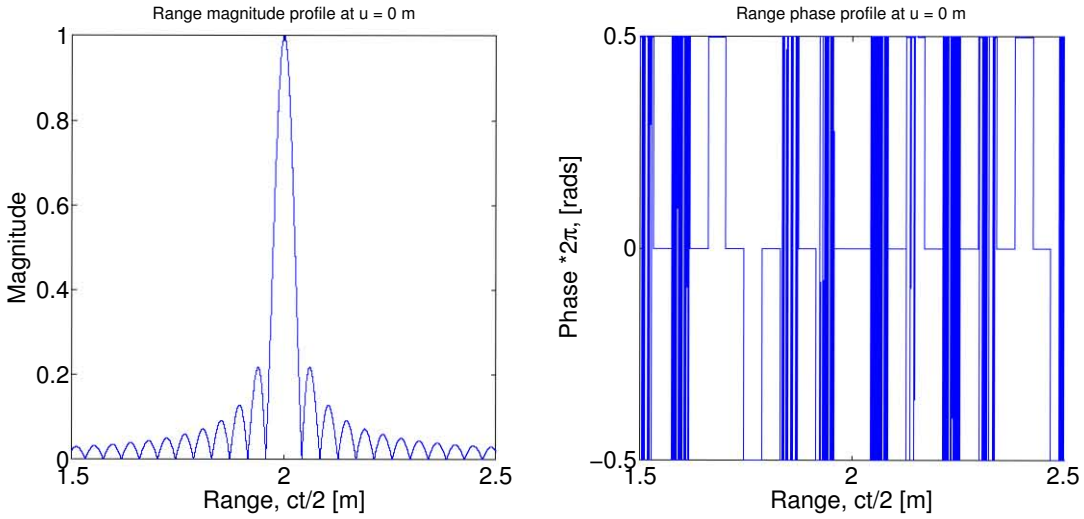

(a) (b)

Figure 6.6: The output of the inverse filter at $u = 0$ with one target at the centre of the scene.

2D SAS Image Reconstruction: Accelerated Chirp Scaling Algorithm

Fig. 6.7a shows the final 2D SAS image obtained using the accelerated chirp scaling algorithm. The image represents the magnitude of the complex SAS focused data. The point spread function is a two-dimensional sinc function in the range and cross-range directions with a range resolution of 3.74cm and a cross-range resolution of 1.24cm measured as width of the mainlobe of the sinc functions at the -3-dB point. Recall that the resolutions are dependent on the processed bandwidth in each domain (2.58 & 2.60). The

measured resolution in the range direction was close to the theoretical resolution (3.78 cm) with a processed bandwidth of 4kHz according to (2.45). In the cross-range domain, the measured resolution was greater than the theoretical resolution ($D_y/2 = 0.7$cm) because the processed bandwidth was less than theoretical. Fig. 6.8a shows the Doppler magnitude spectrum of the target after range migration correction to give an idea of the available doppler bandwidth that could be processed for cross-range focusing. A Doppler baseband-bandwidth of about 500 rad/m was available for processing however only 200 rad/m was used for cross-range image formation (Fig. 6.8b). This bandwidth was chosen as a compromise between the resolution and a satisfactory point target response in the cross-range direction. Fig. 6.7 also shows the range and cross-range profiles along the centre of the scene from which one can observe the high sidelobes of the point spread function as a result of the rectangular window function used in the reconstruction process. Note the flat phase response of point spread function in the cross-range domain. This is expected and essential for compressive sampling and other imaging techniques such as interferometry. The Hann window was used to reduce the sidelobes but this resulted in a broadening of the mainlobe (Fig. 6.9b & 6.9c) and thus a lower resolution SAS image (Fig. 6.9a). The new 3-dB widths (resolutions) were 5.87cm (56% increase) in range and 2.22cm (79% increase) in cross-range.

6.2.2 Multiple Targets Simulation

The Target Region

Fig. 6.10 shows the simulated target region in the 3D, azimuth-range and elevation-range domain with 15 targets. Some of the targets have the same range and azimuth coordinates but different elevations to demonstrate the impossibility of extracting height information from 2D SAS images. The targets were set to have the same amplitude and phase of reflectivity of unity. One target is placed at the centre of the scene $[X_c, Y_c, Z_c]$ while others are placed at different locations to demonstrate the resolution capability of the SAS system.

The SAS Data and Range Compression

Fig. 6.11a shows the simulated SAS response from all the targets. The image is the sum of the real parts of the chirp signals that is received by the transducer as it moves along the synthetic aperture. The distinct signatures from each target are not clearly visible, however after pulse compression the echos from the targets are compressed into a narrow pulse (Fig. 6.11b). The hyperbolic locus of the SAS returns from each target describes the variation in range to each target as the sensor moves along the synthetic aperture. Also observe the constructive and destructive interference caused by the interaction of the signatures from two or more targets.

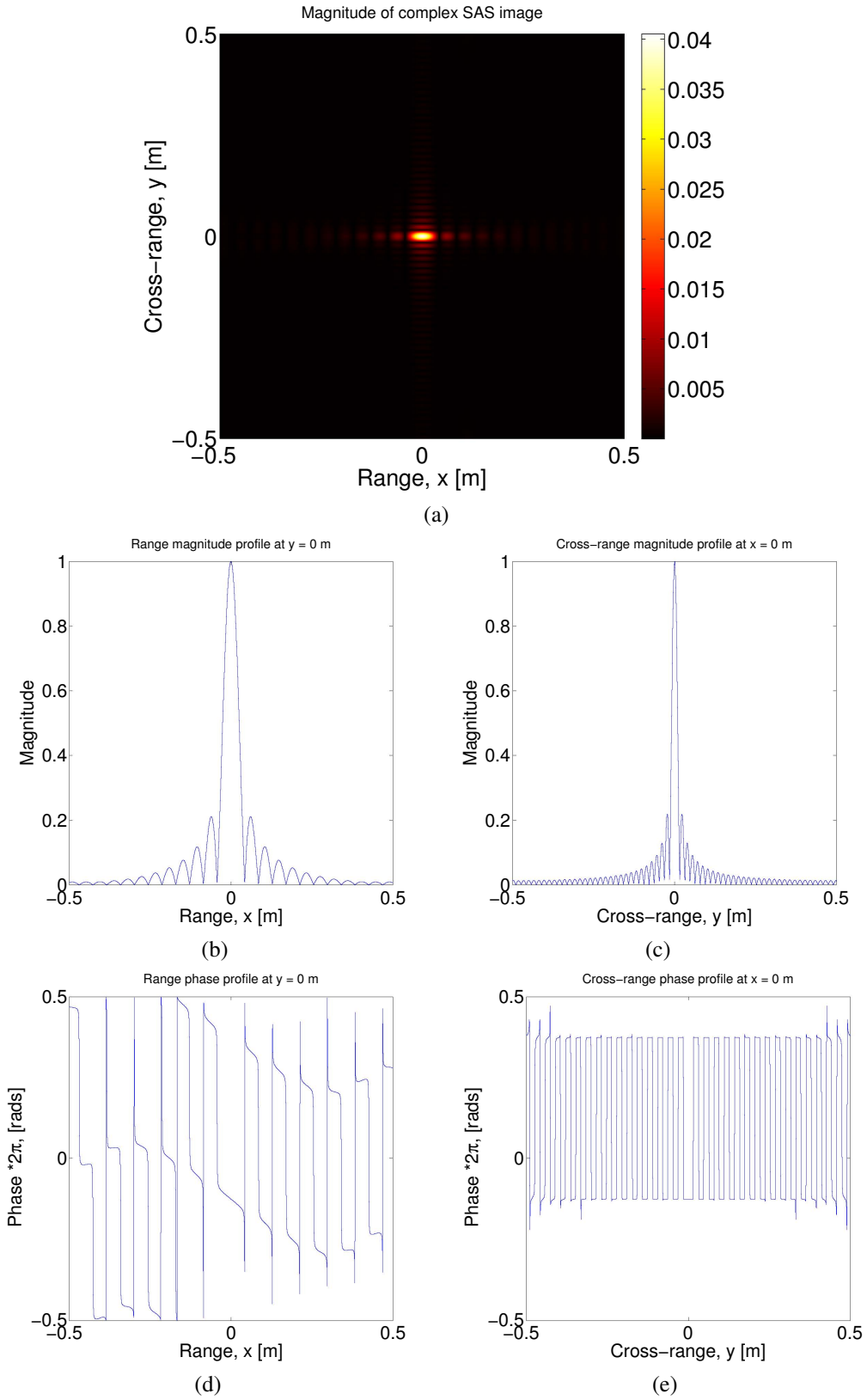

Figure 6.7: 2D SAS image and profiles of a target scene containing a single target. A rectangular window is used in both range and cross-range direction hence the high side-lobes in the image (a). 2D SAS image of a single target (b). Range magnitude profile (c). Cross-range magnitude profile (d). Range phase profile (e). Cross-range phase profile

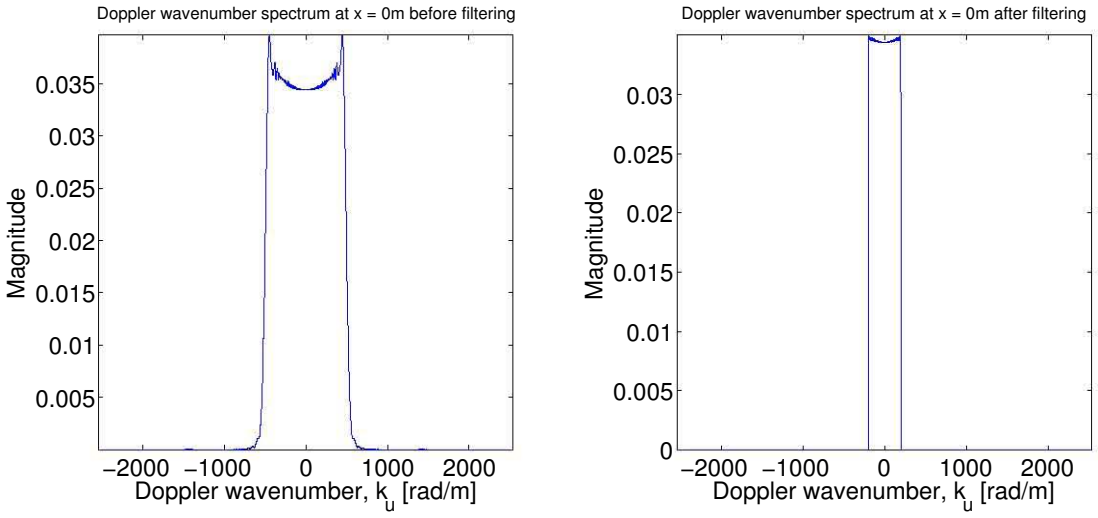

(a) (b)

Figure 6.8: Doppler magnitude spectrum of the target (a). available Doppler bandwidth (b). processed Doppler bandwidth

2D SAS Image Reconstruction: Accelerated Chirp Scaling Algorithm

Fig. 6.12 shows the final 2D SAS image obtained using the accelerated chirp scaling algorithm. The image represents the magnitude of the complex SAS focused data. The processed bandwidths in the range and cross-range directions were the same as those used for the case of a single target. A hann window was also used in the filtering process in both directions therefore the same resolutions were obtained. Notice that only five point spread functions are present in the 2D SAS image instead of 15. This is because the point spread functions from targets with the same range and azimuth coordinate but different elevations add constructively and map to the same azimuth-range pixel in the final 2D SAS image. Note also the flat phase response of point spread function in the cross-range domain. This phase contains the elevation information of each target in the given azimuth-range cell and will be useful in resolving the targets in the elevation direction.

6.3 Three-dimensional SAS Imaging

The simulation results of the elevation focusing using the FFT and the compressive sampling technique will now be presented. The elevation acquisition parameters used in this simulation were constrained by the properties of the real system to be tested. In this simulation the SAS signals are acquired along multiple passes (implemented as for loops) with a total orthogonal baseline span of about $2L_s = 16$cm to give a 3-dB theoretical elevation resolution of about $\triangle_z = 5.31$cm (3.9). The minimum possible separation between the centres of the transducers in the array is 1.6cm since this is the diameter of each tranducer. Therefore a baseline spacing of $\triangle_s = 2.0$cm was chosen which consequently translates to an elevation extension of the ground scene of $2Z_0 = 42.5$cm (3.8). With this sampling interval and orthogonal baseline span, the odd number of acquisitions required for

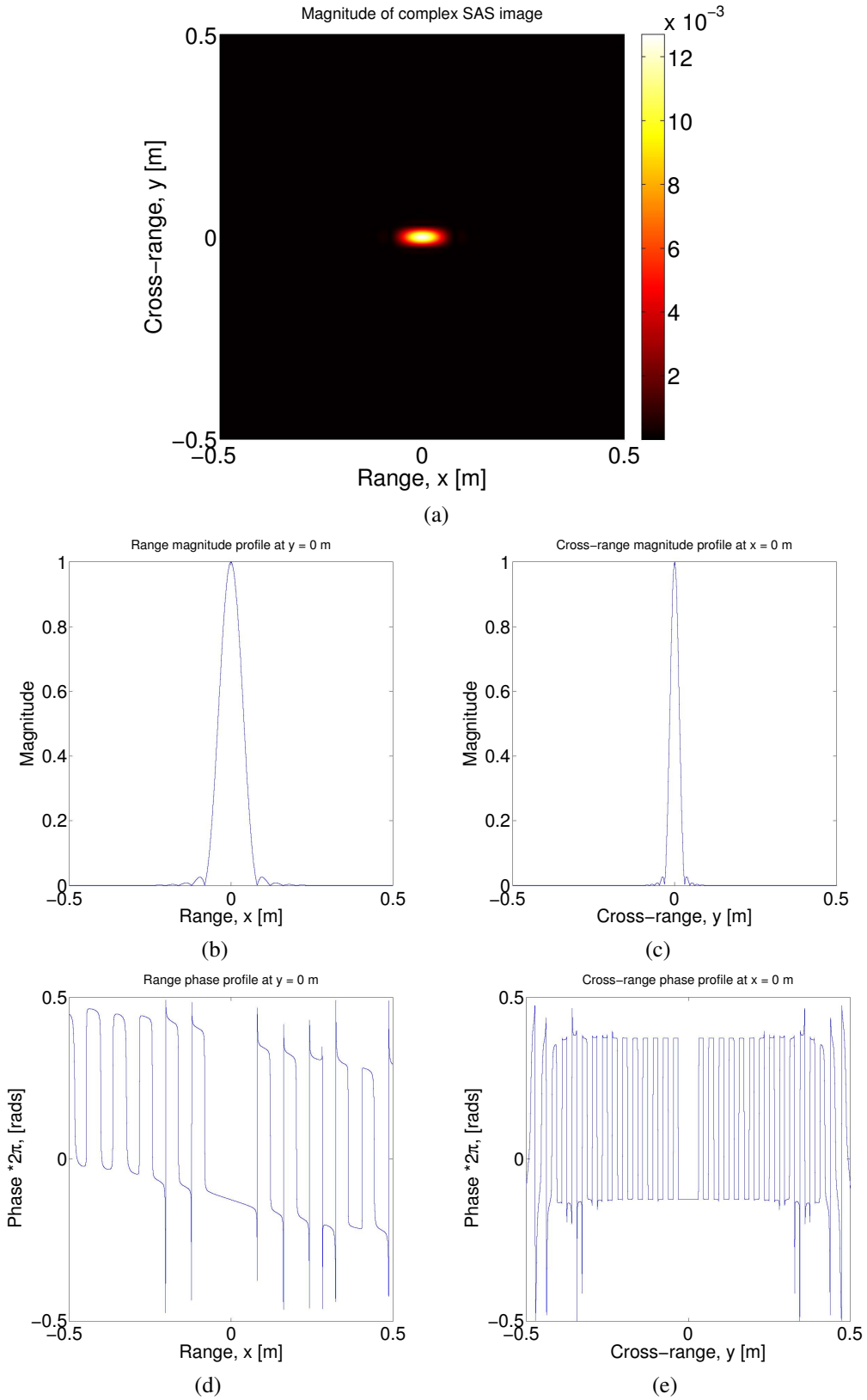

Figure 6.9: 2D SAS image and profiles of a target scene containing a single target. A Hann window is used in both range and cross-range direction which reduces the sidelobes but increases the -3dB width of the point spread function (a). 2D SAS image of a single target with lower resolution as a result of windowing. (b). Range magnitude profile showing 56% decrease in resolution. (c). Cross-range magnitude profile with 79% decrease in resolution. (d). Range phase profile (e). Cross-range phase profile

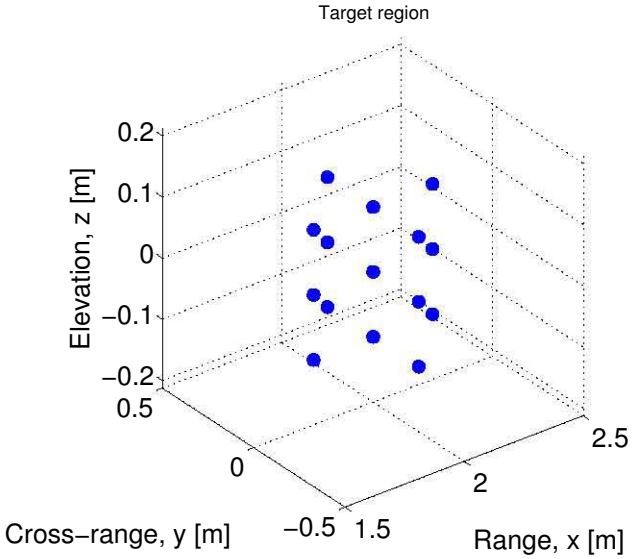

(a)

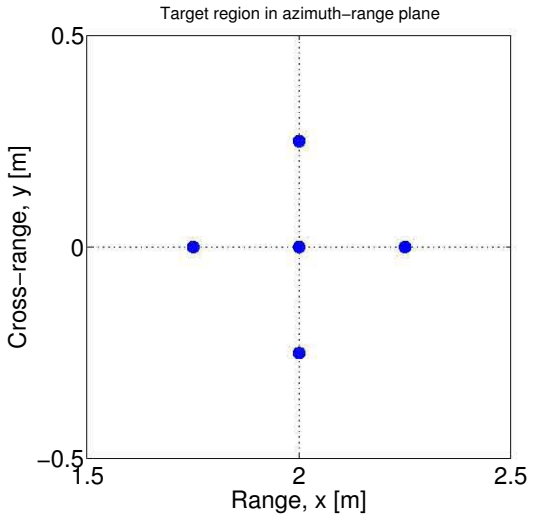

(b)

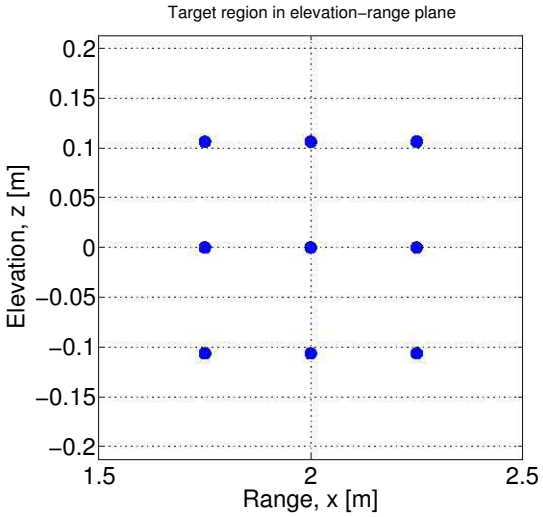

(c)

Figure 6.10: The simulated 2D target region with 15 targets. (a). 3D view (b). View in the azimuth-range plane (c). View in the elevation-range plane

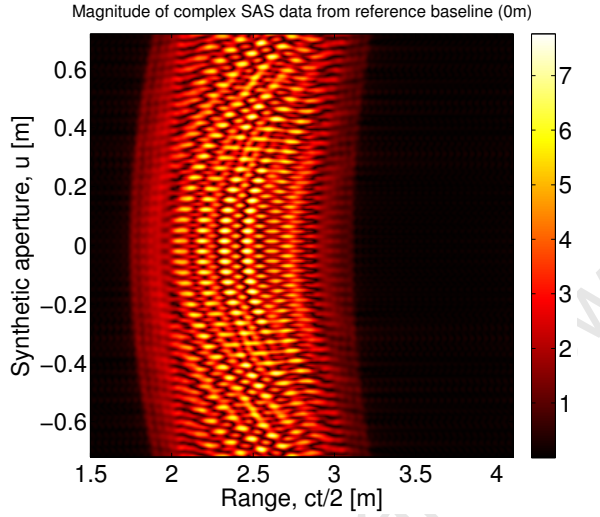

(a)

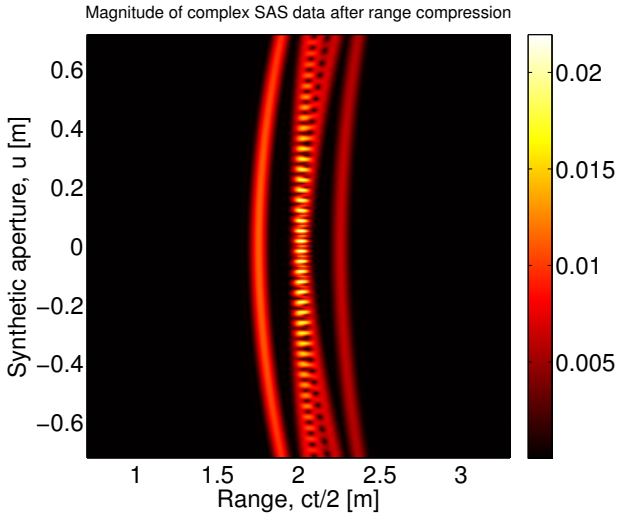

(b)

Figure 6.11: (a). The simulated response from multiple targets. (b). Simulated response after range compression

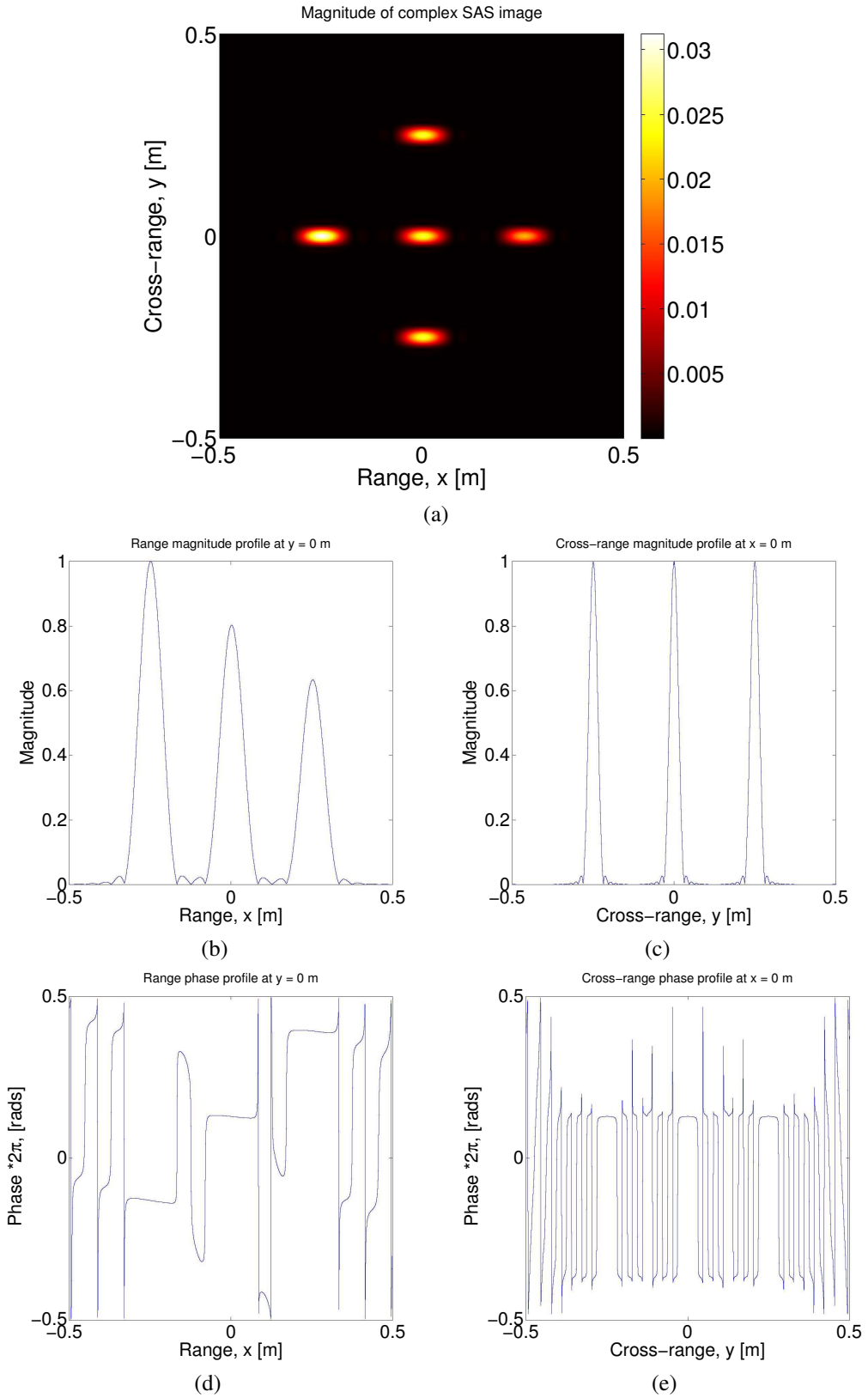

Figure 6.12: 2D SAS image and profiles of a target scene containing 15 targets. Some of the targets have the same range and azimuth coordinates but different elevations. A Hann window is used in both range and cross-range direction. (a). 2D SAS image without windowing (b). Range profile (c). Cross-range profile (d). Range phase profile (e). Cross-range phase profile

FFT-based reconstruction is 9 acquisitions which are uniformly spaced by 2cm.

6.3.1 Single Target: Zero-elevation

The Target Region

Fig. 6.13 shows the simulated target region in the different domains: 3D domain, azimuth-range domain, elevation-range domain and elevation-azimuth domain. A single target is placed at the centre of the scene with coordinates X_c, Y_c, Z_c where $Z_c = 0$m.

Image Registration

The 2D SAS images of the scene from all transducers were stacked into a 3D array. The image from the middle transducer was used a reference for image co-registration. Fig. 6.14 shows the 2D SAS data acquired from the reference orbit and the resultant 2D SAS image after 2D SAS processing illustrated in the preceding section. Similar images were obtained from the other orbits.

The processed 2D images from the other orbits were co-registered with respect to the reference image to 1/10 subpixel accuracy. To illustrate the image registration process, the range and cross-range profiles from the one of the outermost orbits before and after registration are shown in Fig. 6.15. Observe that the cross-range magnitude profile remains unchanged after registration. This is expected because the synthetic aperture sample points from each orbit are the same since there is no relative displacement of the sensors in the azimuth direction.

Deramping the Tomographic Elevation Signal

Fig. 6.16 shows the phase of the elevation signal before and after deramping as described in Section 5.4.3. Notice how the quadratic phase distortion is removed and only the residual video phase (3.4) remains. The residual phase is absorbed into the elevation model but can be compensated by a post-processing phase compensation in situations where phase preservation is vital.

Elevation Imaging via Inverse FFT

Fig. 6.17 shows the estimate of the elevation profile obtained by taking the inverse Fourier transform of the tomographic signal in the elevation direction and upsampling to improve visibility. The elevation resolution, measured as the 3-dB width of the mainlobe of the point spread function was 7.08cm which was about 33% higher than the theoretical resolution of 5.31cm. This is partly due to the use of the hann window.

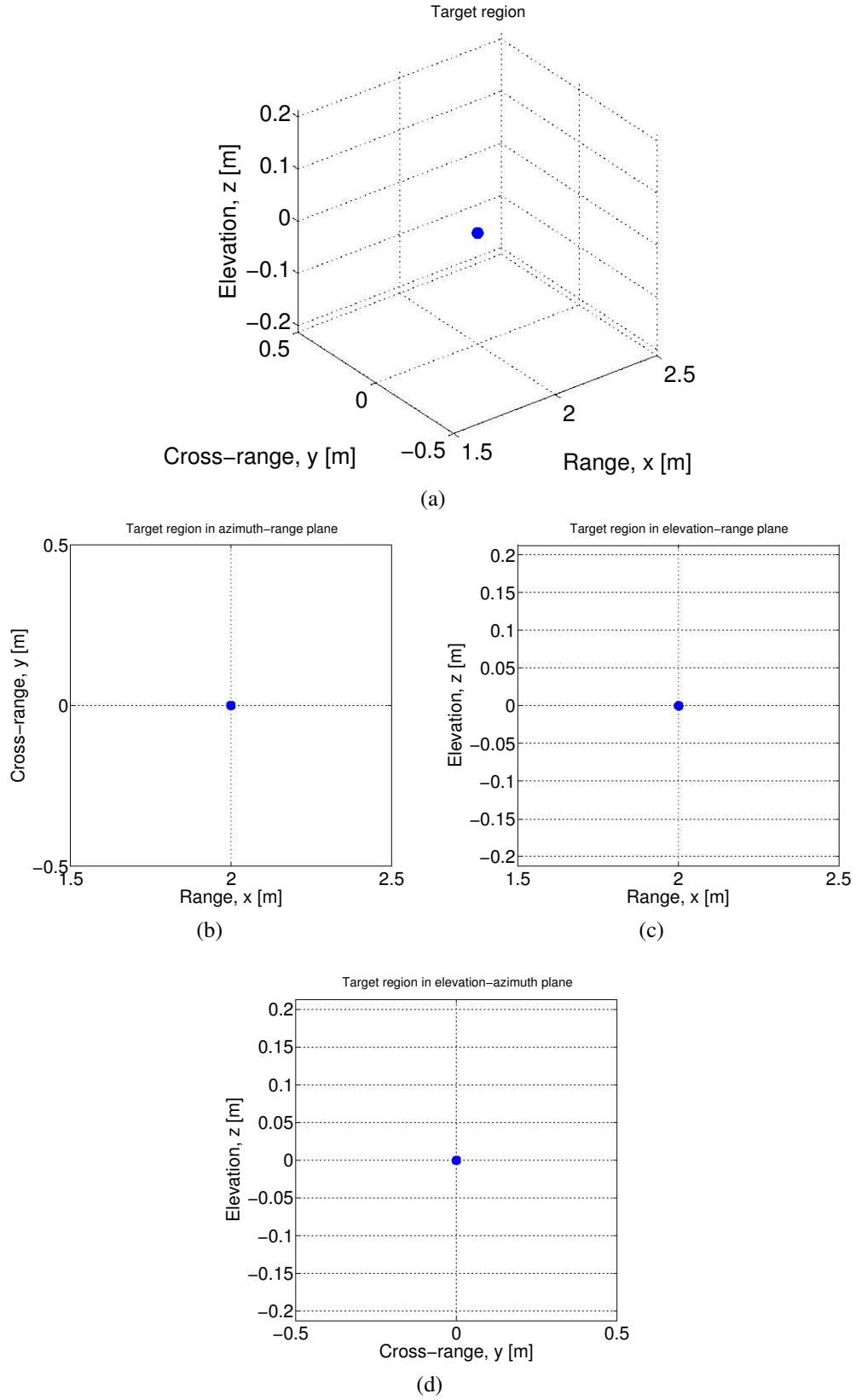

Figure 6.13: The simulated 3D target region with a single target placed at the centre of the scene

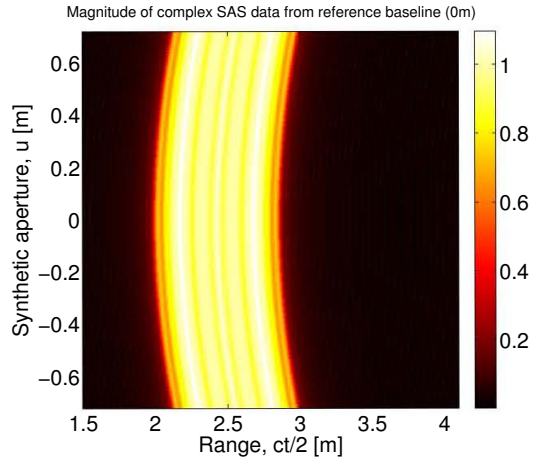

(a)

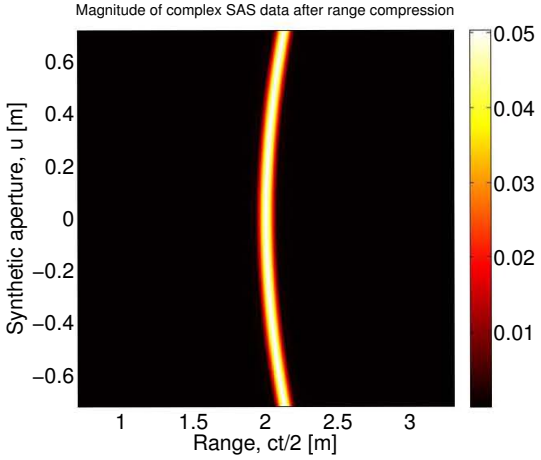

(b)

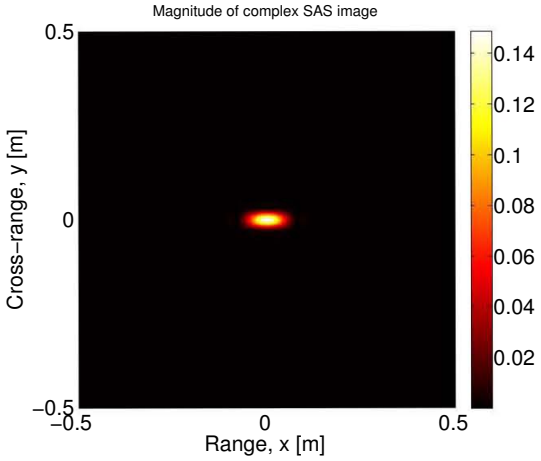

(c)

Figure 6.14: 2D SAS data from a single target as obtained by the reference baseline (a). raw data (b). range compressed data and (c). image from the reference orbit

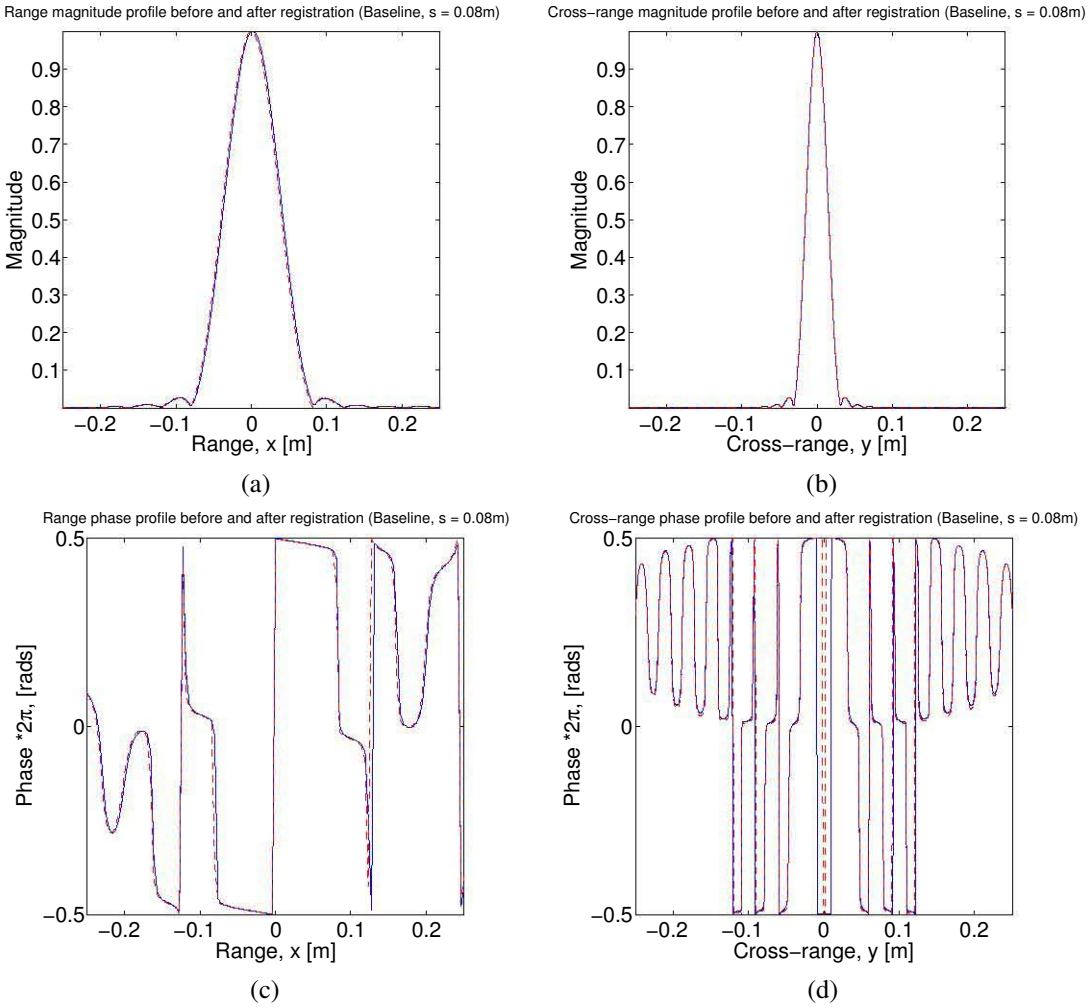

Figure 6.15: Profiles from the 9th orbit before (blue) and after (red-dashed) image registration (a). Range magnitude profile. (b). Cross-range magnitude profile. (c). Range phase profile. (d). Cross-range phase profile.

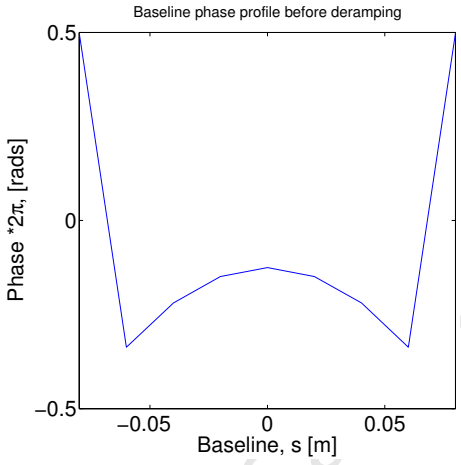

(a)

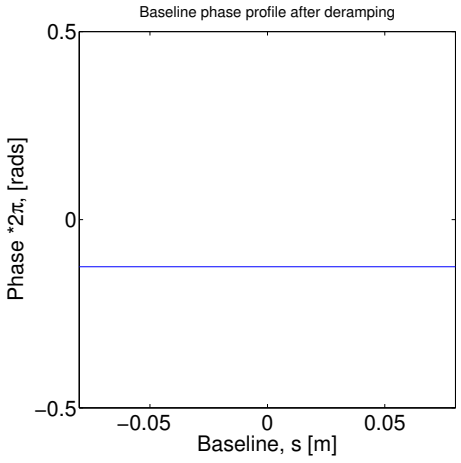

(b)

Figure 6.16: Phase of the tomographic signal (a) before deramping (b) after deramping

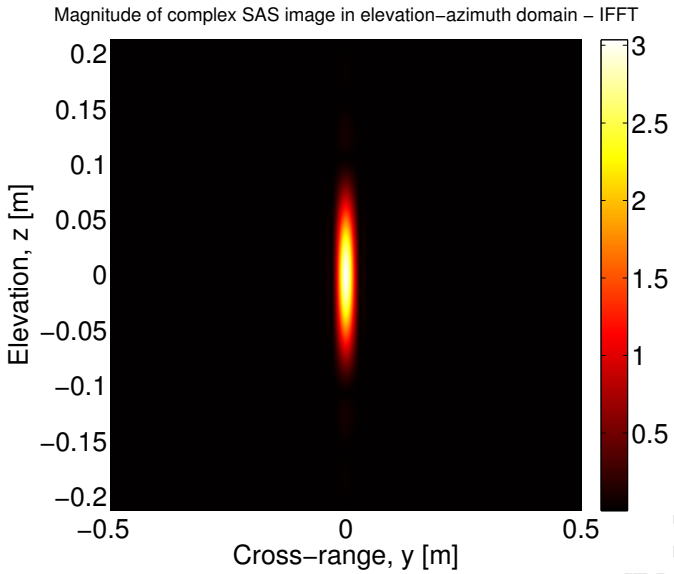

(a)

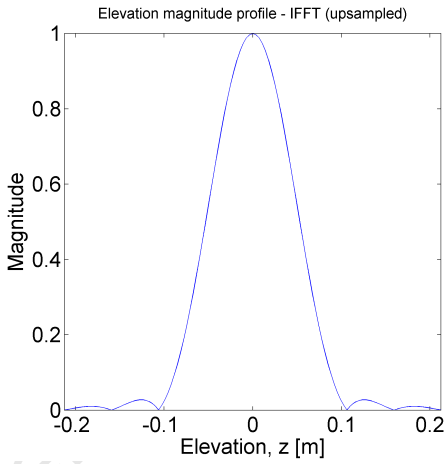

(b)

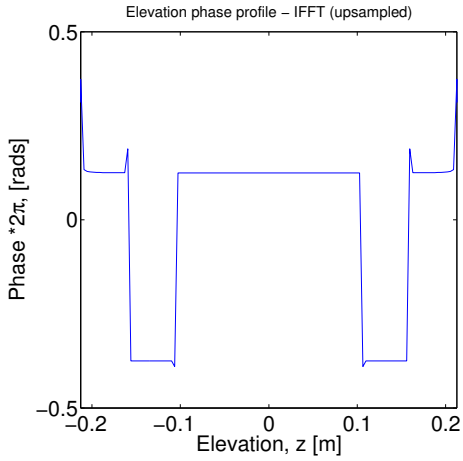

(c)

Figure 6.17: Reconstructed elevation image and profiles of point target in the elevation-azimuth domain using IFFT (a). The elevation image (b). The elevation magnitude profile (c). The elevation phase profile

Elevation Imaging using Compressive Sampling

l_1-norm minimization (3.16) was performed on each column of the registered-deramped-noiseless 3D SAS image to focus the image in the elevation direction using SPGL1. Fig. 6.18a & b show the elevation image reconstruction and the elevation profile respectively obtained with a super-resolution factor $\eta = 1$. Compressive sampling reconstructs spectal lines as opposed to sinc-like point spread functions [10]. However the visibility of the reconstructions can be improved by upsampling using sinc interpolation which is what was done in this case. Here CS detects a single spectral line. As expected the reconstruction was similar to that obtained using the FFT-based technique in the previous section. The compressive sampling technique exhibits good accuracy in reconstructing elevation profile at a given range. [5] obtained similar results when comparing the compressive sampling technique to the TSVD numerical method. The measured 3-dB width of the point spread function for a single target in the elevation direction was 6.38cm which is 20% larger than the nominal resolution. Notice that the resolution obtained from the CS reconstruction with $\eta = 1$ is 10% better than that obtained by the FFT technique. The super-resolution capability of the compressive sampling technique was explored by using a super-resolution factor of $\eta = 3$, which corresponds to an elevation resolution of $\delta z_{\text{sup}} = \triangle_z/\eta = 1.77$cm. Fig. 6.25 shows the reconstructed super-resolution SAS elevation image and it confirms that it is possible to achieve super-resolution using compressive sampling. The measured 3-dB width of the point spread function for the single target in the elevation direction was 2.13cm. This corresponds to a 3x improvement in resolution which is expected since the super-resolution factor was increased by the same amount.

6.3.2 Multiple Targets

The Target Region

Fig. 6.20 shows the simulated target region in different domains: 3D domain, azimuth-range, elevation-azimuth and elevation-range domain. Multiple targets with the same cross-range coordinates were set to have the same reflectivity amplitude. One target is placed at the centre of the range-elevation plane $[X_c, Z_c]$ where $Z_c = 0$, while others are placed at different locations to demonstrate the resolution capability of the 3D SAS system.

Image registration

Fig. 6.21 shows the 2D SAS data acquired from the reference baseline and the resultant 2D SAS image after 2D SAS processing illustrated in the preceding section. Similar images were obtained from the other baselines.

The processed 2D images from the other orbits were co-registered with respect to the reference image to 1/10 subpixel accuracy. To illustrate the image registration process,

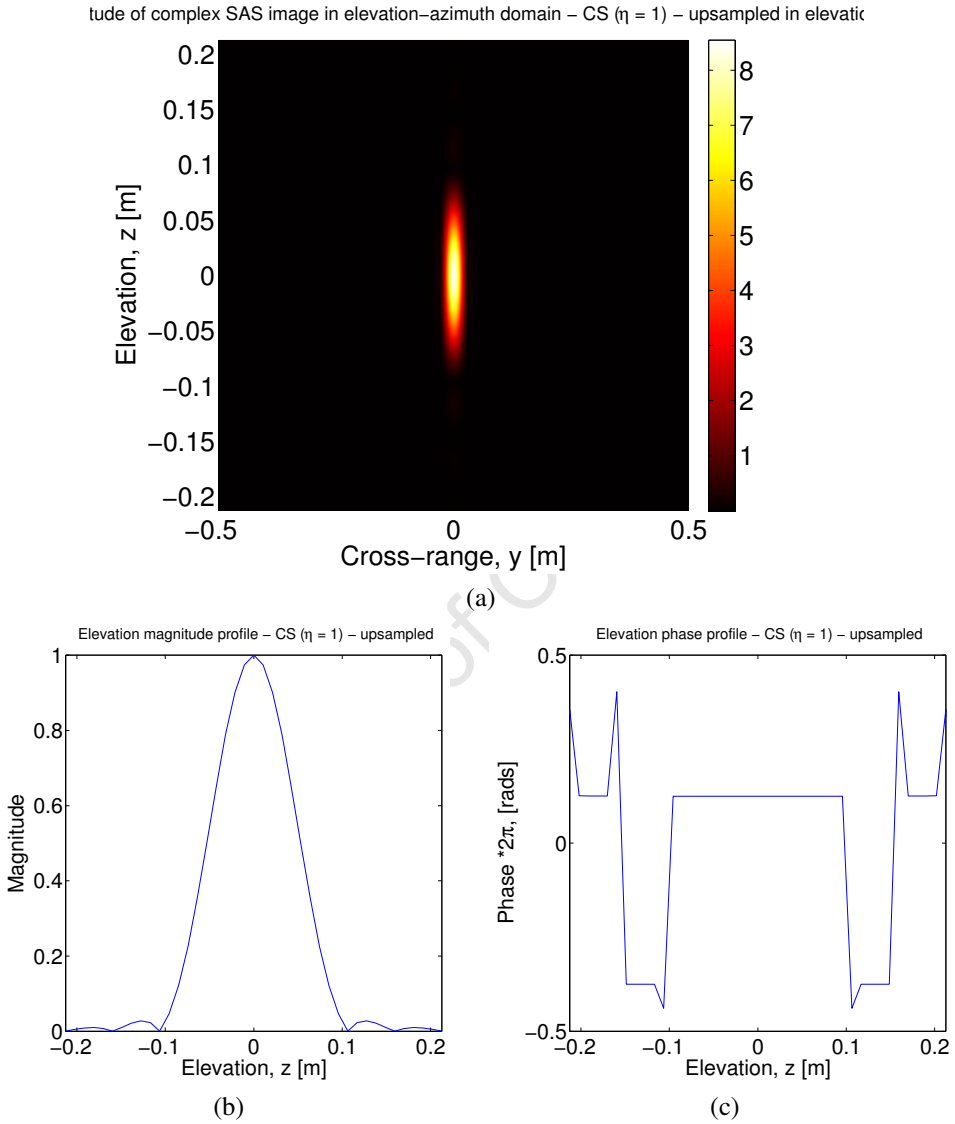

Figure 6.18: Reconstructed elevation image and profile of a scene containing a single point target at zero elevation using CS with $\eta = 1$. (a). Reconstructed elevation image. (b). The elevation magnitude profile (c). The elevation phase profile.

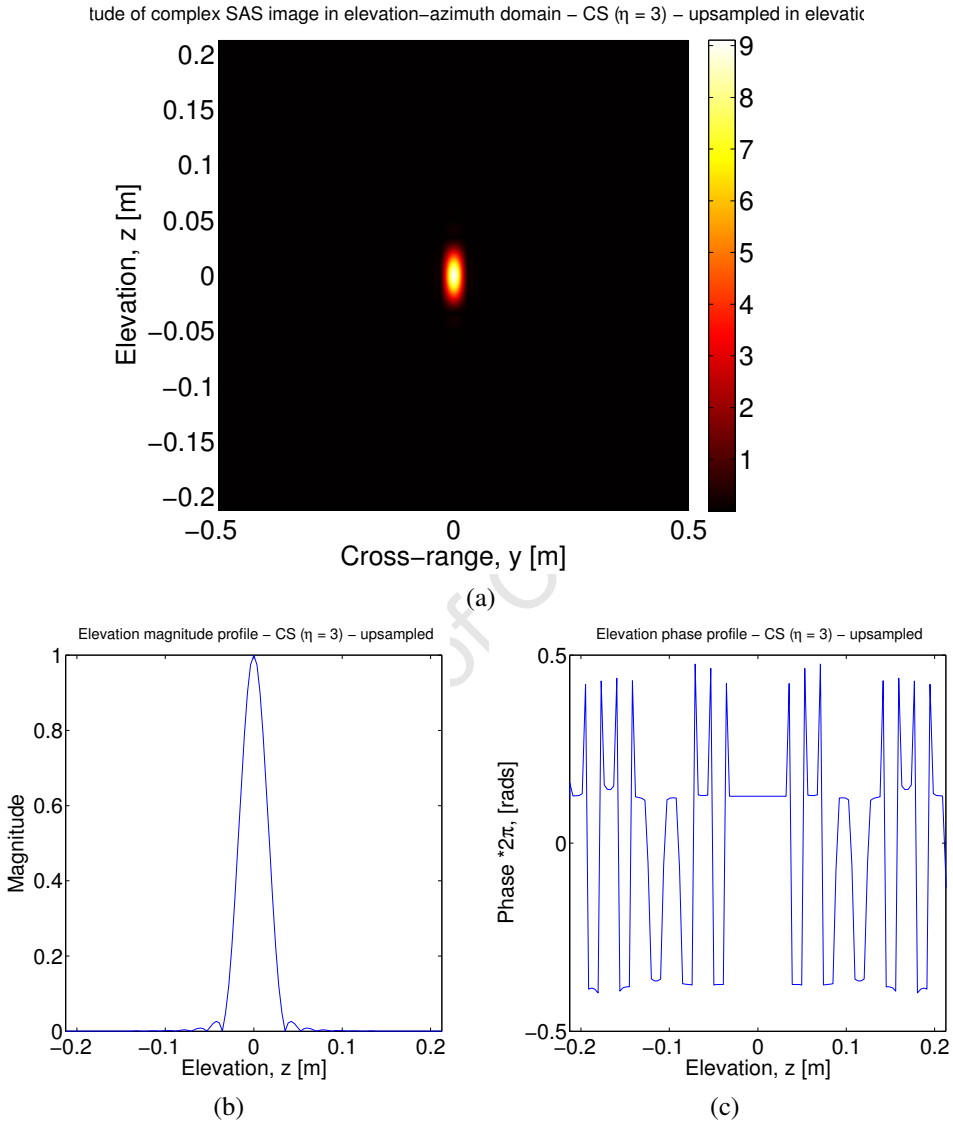

Figure 6.19: Reconstructed elevation image and profile of a scene containing a single point target at zero elevation using CS with $\eta = 3$. (a). Reconstructed elevation image. (b). The elevation magnitude profile (c). The elevation phase profile.

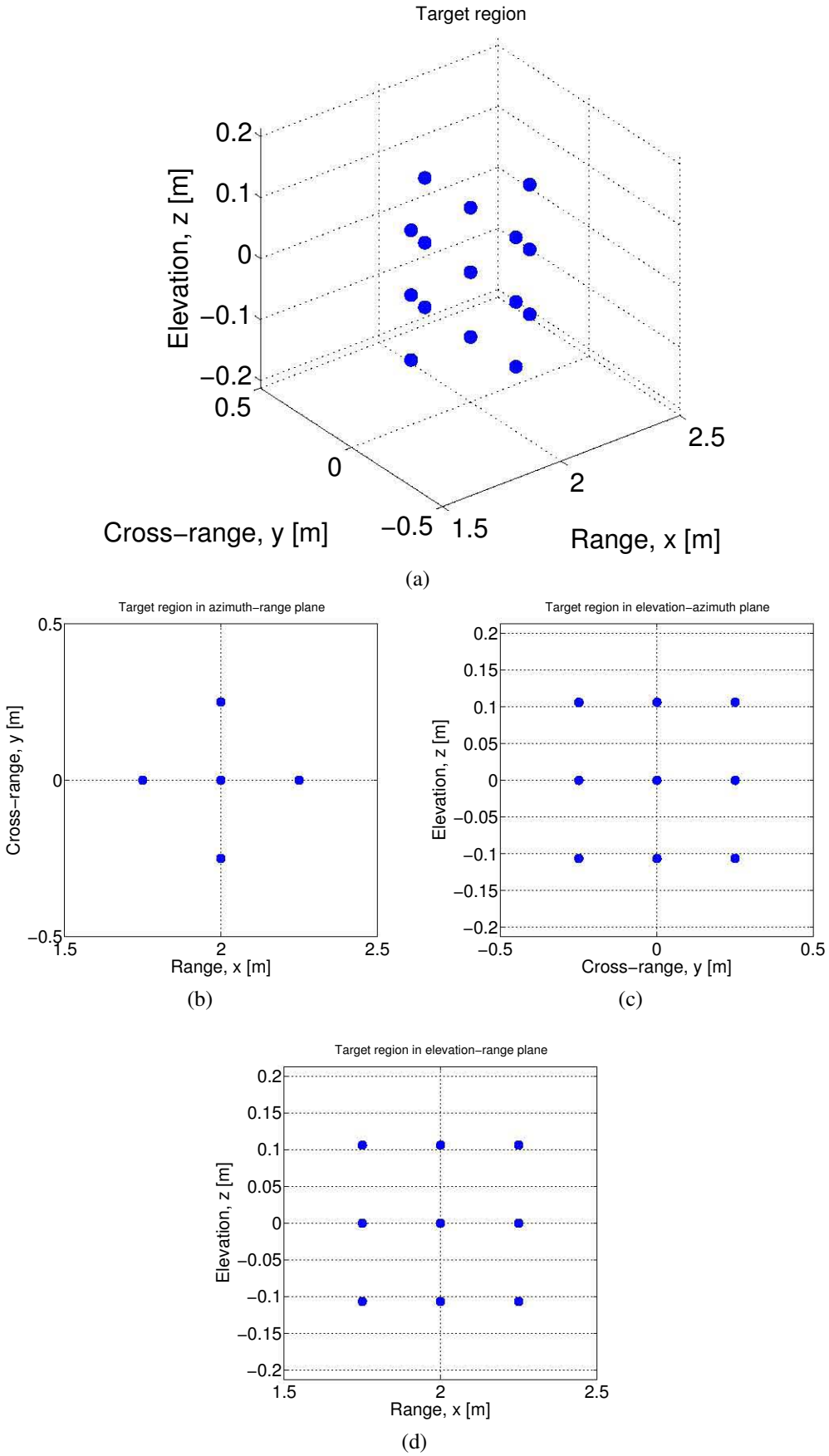

Figure 6.20: The simulated 3D target region with 15 point targets

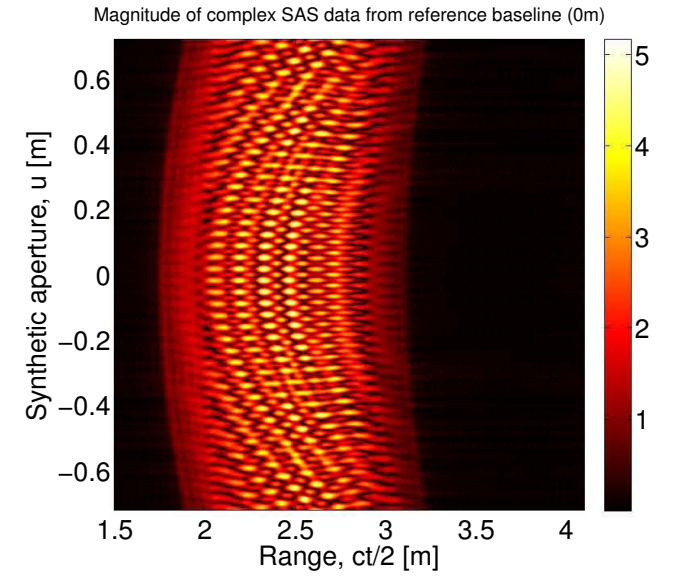

(a)

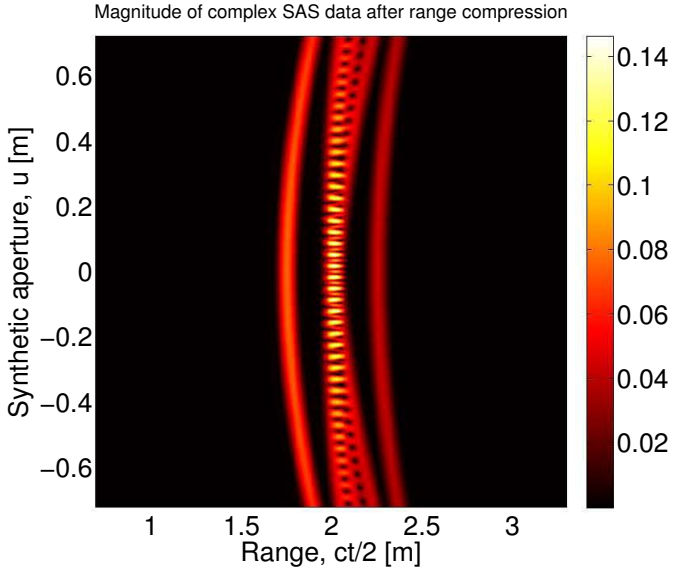

(b)

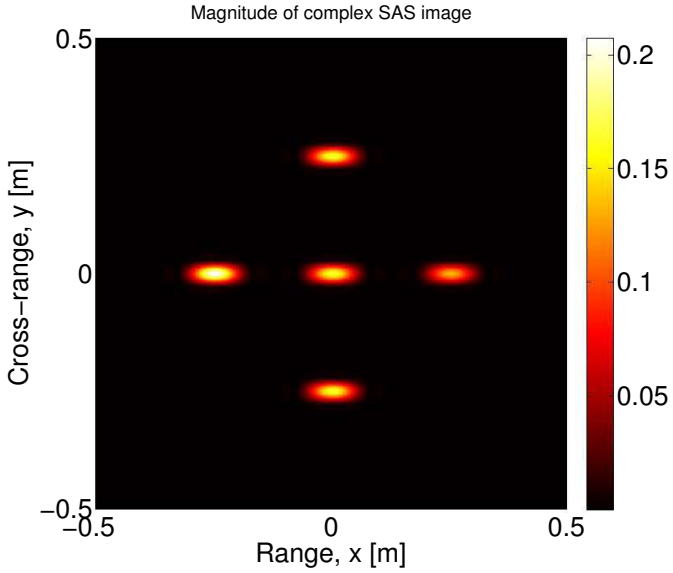

(c)

Figure 6.21: 2D SAS (a). raw data (b). range compressed data and (c). image from the reference orbit

the range and cross-range profile from the one of the outermost orbit with one target at $(X_c, 0, 0)$ before and after registration is shown in Fig. 6.22. Observe again that the cross-range profile remains unchanged after registration for the same reason given in the case of single target simulation.

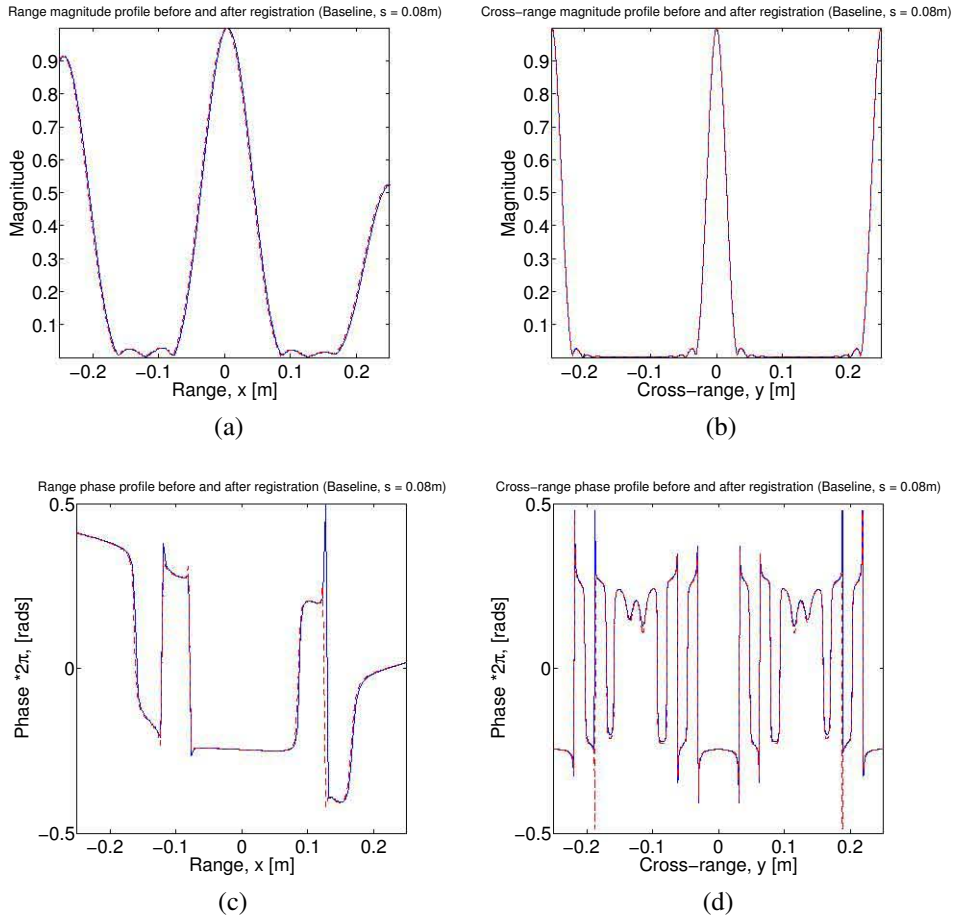

Figure 6.22: Profiles from the 9th orbit before (blue) and after (red-dashed) image registration (a). Range magnitude profile. (b). Cross-range magnitude profile. (c). Range phase profile. (d). Cross-range phase profile.

Deramping the Tomographic Elevation Signal

Fig. 6.23 shows the phase of the elevation signal before and after deramping. Here the residual video phase is not flat compared to the case of a single target because it is composed of the different phase contributions from all the targets.

Elevation Imaging via Inverse FFT

Fig. 6.24 shows the estimate of the elevation profile obtained by taking the inverse Fourier transform of the tomographic signal in the elevation direction. The three targets are barely resolvable in the image.

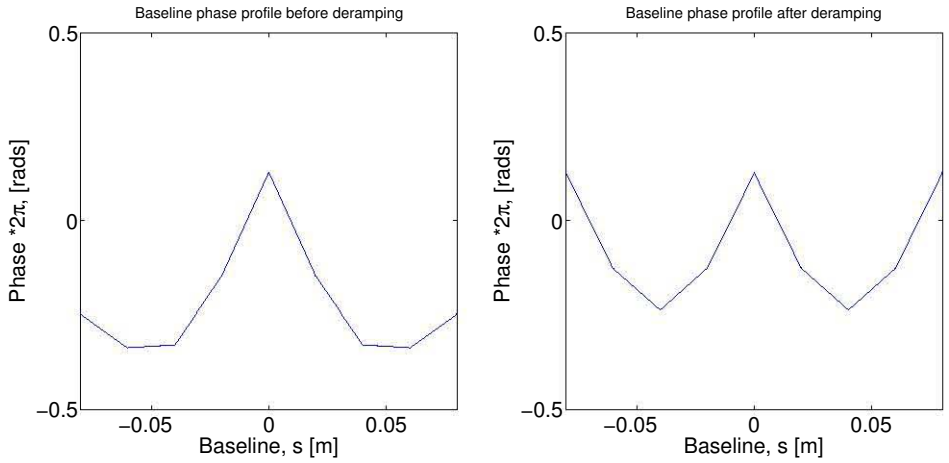

(a) (b)

Figure 6.23: Phase of the tomographic signal (a) before deramping (b) after deramping

Elevation Imaging using Compressive Sampling

l_1-norm minimization (3.16) was performed on each column of the registered-deramped-noiseless 3D SAS image to focus the image in the elevation direction using SPGL1. Fig. 6.25 shows the reconstructed super-resolution SAS elevation image using compressive sampling with $\eta = 3$. The targets are now easily resolvable in the elevation direction.

6.4 Effect of Baseline Span on Elevation Image

The effect of baseline span on the elevation image obtained from both the FFT and CS technique was investigated. The baseline span was changed by varying the number of transducers used in the array. It is expected that the FFT-based reconstructions will have poorer resolutions at smaller baselines because the nominal resolution is inversely proportional to the baseline span according to (3.9). This may not be a problem in CS reconstructions as it has been demonstrated that it is possible to achieve super-resolution, in fact because the CS model assumes that the baseline span is far less than the imaging range, it is expected that the CS reconstruction improves with smaller baselines. To confirm this, the target region in the previous section was used but 3, 5, 9, 11 and 15 transducers were successively used to obtain an elevation image of the scene, these correspond to a total baseline span of 0.04, 0.08, 0.16, 0.20 and 0.28m respectively. From the results (Fig. 6.26 and Fig. 6.27) one can deduce that the resolution of the image obtained via the IFFT method improves with an increase in baseline span as the three targets at the different elevations become resolvable as the number of baselines increase. The CS images have better resolution than IFFT images for all baseline spans because of the super-resolution factor of 3 which was used. However it only from baselines of 0.08m and upwards that CS accurately reconstructs the images. The CS reconstruction using 3 baselines is not accurate as the targets at elevations other than zero are not located in the image. Also artifacts in the form of sidelobes, smearing of the point spread function and tearing in

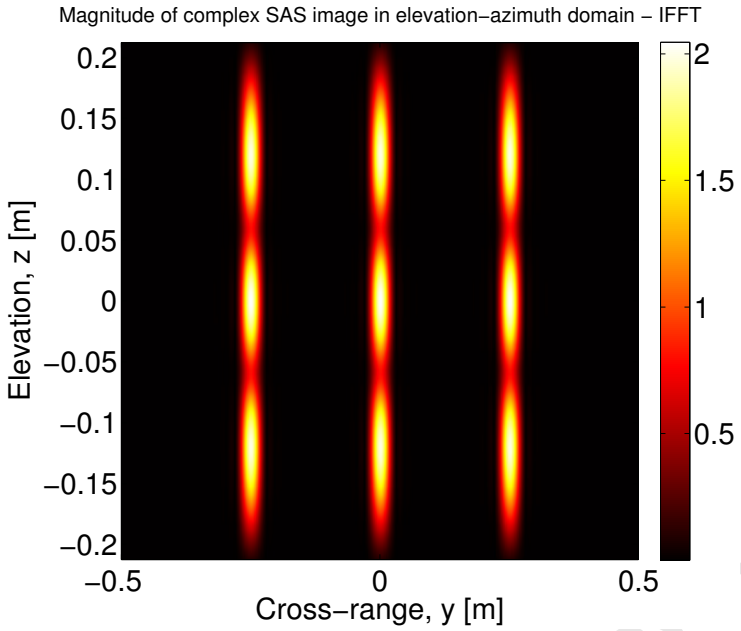

(a)

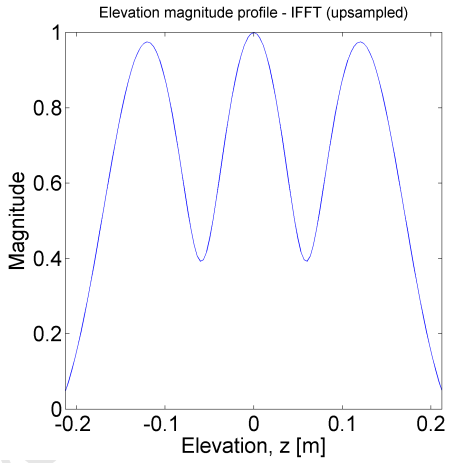

(b)

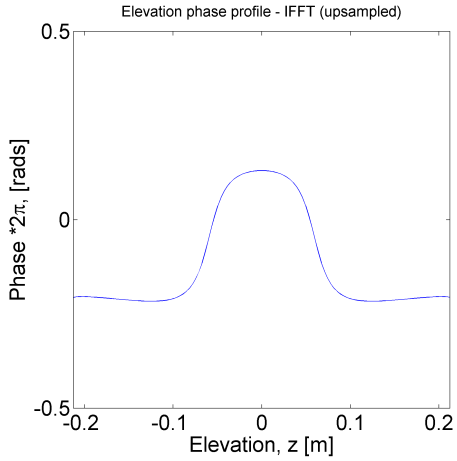

(c)

Figure 6.24: Reconstructed elevation image and profiles of scene containing 15 point targets in the elevation-azimuth domain using IFFT (a). The elevation image (b). The elevation magnitude profile (c). The elevation phase profile

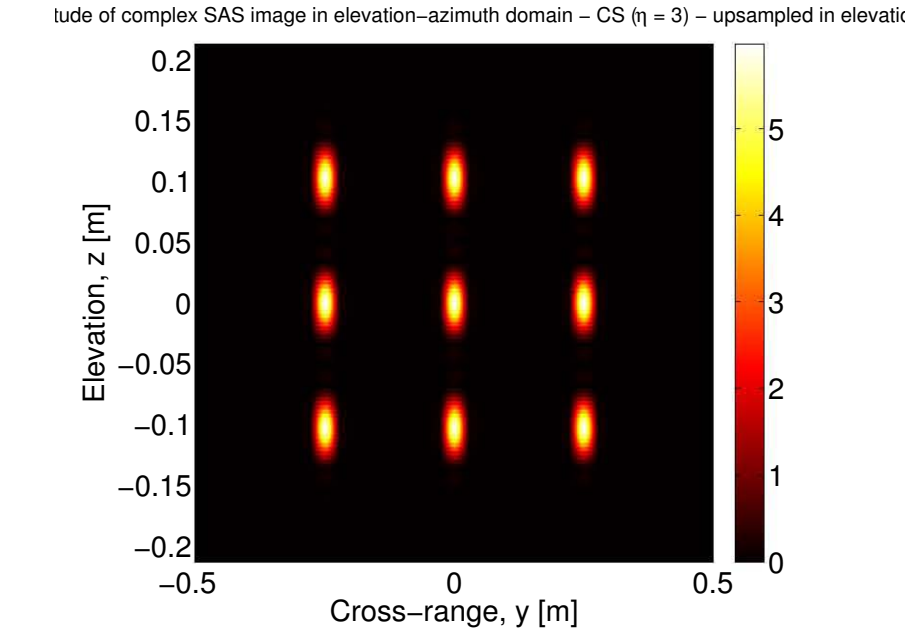

(a)

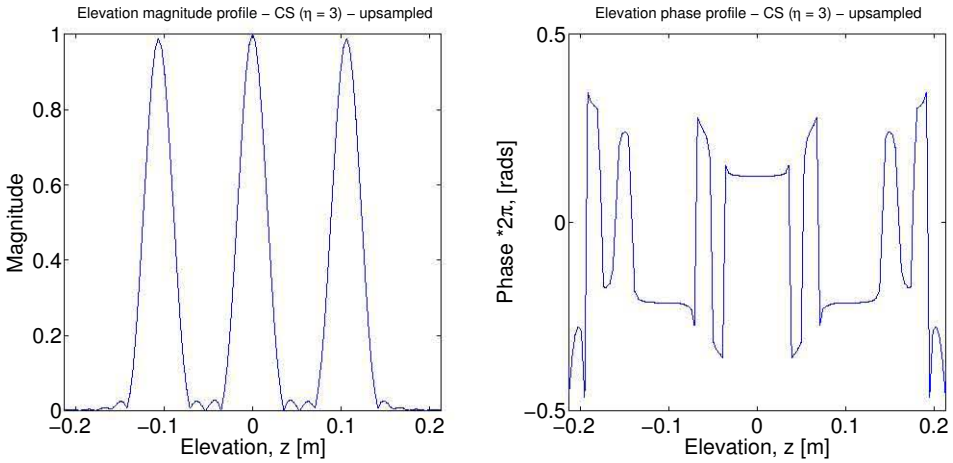

(b)

(c)

Figure 6.25: Reconstructed elevation image and profile of a scene containing a 15 point targets using CS with $\eta = 3$ (a). Reconstructed elevation image. (b). The elevation magnitude profile (c). The elevation phase profile.

the pixels of the image increases in the CS images as the baseline span increases. Note skew in the point spread function of targets which are not at zero elevation which becomes more prominent with longer baselines. This might be attributed to the fact that CS reconstructs sprectral lines [10] and those spectral lines shift with range at higher elevations. However for long baselines, the shifts decrease with an increase in range (Fig. 6.27e) to yield a more uniform point spread function. This explains the fact that for tomographic reconstruction to be treated as a spectral analysis problem, the baselines must be small compared to the range of imaging and not too high range resolutions [27, 10, 26].

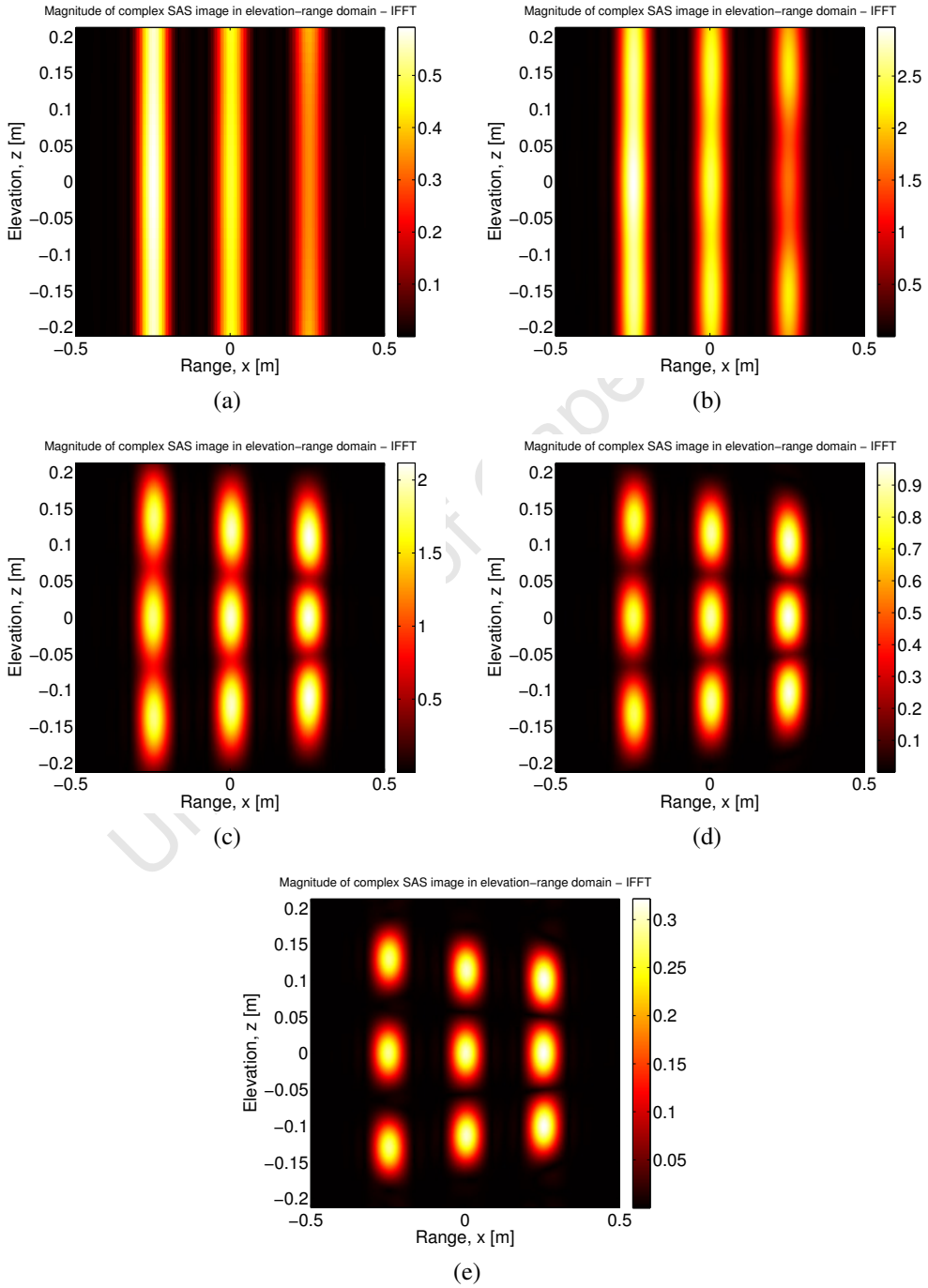

Figure 6.26: SAS images in the elevation-range domain obtained via IFFT with different number of baselines. (a). 3 baselines (b). 5 baselines. (c). 9 baselines. (d). 11 baselines. (e). 15 baselines

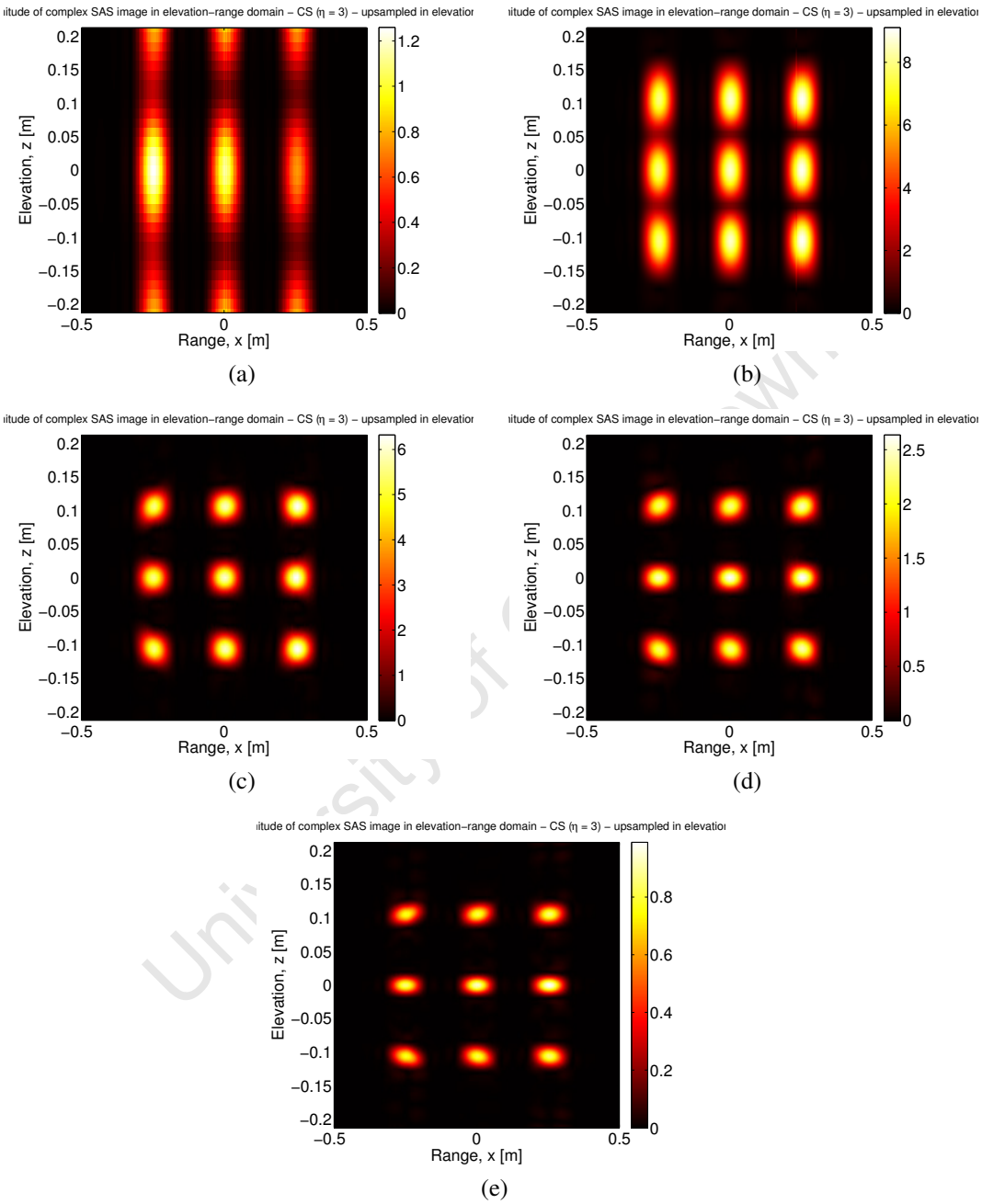

Figure 6.27: SAS images in the elevation-range domain obtained via CS with different number of baselines. (a). 3 baselines. (b). 5 baselines. (c). 9 baselines. (d). 11 baselines. (e). 15 baselines

6.5 Effect of Super-resolution Factor

The effect of the super-resolution factor on the CS images was investigated. The upper limit on the super-resolution factor is given by (5.2):

$$\eta_{up} \leq \frac{\lambda X_c}{8 L_s \cdot Z_0} \exp\left[\left(\frac{M_z}{C \cdot S}\right)^{1/4}\right]$$

where λ is the wavelength, X_c is the range to the centre of the scene, L_s is the baseline half-span, Z_0 is half of the elevation extent, M_z is the number of acquisitions which was chosen to be 9, S is the estimated number of target contributions in a range-azimuth cell which was 3 in this case, and C is a small constant which in this case was empirically estimated to be = 0.714.

With all the parameters in the equation known, the upper limit on the super-resolution factor was calculated to be 3. The super-resolution factors of 1, 3, 4, 6 and 12 were used successively to evaluate its effect on the CS images. The reconstructed images and elevation profiles are shown in Fig. 6.28. From the images one can observe that the super-resolution factor does indeed affect the resolution of the CS images as expected. However the artifacts increase with super-resolution and thereby degrade the images. This confirms that if the number of measurements is not sufficiently high for the required elevation resolution, artifacts appears in the reconstruction [44].

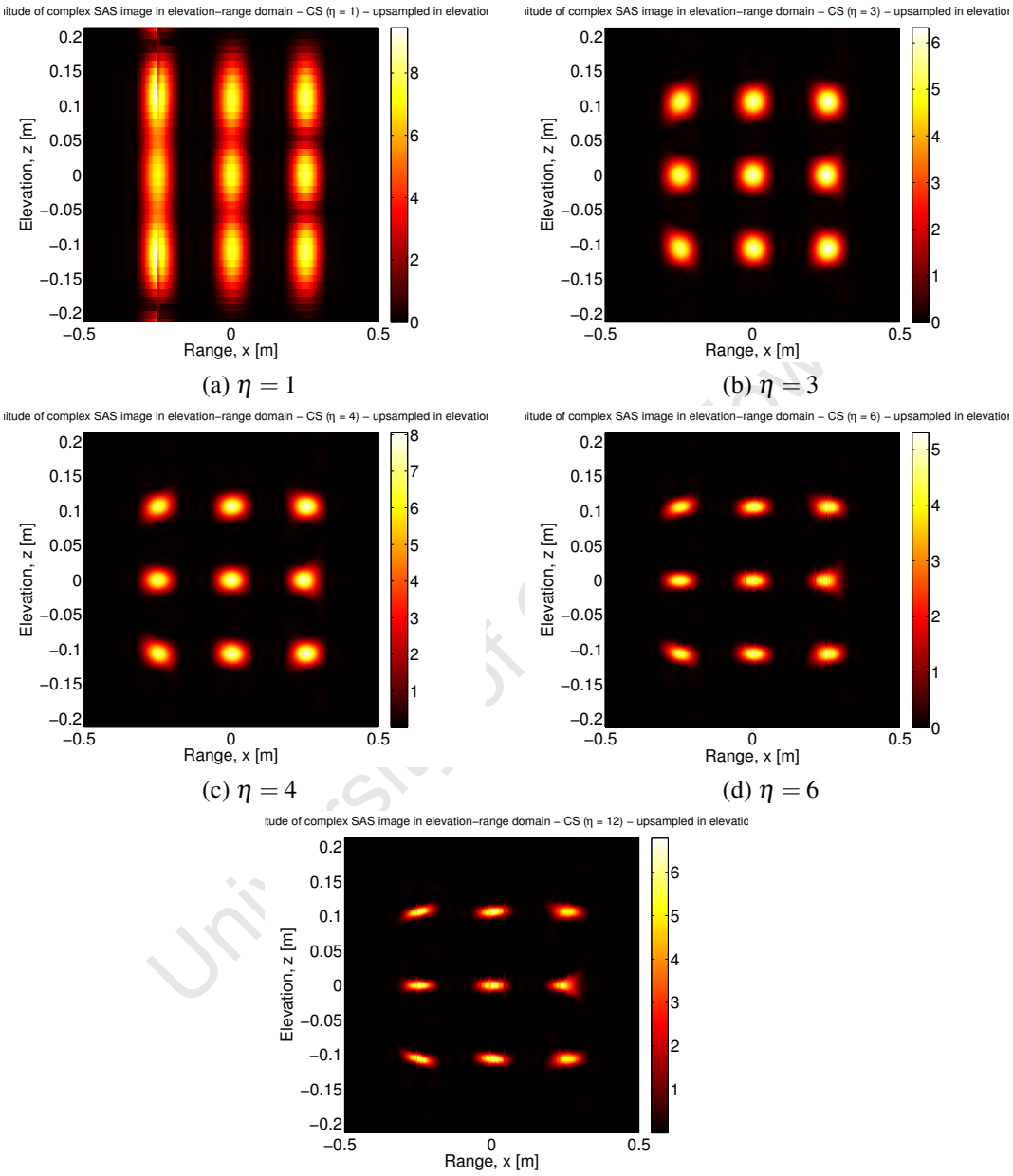

(a) $\eta = 1$

(b) $\eta = 3$

(c) $\eta = 4$

(d) $\eta = 6$

(e) $\eta = 12$

Figure 6.28: Effect of super-resolution factor on CS images in the elevation-range domain

Chapter 7

Three-dimensional SAS Processor Results and Discussion

In this chapter the results of the 3D SAS processor applied to the real ultrasound array measurements are presented. These results are discussed and compared with those obtained from simulation in the previous chapter in order to draw reasonable conclusions on the capability of the system in obtaining 3D SAS images.

7.1 The Transmitted (Loopback) Pulse

Fig. 7.1a shows the transmitted chirp pulse as recorded by the loopback channel at a particular point along the synthetic aperture with a pulse width of 5ms. There is a gradual drop in the amplitude of the pulse as a result of the roll-off of the filters used in the system. This effect was compensated during post-processing by inverse filtering. Fig. 7.1b shows the magnitude spectrum of the transmitted pulse that contains aliasing as a result of the sampling rate (60kHz) which violates the Nyquist sampling criterion for low pass signals. It was however concluded that the second envelope in the magnitude spectrum is always centred at the required frequency of 40kHz, while the first envelope is the aliased spectrum. The bandwidth of the signal was about 4kHz which yielded a time-bandwidth product of 20. Fig. 7.2a shows the basebanded version of the transmitted signal where it has been stripped of its out-of-band frequency components (the carrier 40 kHz) and it now centred on 0Hz as shown by its magnitude spectrum in Fig 7.2b. The basebanding was performed by IQ demodulation process as described in Chapter 2. The spectrum of the baseband signal is not aliased since the sampling rate satisfied the Nyquist sampling criterion for bandpass signals which states that the sampling rate must be a least twice the bandwidth of the bandpass signal. The transmitted pulses along the synthetic aperture were similar to the one shown here.

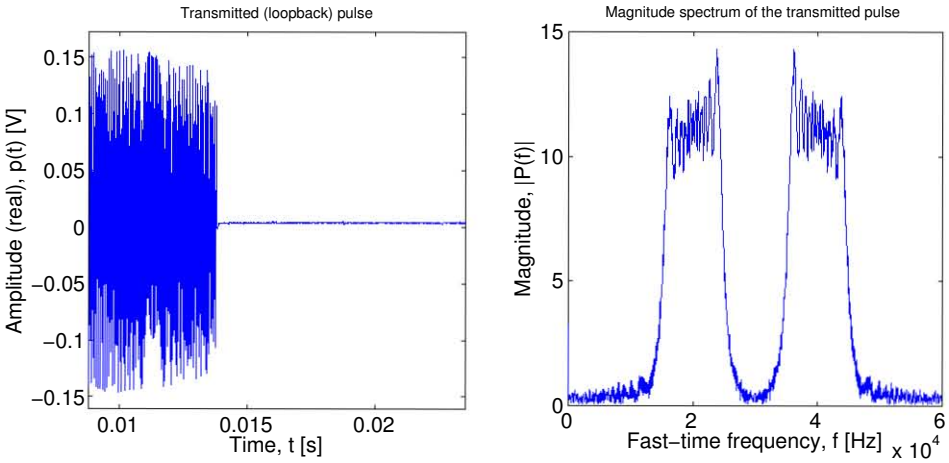

(a) Time-domain (b) Aliased magnitude spectrum

Figure 7.1: The transmitted (loopback) signal

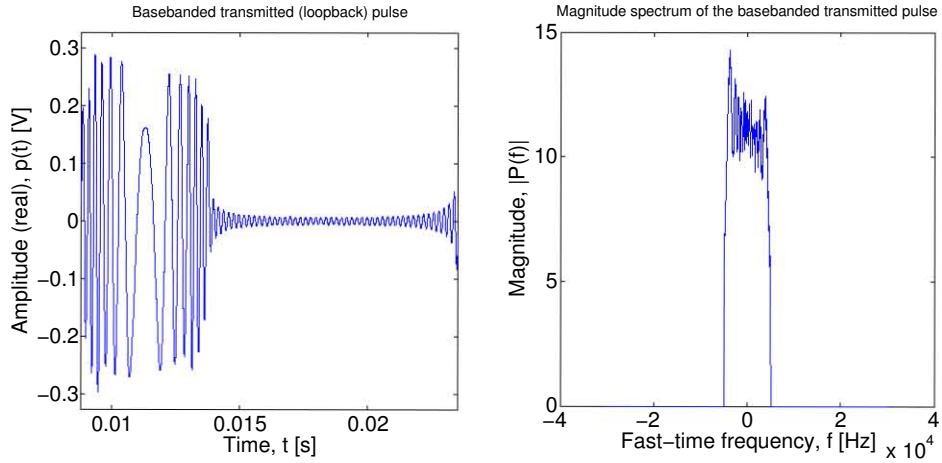

(a) Time-domain (b) Magnitude spectrum

Figure 7.2: The basebanded loopback signal

7.2 3D SAS Imaging: A Single Point Target

To demonstrate the 3D resolution capabilities of a system, a corner reflector was placed at the centre of the scene $[X_c, Y_c, Z_c]$ where $X_c = 2$m, $Y_c = 0$m and $Z_c = 0$m. The corner reflector was made by joining three 5-by-5cm fibre glass plates to form an open cube with one vertex (Fig. 7.3). Fig. 7.4 show photographs of the scene taken from different viewing angles.

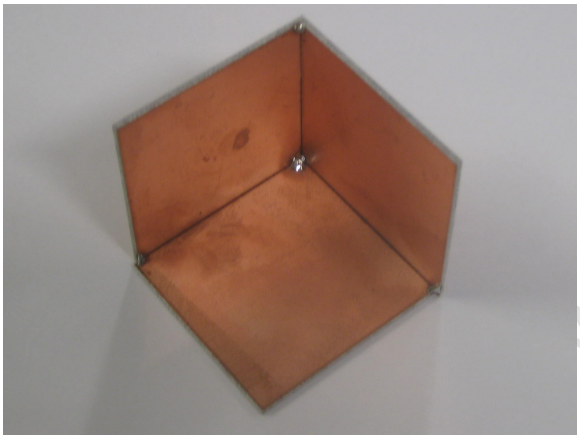

Figure 7.3: Photograph of the corner reflector used in the test scene

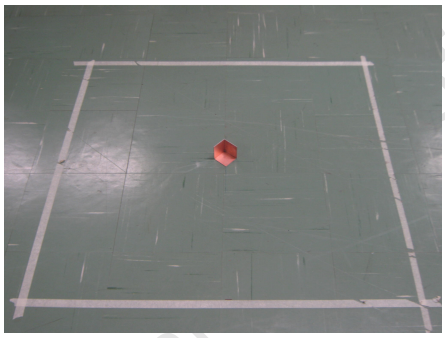

(a) Point of view from the centre of the synthetic aperture

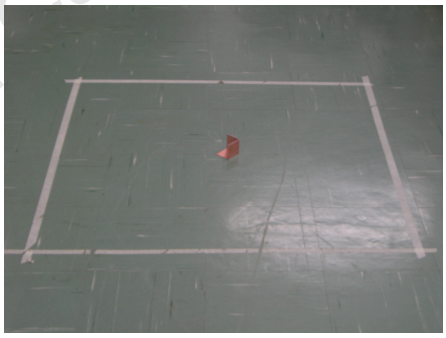

(b) Point of view from the mid-range

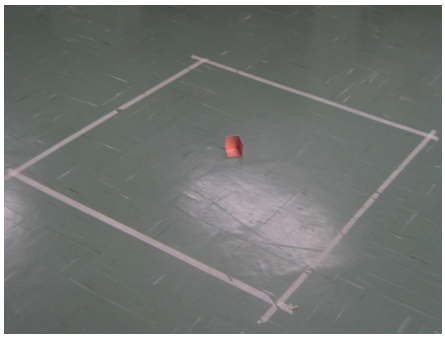

(c) Point of view of the operator

Figure 7.4: Photographs of the target scene from different perspectives

7.2.1 2D SAS Data and Range Compression

Fig. 7.5a is an image of the response from the point target as recorded from the reference baseline. The image is the real part of the echoed chirp signal that is received by the transducer as it moved along the synthetic aperture (the vertical axis). Fig 7.5b shows the response from the target after pulse compression. One can observe the hyperbolic locus of the response that describes the variation in range to the target as a function of the position of the sensor along the synthetic aperture.

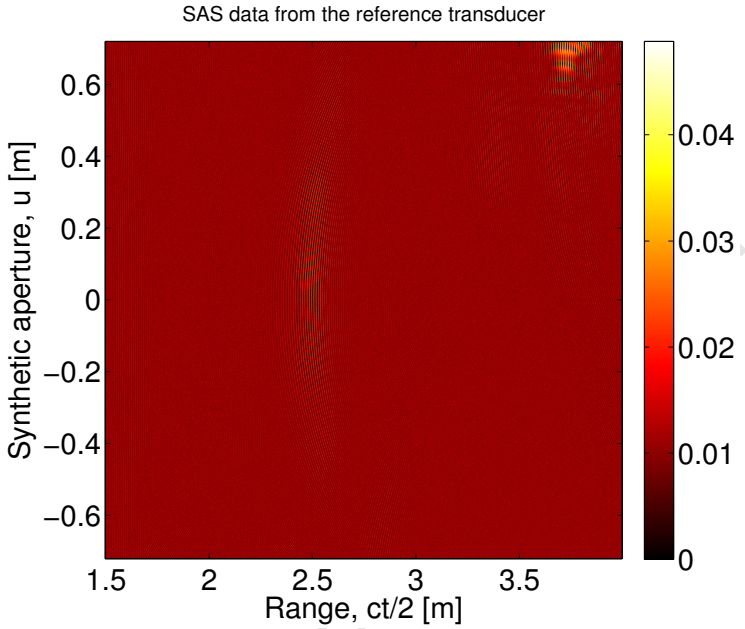

(a)

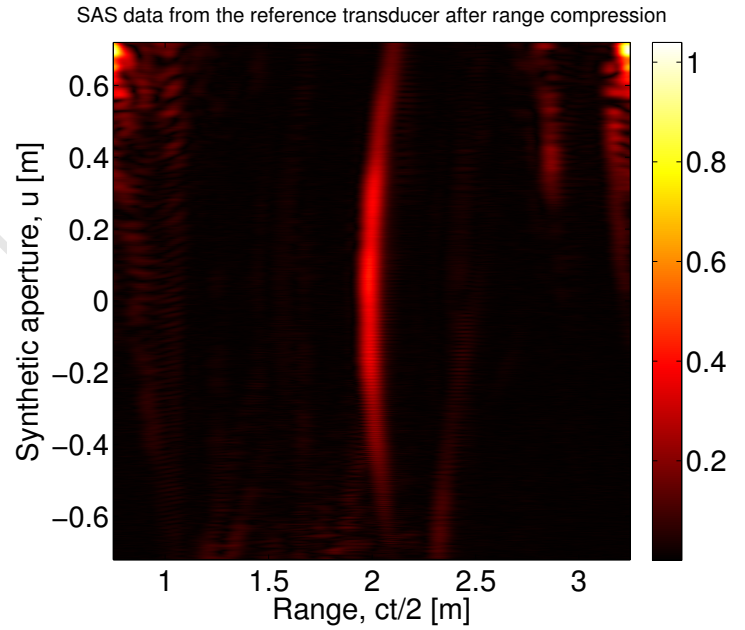

(b)

Figure 7.5: SAS data from a corner reflector (a). The response from the corner reflector. (b). Pulse-compressed response from a single target

Pulse compression was achieved using an inverse filter designed to deconvolve the system effects and as a prewhitening filter for matched filtering as described in Section 4.2. The

matched filter was designed from a time-shifted version of the loopback signal. A Hann window was used to suppress the sidelobes of the output response. The bright returns in the SAS data (Fig. 7.5) at the range of about 3.7m and azimuth of 0.7m are returns from a file cabinet that was sitting at that position in the laboratory where this experiment was conducted. After range compression the signature of the cabinet wraps around causing bright spots in the range compressed image at range 1.7m and 3.3m. The object was however not in the imaging range and was therefore time-gated out in the final SAS image (Fig. 7.6). Notice the presence of weak SAS signatures at range of 2.3m and -0.4m azimuth, these are signatures from targets outside the target region but visible to the transducers as a result of the wide beamwidth of the transducers.

7.2.2 2D SAS Image Reconstruction: Accelerated Chirp Scaling Algorithm

Fig. 7.6a shows the final 2D SAS image obtained using the accelerated chirp scaling algorithm. The image represents the magnitude of the complex SAS focused data. The point spread function is a two-dimensional sinc function in the range and cross-range directions with a range resolution of 6.52 cm and a cross-range resolution of 2.2cm measured as width of the mainlobe of the sinc functions at the 3-dB point. The cross-range Doppler bandwidth used in the reconstruction was 200 rads/m as was established in the simulations. Fig. 7.6b & 7.6c shows the range and cross-range profiles from the reference transducer along the centre of the scene. The magnitude response of both profiles has a mainlobe as expected which peaks at the range and cross-range position of the target from the sensor which were approximately -1.5cm and -0.15cm respectively. There is also a smearing of the response to the right of the mainlobe in the range profile which could be associated to multipath echo from the side of the table on which the platform was mounted. Note the fairly flat phase response of point spread function in the range and cross-range directions. It is not as flat as the simulated response in the Chapter 6 as a result of possible phase errors introduced in the data acquisition and processing. Fig. 7.7 shows the SAS images obtained from the different baselines used in the acquisition. The image all look quite similar. Differences in the images will arise as a result of different viewing angles of each baseline.

7.2.3 Image Coregistration

The stack of 2D SAS images from all the baselines used were coregistered with respect to the reference baseline with a subpixel accuracy of 1/10. Fig. 7.8 shows the range and cross-range profiles from all the baselines after coregistration. There is not much variation in the profiles, confirming that the registration algorithm works.

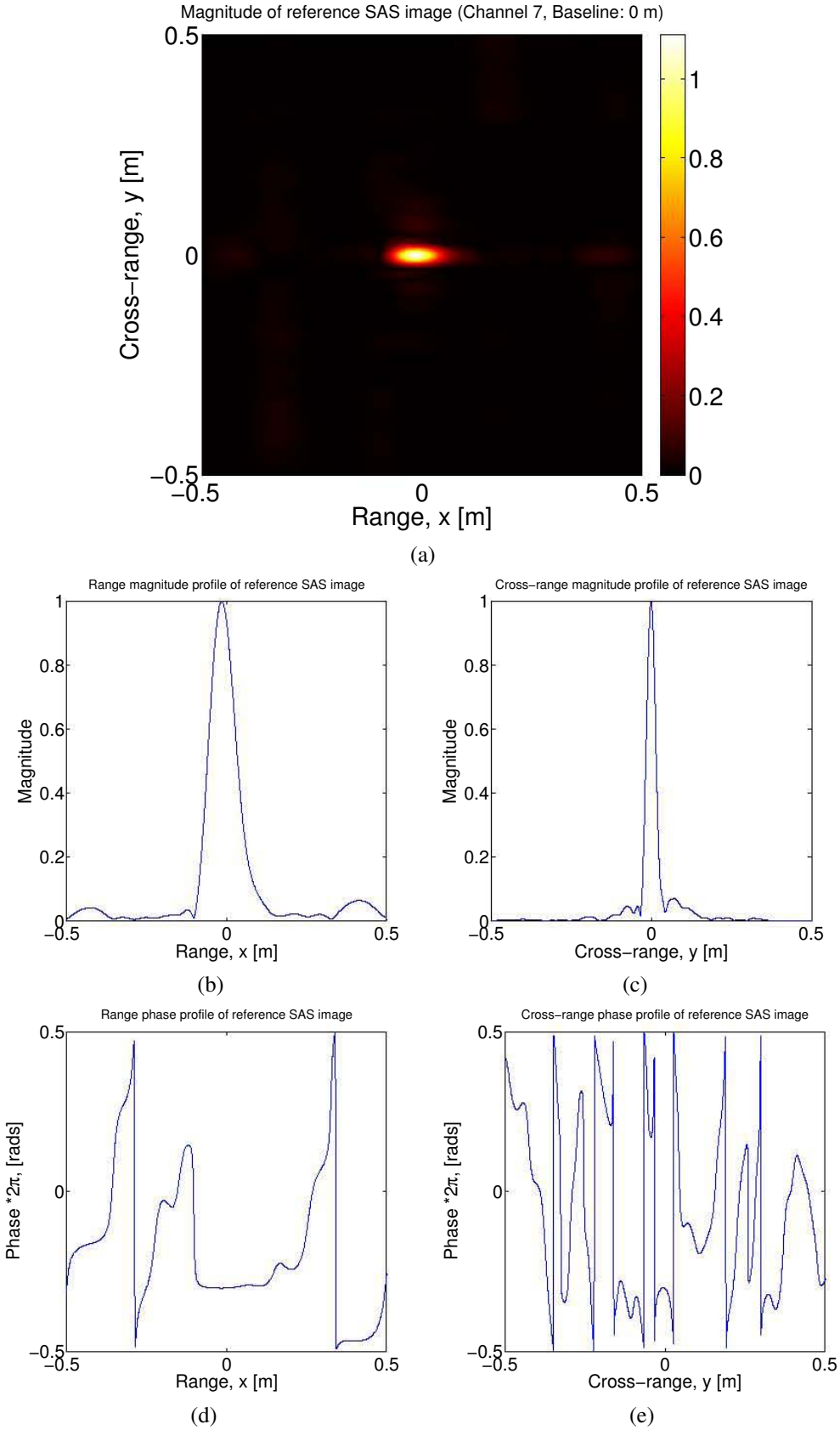

Figure 7.6: 2D SAS image and profiles of a corner reflector placed at the centre of the scene. (a). 2D SAS image of a corner reflector (b). Range profile (c). Cross-range profile

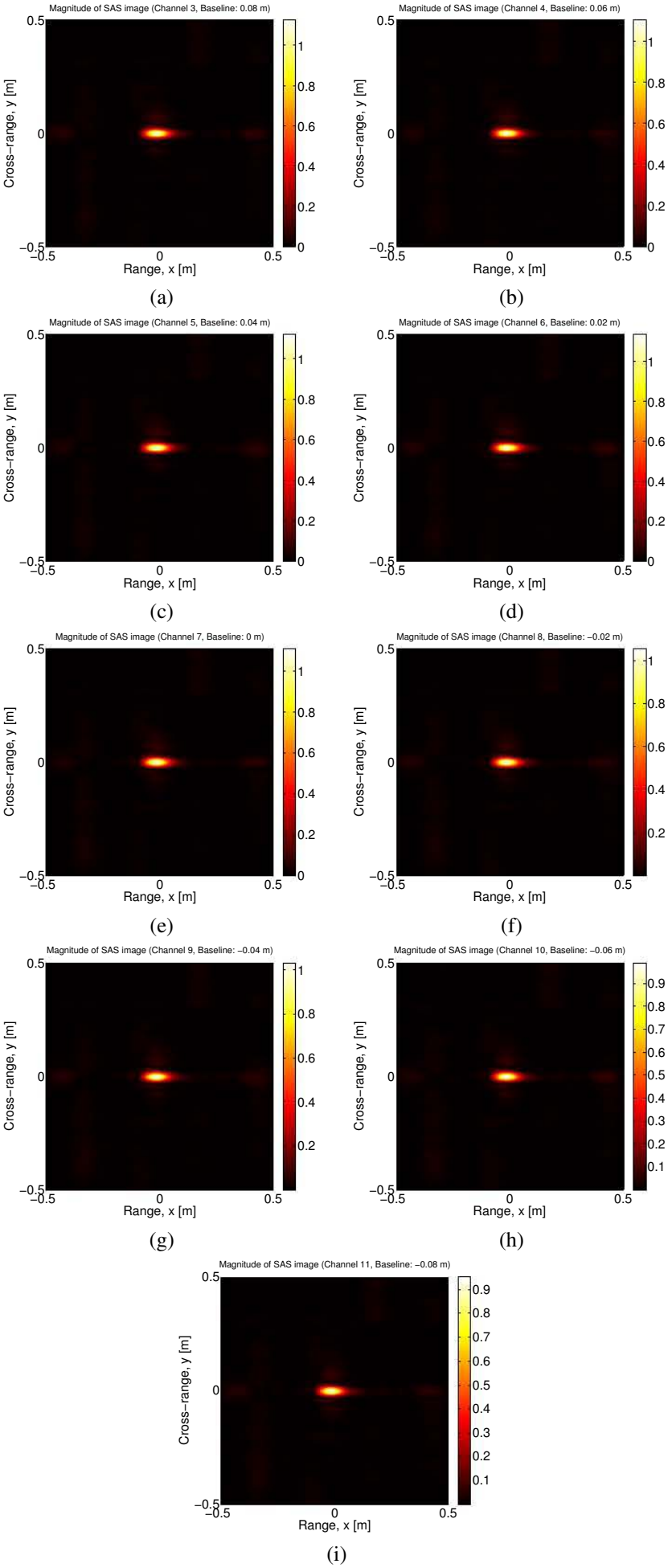

Figure 7.7: 2D SAS images of the corner reflector from 9 uniformly spaced baselines

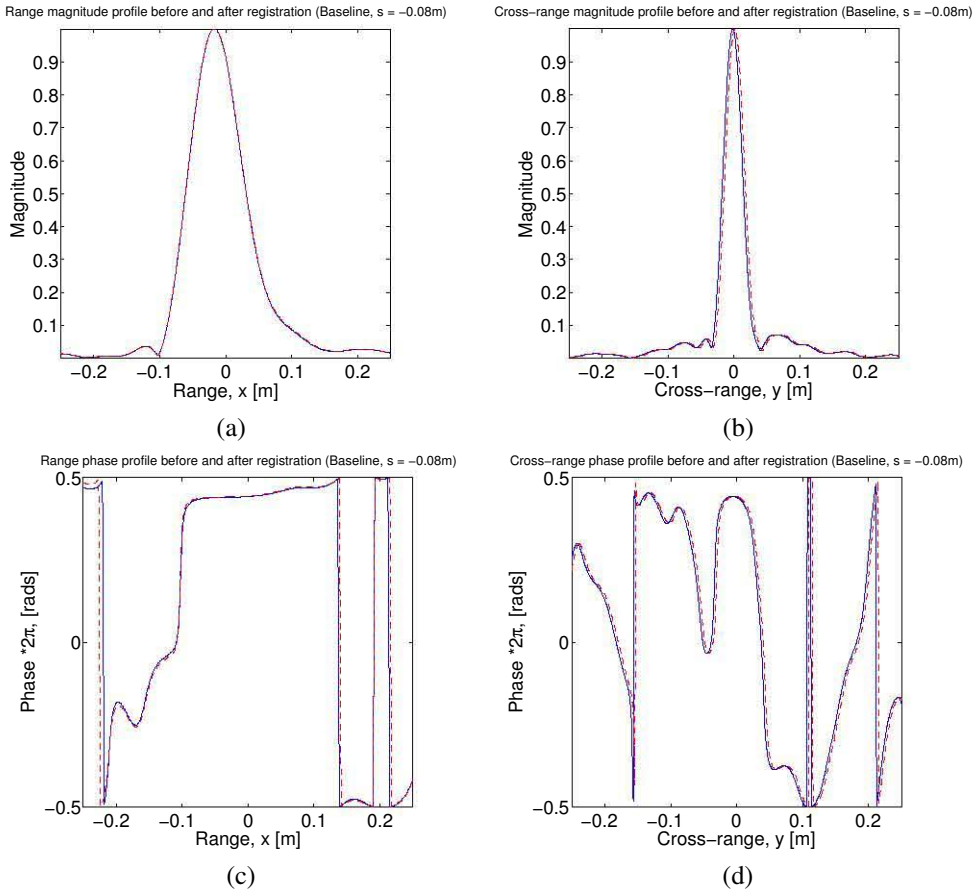

Figure 7.8: Range and cross-range profiles of corner reflector before and after co-registration (blue - before; red - after). (a). Range magnitude profile. (b). Cross-range magnitude profile. (c). Range phase profile. (d). Cross-range phase profile.

7.2.4 Deramping

Fig. 7.9 shows the phase of the elevation signal the location of the point target before and after deramping. The phase of the signal is quadratic before deramping as expected from theory and simulations. The displayed phase is wrapped in to the interval $[-\pi, \pi]$ and the phase jumps at the extremes are due to wrapping. The deramping operation should eliminate the quadratic phase term associated with the baseline. There is however still a residual quadratic phase which is more than the expected residual phase. This could be caused by phase noise in the system and also the possibility that the transducers do not have a flat phase response. The regularization parameter, ε in the CS algorithm can be used to compensate for this error.

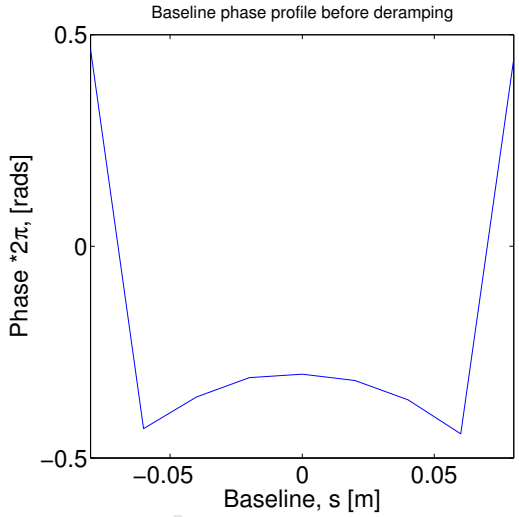

(a)

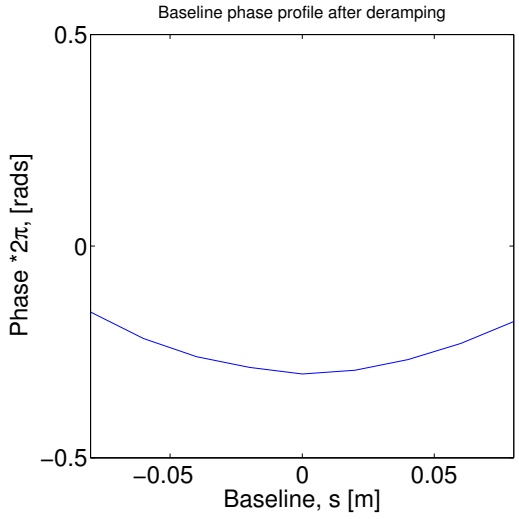

(b)

Figure 7.9: Baseline phase profile (a). before and (b). after deramping

7.2.5 3D SAS Image: FFT method

Fig. 7.10 shows the reconstructed SAS elevation image and profiles in the elevation-azimuth domain using the FFT method. The image is the magnitude of the focused SAS

data in the domain. The SAS image was obtained by taking the inverse Fourier transform of the deramped 3D SAS data. To improve the visibility of the image, the image is upsampled in the frequency domain (Fig. 7.11). The measured elevation resolution was 7.73 cm which is about 45.6% larger than the nominal resolution (5.31cm) that can be achieved with this geometry.

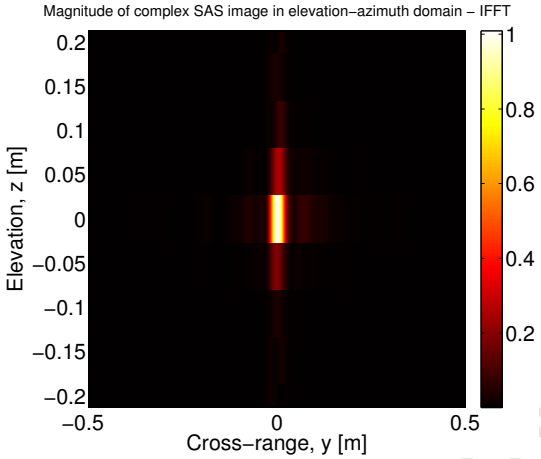

(a) SAS elevation image at elevation-azimuth section ($x = -0.015$m)

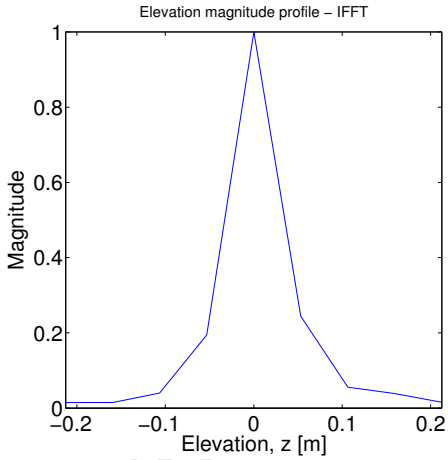

(b) Elevation magnitude profile at $x = -0.015$m and $y = -0.0015$m

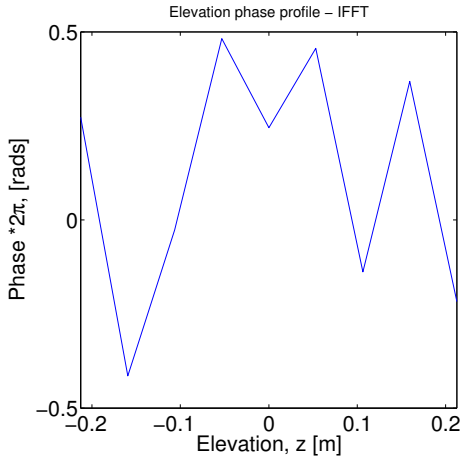

(c) Elevation magnitude profile at $x = -0.015$m and $y = -0.0015$m

Figure 7.10: Poor visibility elevation image of a corner reflector in the elevation-azimuth domain ($x = -0.015$m) using IFFT

7.2.6 3D SAS Image: CS method

l_1-norm minimization (3.16) was performed on each column of the registered-deramped 3D SAS image to focus the image in the elevation direction using SPGL1. The super-resolution capability of the compressive sampling technique was explored by using a super-resolution factor of $\eta = 3$, which corresponds to an elevation resolution of $\delta z_{\text{sup}} = \triangle_z/\eta = 0.81$cm. Fig. 7.12 shows the reconstructed super-resolution SAS elevation image. Here CS successfully detected a single spectral line at the location of the corner reflector. Again the visibility of the reconstruction is improved by upsampling (Fig.7.13). The

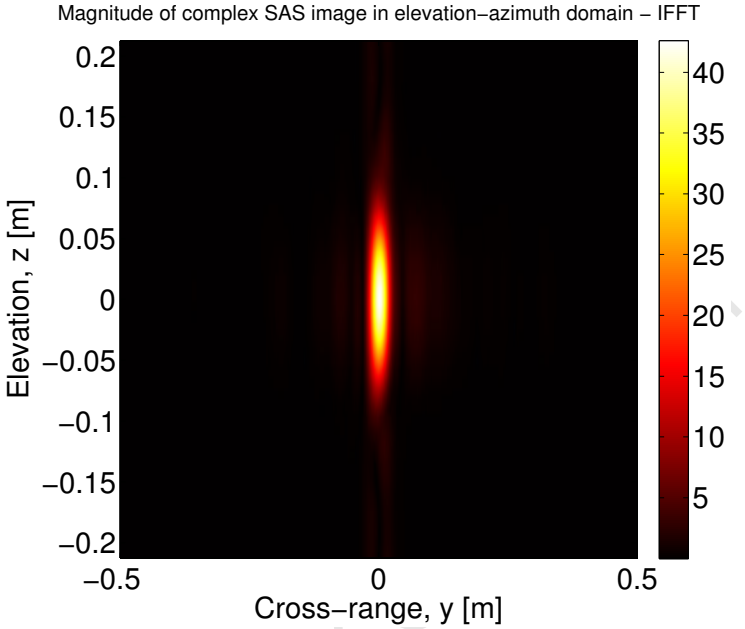

(a) SAS elevation image at elevation-azimuth section ($x = -0.015$m)

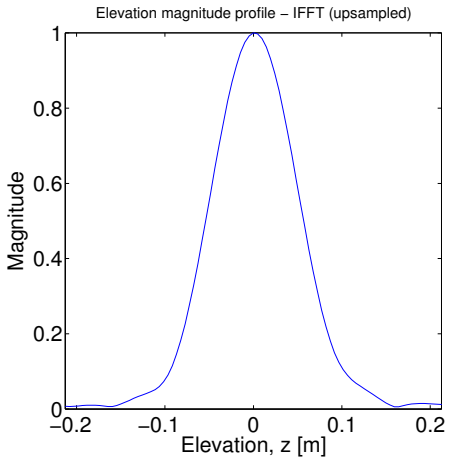

(b) Elevation magnitude profile at $x = -0.015$m and $y = -0.0015$m

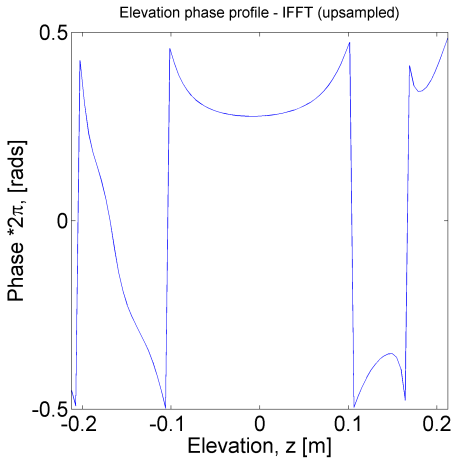

(c) Elevation magnitude profile at $x = -0.015$m and $y = -0.0015$m

Figure 7.11: Reconstructed elevation image and profiles of the corner reflector in the elevation-azimuth domain ($x = -0.015$m) using IFFT

measured 3-dB width of the point spread function in the elevation direction was 2.13cm which corresponds to a 3.6x improvement in resolution compared to the nominal IFFT reconstruction.

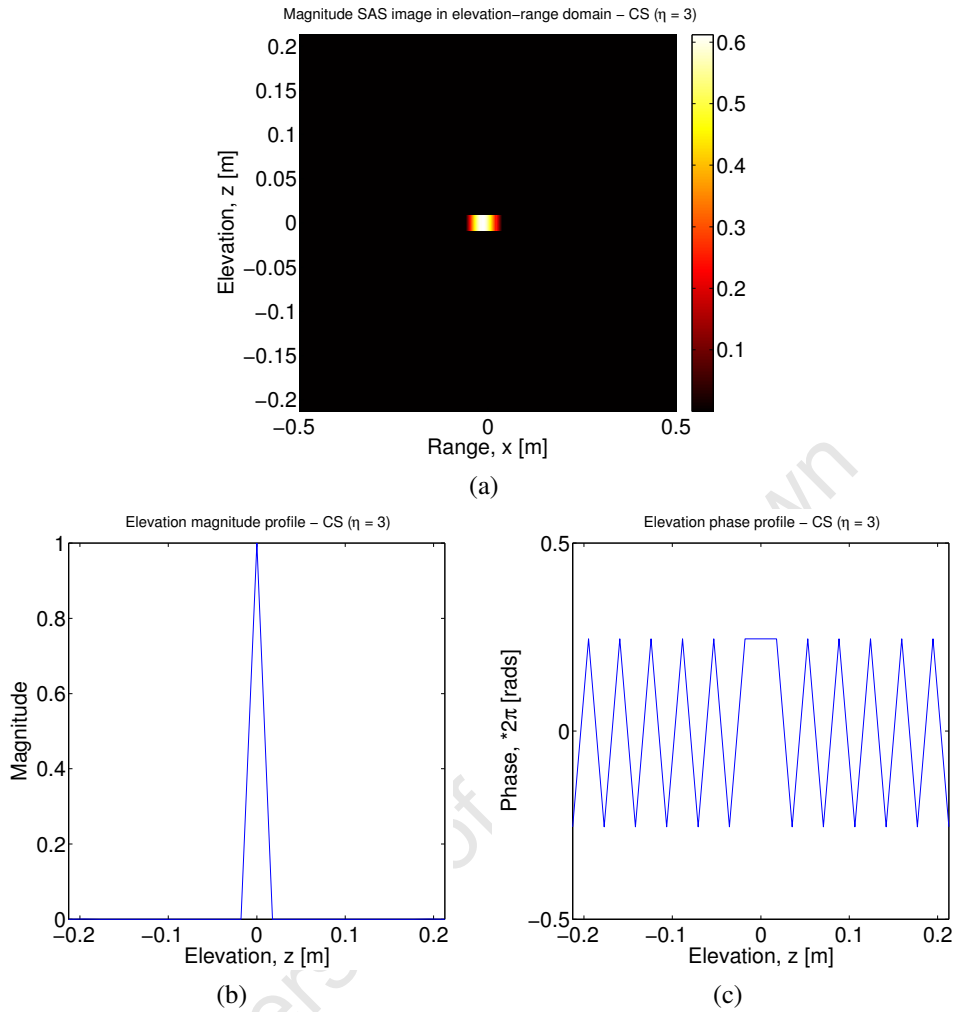

Figure 7.12: Poor visibility elevation image of a corner reflector in the elevation-azimuth domain ($x = -0.015$m) using CS with $\eta = 3$ and $\varepsilon = 1.5$ (a). Reconstructed elevation image. (b). The elevation magnitude profile (c). The elevation phase profile.

7.3 3D SAS Imaging: 2 Point Targets

In this experiment, two point targets (corner reflectors) were placed at the same range and azimuth coordinates of 2.0m and 0 m respectively, but at different elevations. The aim of this experiment was to demonstrate the capability of CS in distinguishing multiple targets placed at different elevations but whose 2D point spread function fall on the same range-azimuth pixel in the 2D SAS image. Fig. 7.14 shows photographs of different views of the scene. Fig. 7.15 shows the 2D SAS image obtained from the reference baseline (0.0m) as well as the range and cross-range profiles through the location of the target. Fig. 7.16 shows the reconstructed elevation image of an azimuth-elevation section of the scene taken at the range of the point targets using the Fourier technique. Once again

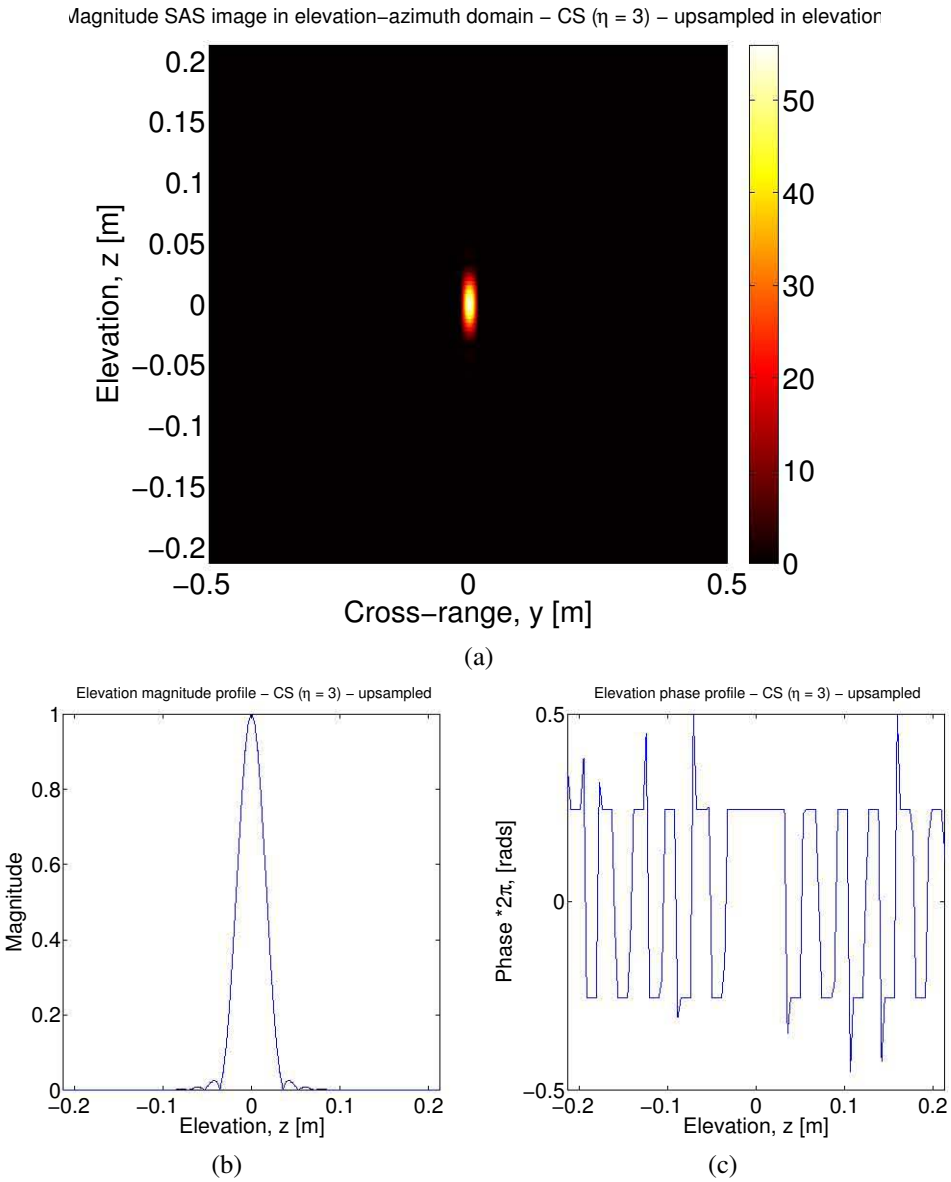

Figure 7.13: Reconstructed elevation image and profiles of the corner reflector in the elevation-azimuth domain ($x = -0.015$m) using CS with $\eta = 3$ and $\varepsilon = 1.5$ (a). Reconstructed elevation image. (b). The elevation magnitude profile (c). The elevation phase profile.

the reconstructed image exhibits low resolution as a result of the baseline extent used in the processing. Fig. 7.17 shows the same image reconstructed using the CS technique with a super-resolution factor $\eta = 3$ and $\varepsilon = 2.1$. With an improved resolution, the two point targets can be separated in the image. However from the elevation profiles shown in Fig. 7.17 one can notice the presence of a possible false target at an elevation of 0.1m. This could be attributed to the choice of the super-resolution factor and the regularization parameter as these have been shown to produce artifacts and ambiguities if not chosen appropriately [44].

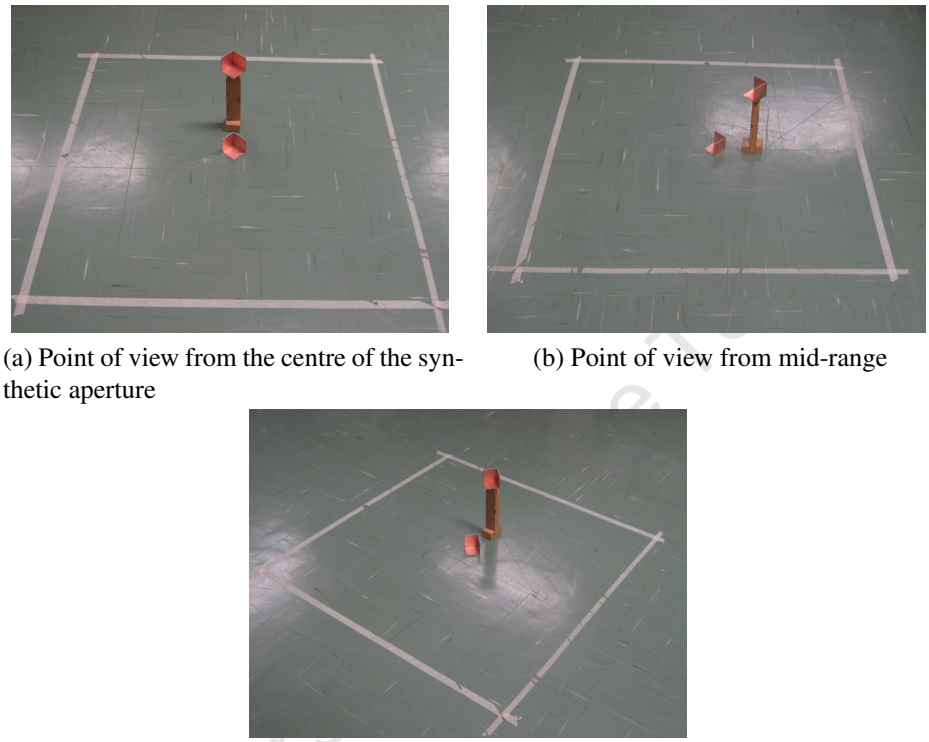

(a) Point of view from the centre of the synthetic aperture

(b) Point of view from mid-range

(c) Point of view of the operator

Figure 7.14: Photographs of the target scene from different points of view. The scene contains two corner reflectors at the same range and azimuth location but different elevations.

7.4 3D SAS Imaging: 5 Point Targets

Fig. 7.18 shows a photograph scene looking from the centre of the synthetic aperture. Point targets A, C and D are at approximately the same range (2 m) and elevation (0 m) but different azimuth positions (0.3 m, 0.0m, and 0.25m respectively). Targets B and C have the same range (2m) and azimuth (0 m) coordinates but different elevations (0.22 and 0 m respectively). Target C and E have the same azimuth (0 m) but different elevation (0 and 0.11m respectively) and range (2 and 1.7m respectively) coordinates. Fig. 7.19 shows the 2D SAS images from the 9 baselines used in the acquisition while Fig. 7.20 shows the 2D SAS image obtained from the reference baseline (0.0m). The images look similar with about four dominant bright spots in most of them as opposed to five. This is a

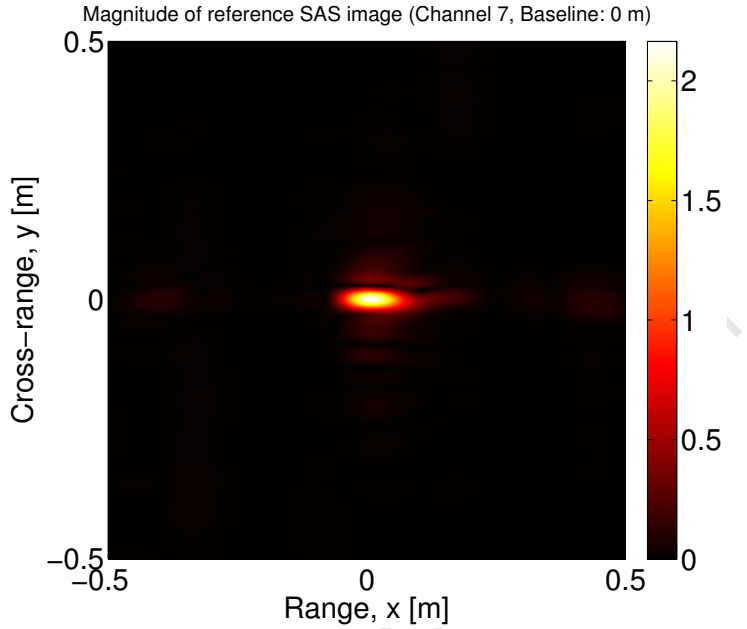

(a)

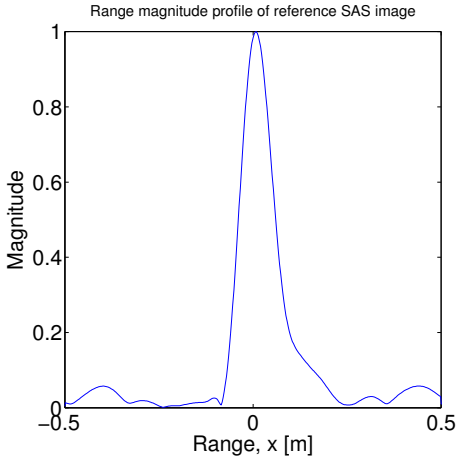

(b) Range magnitude profile at the location of the targets

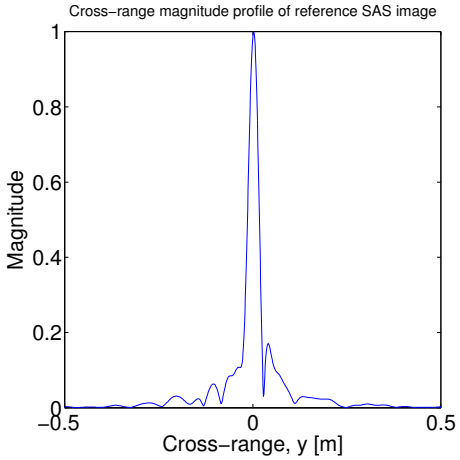

(c) Cross-range magnitude profile at the location of the targets

Figure 7.15: 2D SAS image and profiles from the reference baseline of target scene containing two corner reflectors at the same range and azimuth location but different elevations.

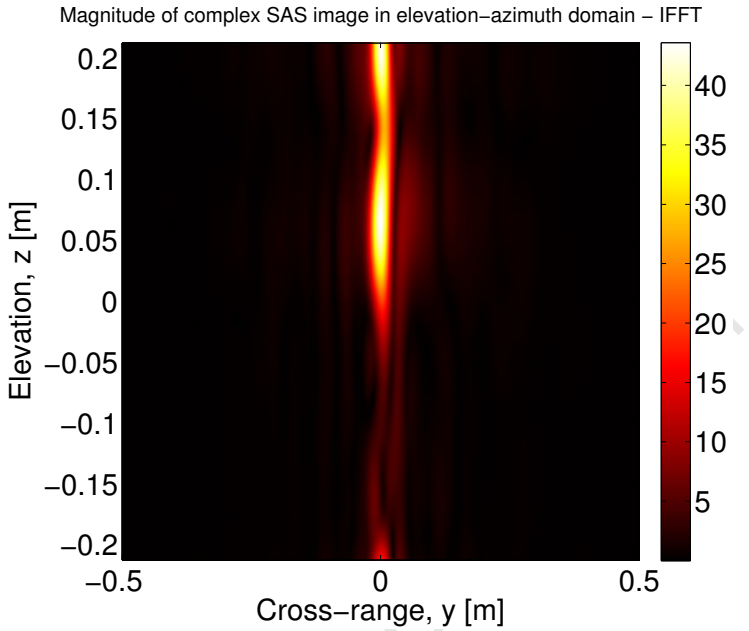

(a) Reconstructed elevation-azimuth section of the target scene using IFFT

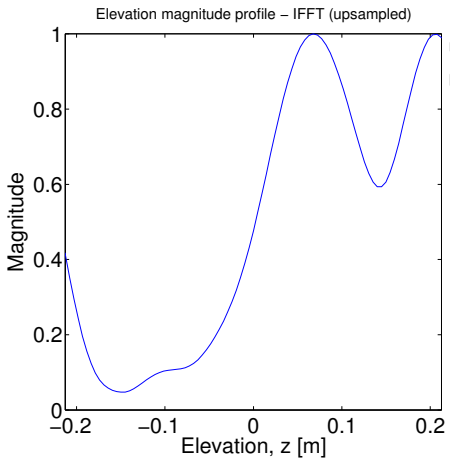

(b) Elevation magnitude profile through cross-range location of the targets

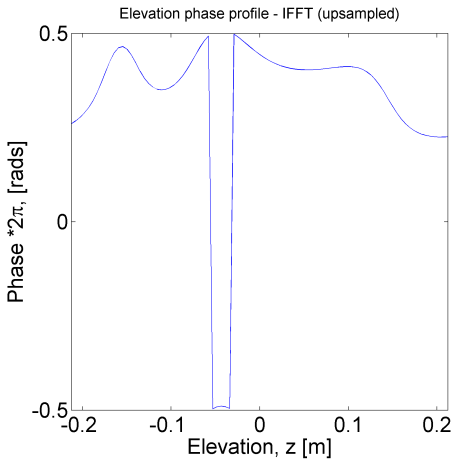

(c) Elevation phase profile through cross-range location of the targets

Figure 7.16: Reconstructed elevation image in the elevation-azimuth domain at the range of the targets using IFFT

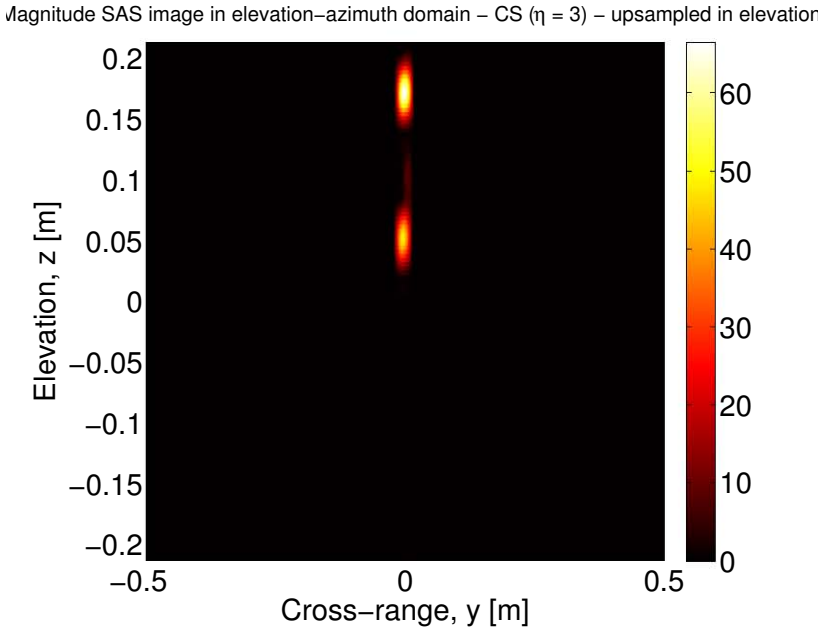

(a) Reconstructed azimuth-elevation section of the target scene using CS

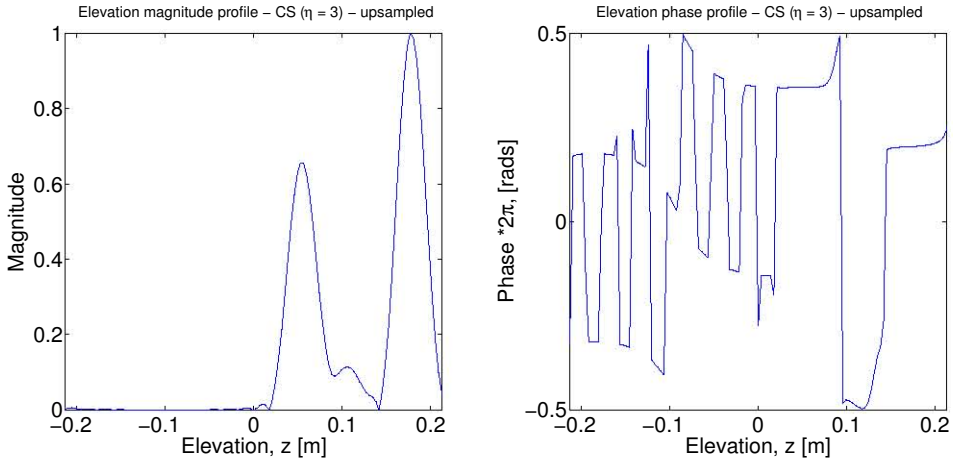

(b) Elevation magnitude profile through cross-range location of the targets

(c) Elevation phase profile through cross-range location of the targets

Figure 7.17: Reconstructed elevation image in the elevation-azimuth domain at the range of the targets using CS with $\eta = 3$ and $\varepsilon = 2.1$

result of the constructive interference of the SAS returns from point targets B and C which cause the responses from these targets to be summed up in the same range-azimuth cell. Deviations in images from the ideal target response could be a result of different viewing angles of the baselines of which the image from the reference baseline is an example. As a result of the viewing angle from this baseline, the point spread function of targets B and C add both constructively and destructively to cause a point spread function which is split into two and with a lower intensity than the other three responses. Fig. 7.21 shows the reconstructed elevation image from two azimuth-elevation sections of the scene using the CS technique with $\eta = 3$ and $\varepsilon = 2.3$. Fig. 7.21a shows reconstructed elevation image in the azimuth-elevation plane of targets A to D ($x = -0.02$m) while the other shows the image in the azimuth-elevation plane of target E ($x = -0.285$m). In these images we see that all the targets have been resolved in azimuth and elevation. While targets A, C and D may not lie at zero elevation, the image shows that they all lie on the same elevation which is correct. The reason they are not reconstructed on zero elevation is because of the view angle of the array. The elevation coordinate is referenced to the reference baseline (or transducer). 0m of elevation means that the target is at a 90 degree view angle (broadside) to the reference transducer. Fig. 7.22 shows the reconstructed elevation image from the range-elevation section through targets B, C and E, from which one can observe that the three targets at the same azimuth position have been separated in both range and elevation.

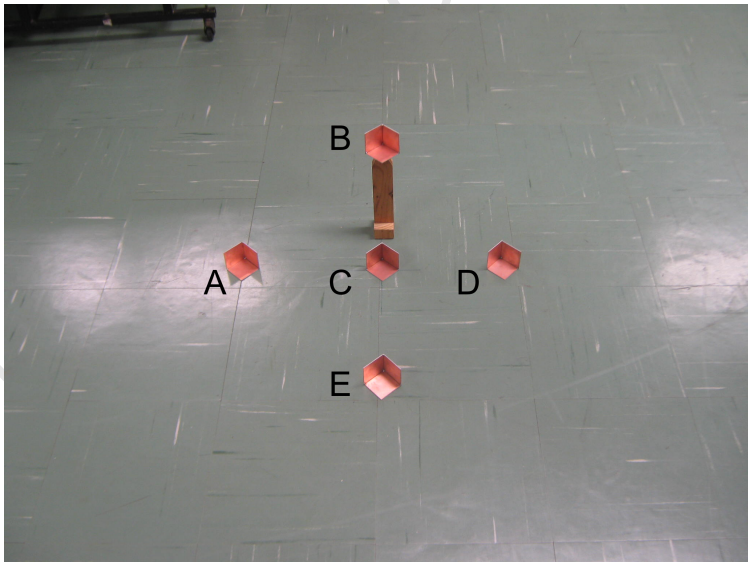

Figure 7.18: Photograph of the target scene containing 5 corner reflectors

7.5 3D SAS Imaging: Toy Robot

In this experiment, the CS reconstruction technique is tested using a toy robot shown in Fig. 7.23. Fig. 7.24 shows the 2D SAS images from the 9 baselines used in the acquisition while Fig. 7.25 shows the 2D SAS image obtained from the reference baseline (0.0m). The images look similar with a number of dominant bright spots in most of them

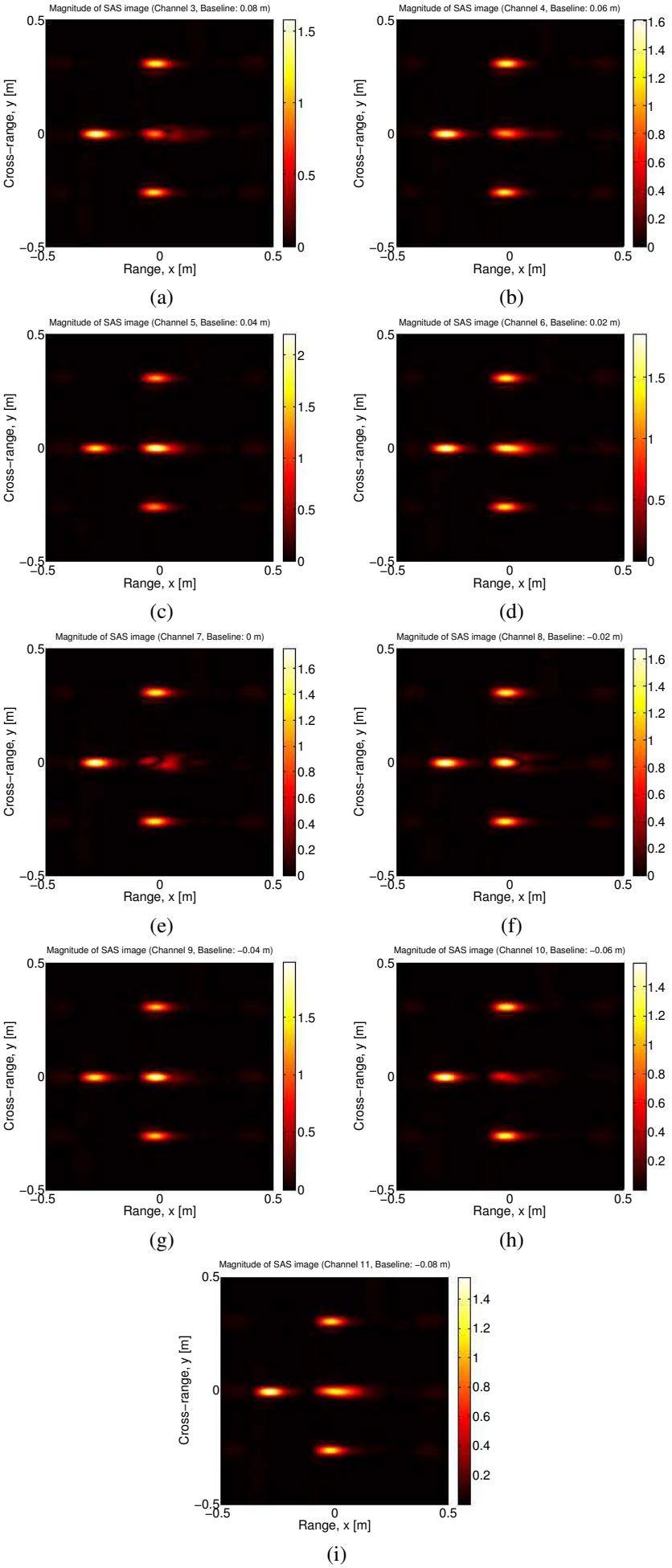

Figure 7.19: 2D SAS images of the scene from 9 uniformly spaced baselines

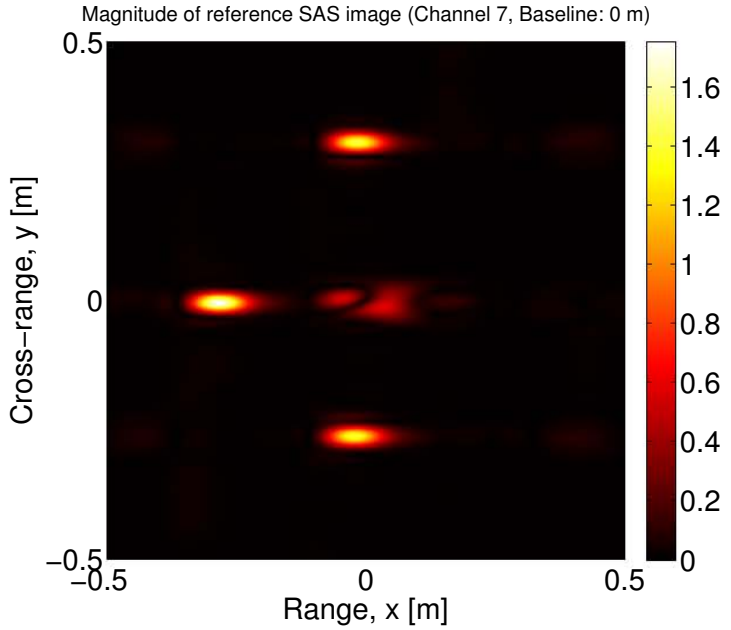

(a)

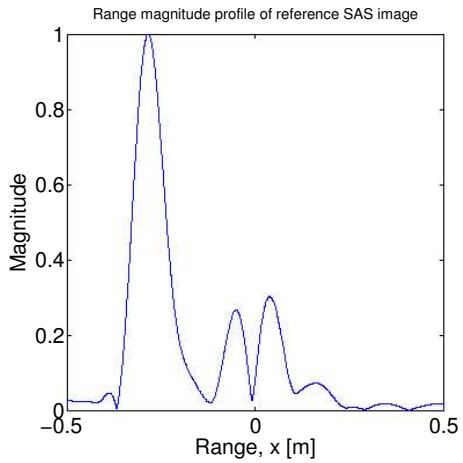

(b) Range magnitude profile at $y = -0.004$m

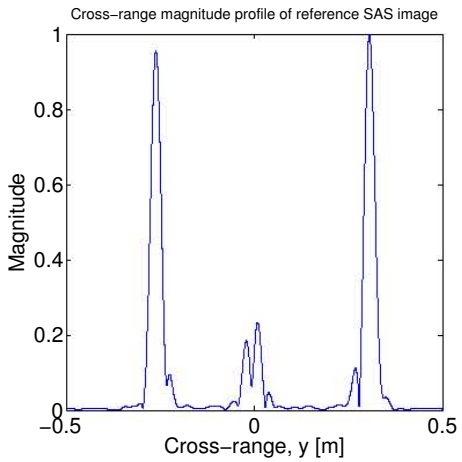

(c) Cross-range magnitude profile at $x = -0.02$m

Figure 7.20: 2D SAS image and profiles from the reference baseline of the scene

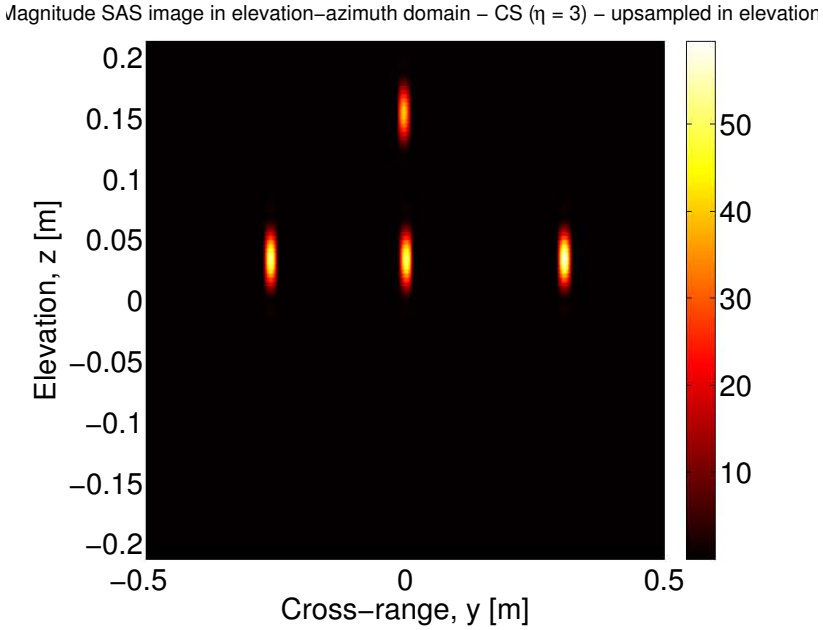

(a) Elevation-azimuth section at $x = -0.02$m

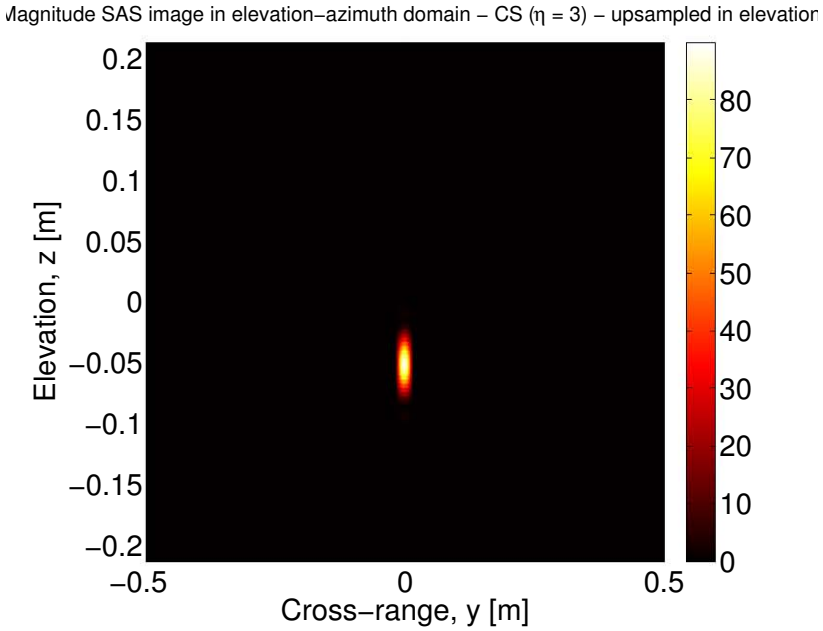

(b) Elevation-azimuth section at $x = -0.285$m

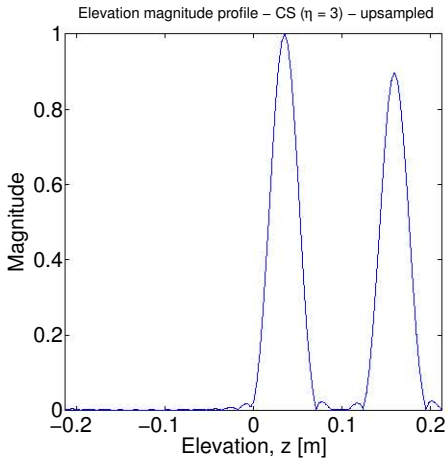

(c) Elevation magnitude profile at $x = -0.02$m and $y = -0.004$m

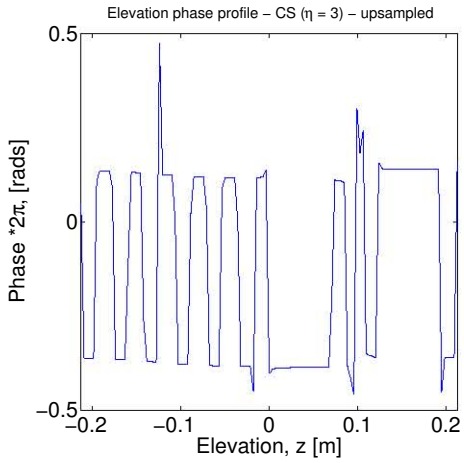

(d) Elevation phase profile at $x = -0.02$m and $y = -0.004$m

Figure 7.21: Reconstructed elevation images in the elevation-azimuth domain using CS with $\eta = 3$ and $\varepsilon = 2.3$.

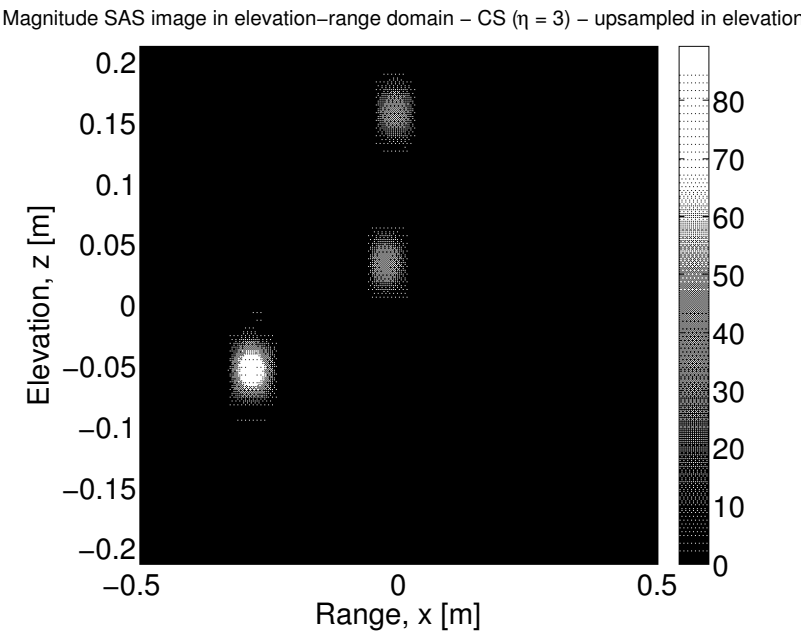

Figure 7.22: Reconstructed elevation image in the elevation-range domain (at $y = -0.004$m) of the targets using CS with $\eta = 3$ and $\varepsilon = 2.3$.

representing the strong ultrasonic reflection from parts of the robot such as the head, hands and feet. Variations in intensity of the reflections across the baseline is a result of the different viewing angles at each point on the baselines. Fig. 7.26 shows the reconstructed elevation image of an elevation-azimuth section of the scene taken at the range of the point targets using the CS technique with $\eta = 3$ and $\varepsilon = 0.015$. Fig. 7.26a shows the reconstructed elevation-azimuth section showing the hands and the head as the dominant reflectors. The left hand is the bright spot on the left-half of the image, the head is the bright spot close to the centre of the image while the right hand is the bright spot in the bottom-right quadrant of the image. Notice that the right hand signature wraps around in the elevation direction. Also the reconstructed image is noisy. One possible reason for this is the choice of the regularization parameter ε which is used to control the sparsity of the CS solution. However this is not the likely reason because the same value of ε was used to reconstruct the elevation-azimuth section containing the legs (Fig. 7.26b) and the result was less noisy. Another possible explanation to the noisy elevation-azimuth reconstruction in Fig. 7.26a is constructive and destructive interference as a result of multipath from surface of the robot.

Remarks

From the results obtained and presented above demonstrate how effective CS is in 3D SAS reconstruction. In particular, the results obtained using the point targets show that the CS technique is capable of resolving targets with the same azimuth and range coordinates but different elevation thereby eliminating the ambiguity of target heights which is present in 2D SAS imaging. While an in-depth theoretical analysis of the effect of super-resolution factor on the ambiguities is outside the scope of this work, this effect was confirmed by

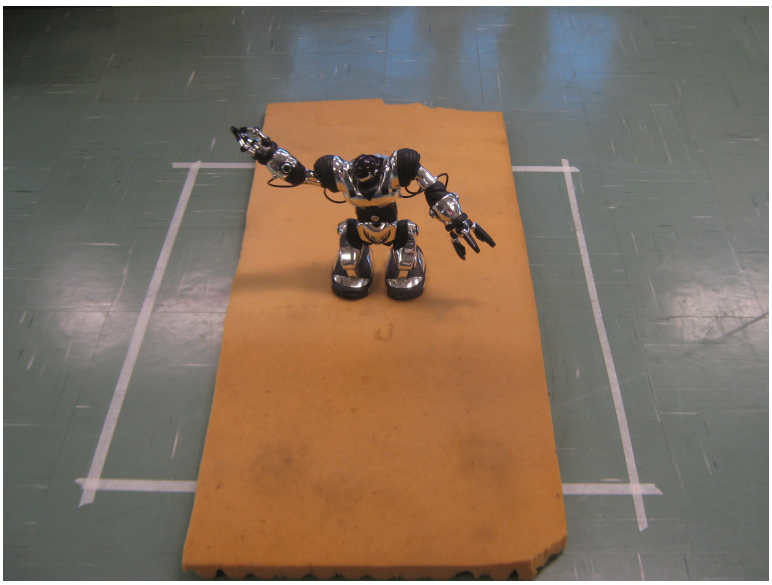

(a) Point of view from the centre of the synthetic aperture

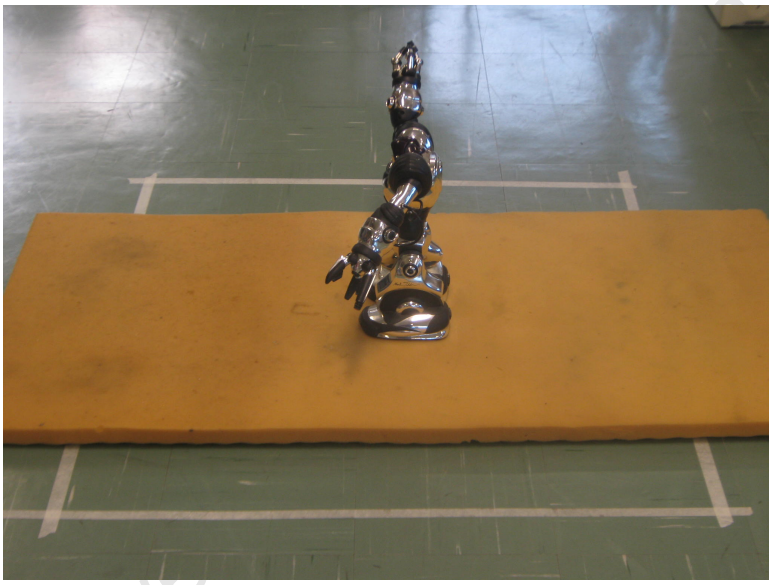

(b) Point of view from mid-range

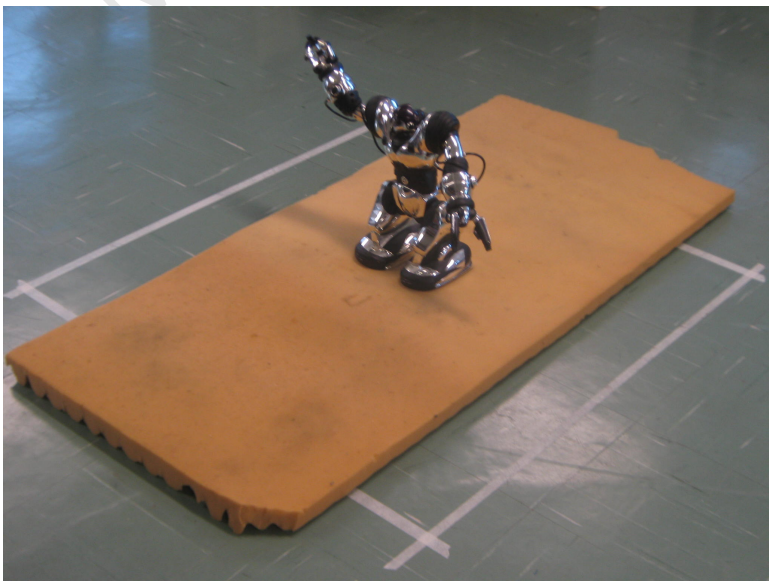

(c) Point of view of operator

Figure 7.23: Photographs of the target scene containing a toy robot from different points of view.

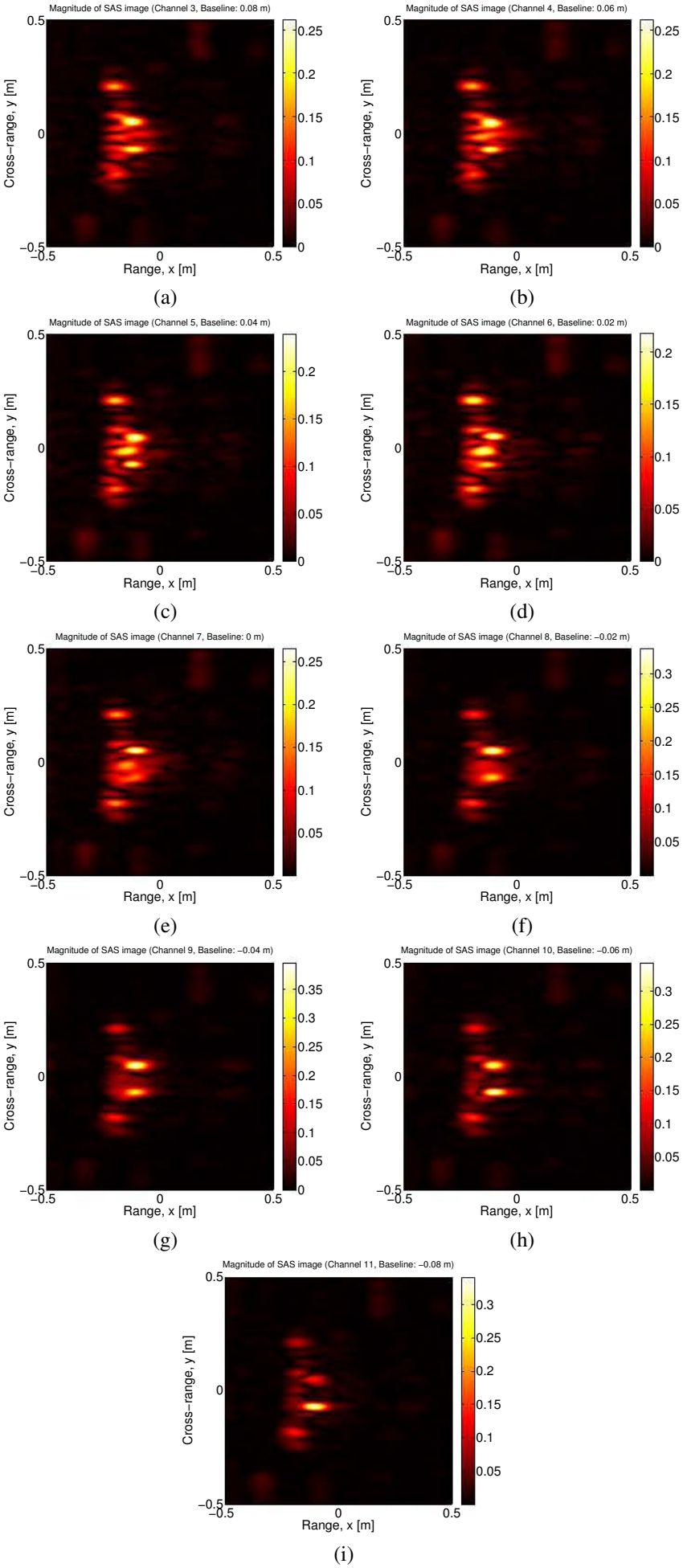

Figure 7.24: 2D SAS images of the toy robot from 9 uniformly spaced baselines

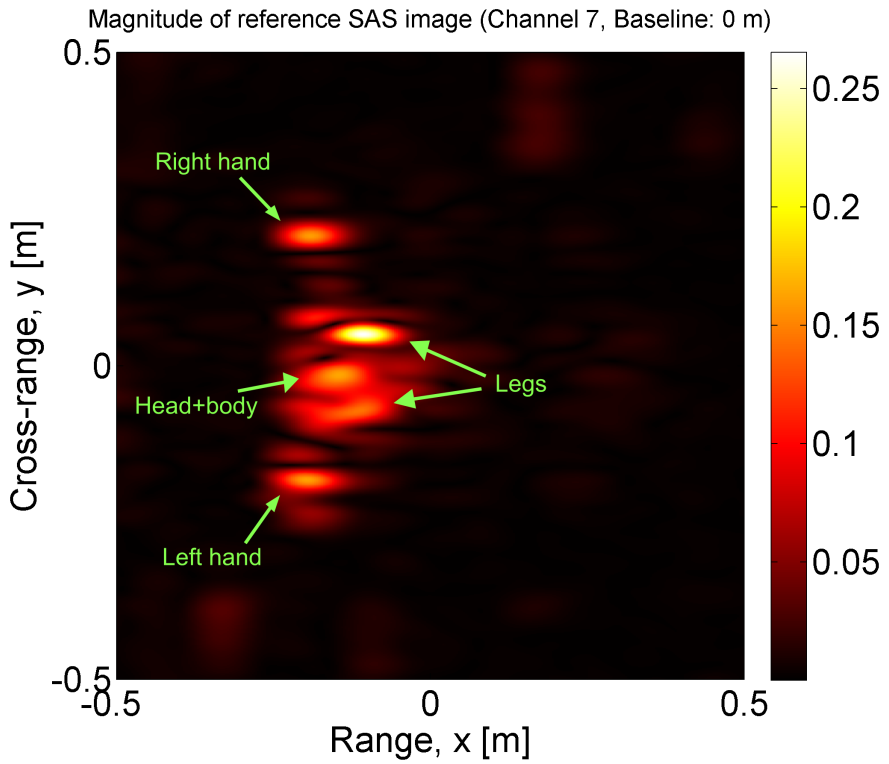

(a)

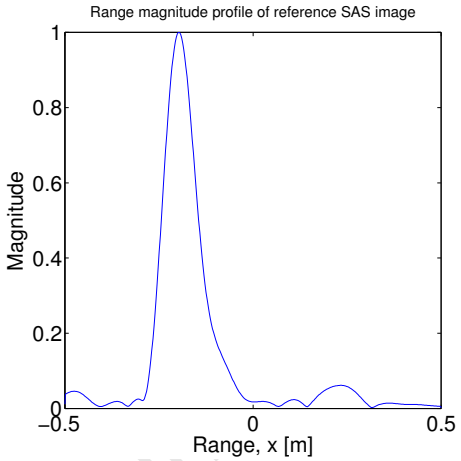

(b) Range magnitude profile at $y = -0.181$m (through the left hand)

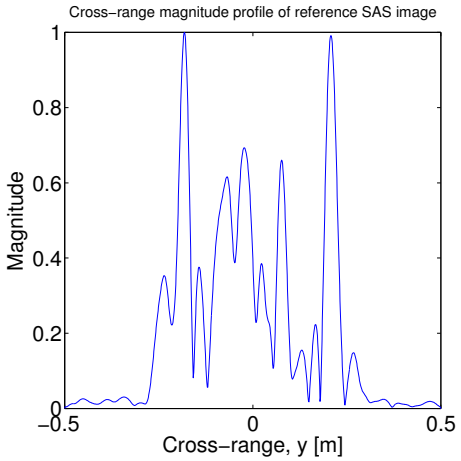

(c) Cross-range magnitude profile at x = -0.198m (through the head and hands)

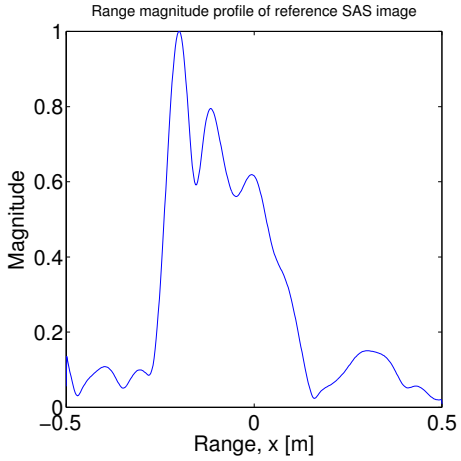

(d) Range magnitude profile at $y = 0.02$m (through the right leg)

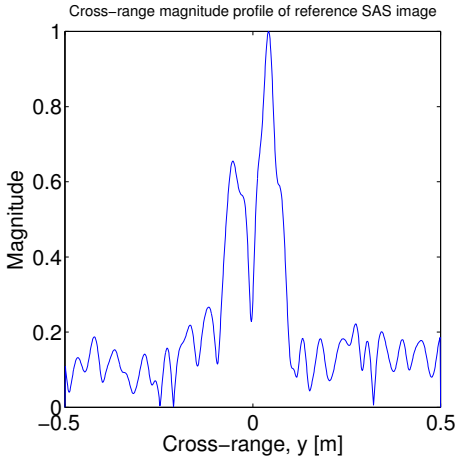

(e) Cross-range magnitude profile at $x = 0.35$m (through the legs)

Figure 7.25: 2D SAS image and profiles from the reference baseline of the toy robot

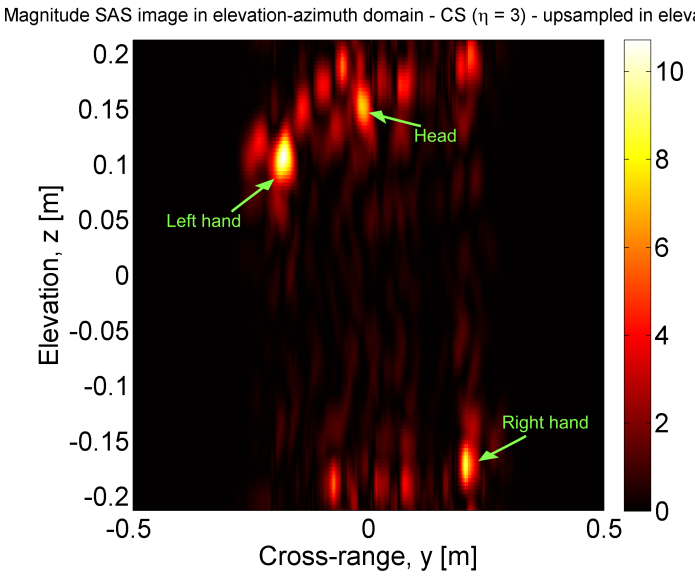

(a) Elevation-azimuth section at $x = -0.198$m showing the hands and head

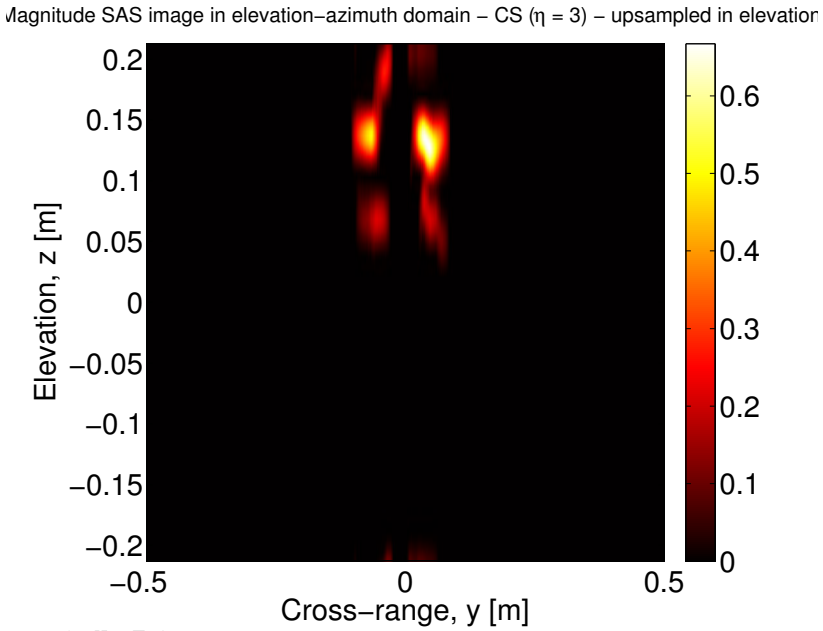

(b) Elevation-azimuth section at $x = 0.35$m showing the legs

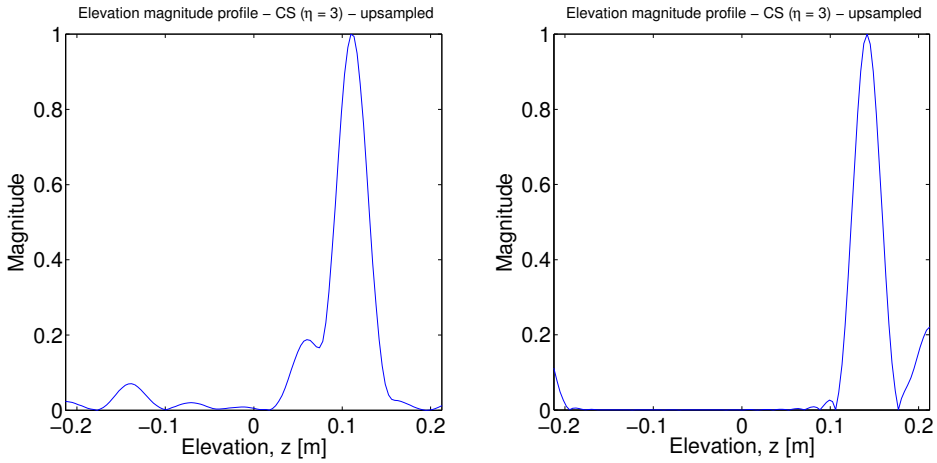

(c) Elevation magnitude profile at $x = -0.198$m and $y = -0.181$m (the left hand)

(d) Elevation magnitude profile at $x = 0.35$m and $y = 0.02$m (the right leg)

Figure 7.26: Reconstructed elevation images in the elevation-azimuth domain using CS with $\eta = 3$ and $\varepsilon = 0.015$.

the results presented in simulation and real data experiments.

Chapter 8

Conclusions and Future Research

An investigation into the three-dimensional synthetic aperture sonar (SAS) imaging using a transducer array and the compressive sampling technique was carried out in this work. The inability to resolve targets of different heights but the same range is a short-coming of typical 2D SAS images and was the motivation behind this work. A number of techniques have been developed for resolving target height information one of which is the compressive sampling/sensing technique. However while some work has been done on applying the technique to synthetic aperture radar tomography, the application of this technique to synthetic aperture sonar imaging has not be investigated. The aim of this work was therefore to carry out an investigation into the possibility of applying the CS technique to synthetic aperture sonar tomography in air. In an attempt to accomplish this objective the following tasks were done:

1. The 3D SAS acquisition and processing system based on compressive sampling was simulated in MATLAB. In order to establish a baseline on which to compare experimental results.

2. An ultrasonic transducer array and a transmit-receive circuitry was designed and implemented to capture raw ultrasonic signals in from different elevations. The ultrasonic transducer array consisted of 15 receive elements and a single transmit element. The transceiver circuitry consisted of bandpass filters and amplifiers.

3. Design of a control system for synthetic aperture data acquisition using LabVIEW and an NI PCI-6070E data acquisition card.

4. Conventional synthetic aperture imaging techniques were carried out on acquired data for 2D SAS images while the compressive sampling technique was applied for elevation resolution.

5. The designed system was tested by imaging test scenes containing point targets at different elevations as well as a physical object. The CS technique was able to resolve the point targets in the 3D scene with super-resolution and parts of the test object.

6. Comparison of the simulated and experimental results to establish the effectiveness of the CS technique in 3D SAS imaging.

From the results obtained the following conclusions and observations were made:

- The CS technique is a spectral estimation technique which is capable of resolving targets in the elevation direction. However for tomographic reconstruction to be treated as a spectral estimation problem, the baseline must be very small compared to the range of imaging and the range resolution must not be too high.
- The CS technique can also be used for super-resolution imaging even with a very small baseline.
- The quality of the reconstructed elevation image depends on the chosen values of the super-resolution factor (η) and the regularization parameter (ε).

This investigation was by no means exhaustive due to time constraints on- and resources available to the project. There is therefore numerous possibilities of further research/investigation into the application of CS to SAS tomography. The following a some of the possible areas to investigate and improvements on the systems that could be made:

- The elevation extent of the scene that can be imaged indirectly depends on the spacing between the baselines as shown in (3.6). In this work the minimum baseline spacing was the diameter of the ultrasonic transducers used (16mm). This work could be repeated using physically smaller transducers in order to have a smaller baseline spacing and thereby image a wider elevation extent.
- The CS technique is not limited to uniformly sampled baselines. It is also effective in tomographic reconstruction using randomly spaced baselines [10, 26, 5] however due to time constraints this was not explored in this work. Future work can be done on the SAS tomographic reconstruction using irregularly spaced baselines.
- The elevation extent is proportional to the range of imaging. In this work the range of imaging was limited to ~2m since the experiments were carried out in indoors. This research can be extended to image over longer ranges.
- As at the time of this writing, the author was not aware/had not come across the application of the CS technique in underwater 3D tomography. This could be an interesting research area as the restrictions on SAS tomography via spectral estimation are easier to satisfy than for air-based SAS tomography.
- Another possible research area is porting of the SAS tomographic processing to a high performance computing platform for real-time imaging. A huge amount of data can be generated from data acquisition in SAS tomography. While execution time of l_1-norm minimization for one data set is fairly fast, it can be several times

longer on large amounts of data which will not be convenient for real-time applications. The application of SAS tomographic reconstruction using CS technique on the GPU or FPGA is an interesting research area.

- The development of a real-time SAS tomography processor based on CS.
- An in-depth theoretical analysis of the effect of super-resolution on induced ambiguities and artifacts especially in the area of ultrasonic 3D imaging using the compressive sampling technique.

Appendix A

Software Source Code

All source code for used in this work was written by the author. Access to all or part of the source codes will be made available on request and at the discretion of the author or the supervisor, Assoc. Prof. Andrew J. Wilkinson of the University of Cape Town.

Bibliography

[1] M. Soumekh, *Synthetic aperture radar signal procesing with MATLAB algorithms*. John Wiley & Sons, 1999.

[2] A. J. Wilkinson, "Notes on radar/sonar signal processing: Fundamentals." University of Cape Town, Department of Electrical Engineering, EEE4001F Lecture Notes, 2011.

[3] J. C. Curlander and R. N. McDonough, *Synthetic aperture radar: systems and signal processing*. John Wiley & Sons, 1991.

[4] G. Fornaro, F. Serafino, and F. Soldovieri, "Three-dimensional focusing with multipass sar data," *Geoscience and Remote Sensing, IEEE Transactions on*, vol. 41, pp. 507 – 517, March 2003.

[5] A. Budillon, A. Evangelista, and G. Schirinzi, "Three-dimensional sar focusing from multipass signals using compressive sampling," *Geoscience and Remote Sensing, IEEE Transactions on*, vol. 49, pp. 488 –499, Jan. 2011.

[6] F. Meglio, G. Panariello, and G. Schirinzi, "Three dimensional sar image focusing from non-uniform samples," in *Geoscience and Remote Sensing Symposium, 2007. IGARSS 2007. IEEE International*, pp. 528 –531, July 2007.

[7] G. Fornaro, F. Lombardini, and F. Serafino, "Three-dimensional multipass sar focusing: experiments with long-term spaceborne data," *Geoscience and Remote Sensing, IEEE Transactions on*, vol. 43, pp. 702 – 714, April 2005.

[8] R. Baraniuk and P. Steeghs, "Compressive radar imaging," in *Radar Conference, 2007 IEEE*, pp. 128 –133, April 2007.

[9] E. Candes and M. Wakin, "An introduction to compressive sampling," *Signal Processing Magazine, IEEE*, vol. 25, pp. 21 –30, March 2008.

[10] X. X. Zhu and R. Bamler, "Very high resolution sar tomography via compressive sensing," in *Fringe 2009 Workshop*, 2009.

[11] H. D. Griffiths, "Radar and sonar imaging - a tutorial introduction," *The Institution of Electrical Engineers*, 1995.

[12] D. Hawkins, *Synthetic Aperture Imaging Algorithms: with application to wide bandwidth sonar*. PhD thesis, University of Canterbury, Christchurch, New Zealand, Oct. 1996.

[13] W. G. Carrara, R. S. Goodman, and R. M. Majewski, *Spotlight Synthetic Aperture Radar Signal Processing Algorithms*. Artech House, Inc., 1995.

[14] M. A. Richards, J. A. Scheer, and W. A. Holm, *Principles of Modern Radar - Basic Principles*. SciTech Publishing, Raleigh, NC, 2010.

[15] K. Tomiyasu, "Tutorial review of synthetic-aperture radar (sar) with applications to imaging of the ocean surface," *Proceedings of the IEEE*, vol. 66, pp. 563 – 583, May 1978.

[16] I. Cumming, F. Wong, and K. Raney, "A sar processing algorithm with no interpolation," in *Geoscience and Remote Sensing Symposium, 1992. IGARSS '92. International*, pp. 376 –379, May 1992.

[17] H. Runge and R. Bamler, "A novel high precision sar focussing algorithm based on chirp scaling," in *Geoscience and Remote Sensing Symposium, 1992. IGARSS '92. International*, pp. 372 –375, May 1992.

[18] J. Munson, D., "An introduction to strip-mapping synthetic aperture radar," in *Acoustics, Speech, and Signal Processing, IEEE International Conference on ICASSP '87.*, vol. 12, pp. 2245–2248, April 1987.

[19] N. Lewitton, "Multiple transducer synthetic aperture sonar interferometry for emulating sar interferometry," Master's thesis, University of Cape Town, Jan. 2007.

[20] J. Munson, D.C. and R. Visentin, "A signal processing view of strip-mapping synthetic aperture radar," *Acoustics, Speech and Signal Processing, IEEE Transactions on*, vol. 37, pp. 2131 –2147, Dec. 1989.

[21] P. Gough and D. Hawkins, "Imaging algorithms for a strip-map synthetic aperture sonar: minimizing the effects of aperture errors and aperture undersampling," *Oceanic Engineering, IEEE Journal of*, vol. 22, pp. 27 –39, Jan. 1997.

[22] R. Bamler, "A comparison of range-doppler and wavenumber domain sar focusing algorithms," *Geoscience and Remote Sensing, IEEE Transactions on*, vol. 30, pp. 706 –713, July 1992.

[23] F. Wong and I. Cumming, "Error sensitivities of a secondary range compression algorithm for processing squinted satellite sar data," in *Geoscience and Remote Sensing Symposium, 1989. IGARSS'89. 12th Canadian Symposium on Remote Sensing., 1989 International*, vol. 4, pp. 2584 –2587, July 1989.

[24] R. Raney, H. Runge, R. Bamler, I. Cumming, and F. Wong, "Precision sar processing using chirp scaling," *Geoscience and Remote Sensing, IEEE Transactions on*, vol. 32, pp. 786 –799, July 1994.

[25] D. Hawkins and P. Gough, "An accelerated chirp scaling algorithm for synthetic aperture imaging," in *Geoscience and Remote Sensing, 1997. IGARSS '97. Remote Sensing - A Scientific Vision for Sustainable Development., 1997 IEEE International*, vol. 1, pp. 471 –473, Aug. 1997.

[26] X. X. Zhu and R. Bamler, "Very high resolution spaceborne sar tomography in urban environment," *Geoscience and Remote Sensing, IEEE Transactions on*, vol. 48, pp. 4296 –4308, Dec. 2010.

[27] R. Bamler, "Email correspondence." Jan 2013.

[28] A. Wilkinson and H. Griffiths, "Novel techniques for 3-d target reconstruction in sar interferometry," in *Radar and Microwave Imaging, IEE Colloquium on*, vol. 1, pp. 1–6, Nov. 1994.

[29] S. Cloude and K. Papathanassiou, "Polarimetric sar interferometry," *Geoscience and Remote Sensing, IEEE Transactions on*, vol. 36, pp. 1551 –1565, Sept. 1998.

[30] J. Webb and J. Munson, D.C., "Radar imaging of three-dimensional surfaces using limited data," in *Image Processing, 1995. Proceedings., International Conference on*, vol. 1, pp. 136 –139, Oct. 1995.

[31] S. S. Chen, D. L. Donoho, and M. A. Saunders, "Atomic decomposition by basis pursuit," *SIAM Rev.*, vol. 43, pp. 129–159, Jan. 2001.

[32] Y. C. Eldar and G. Kutyniok, eds., *Compressed Sensing: Theory and Applications*. Cambridge University Press, 2012.

[33] S. Winter, H. Sawada, and S. Makino, "On real and complex valued l1-norm minimization for overcomplete blind source separation," in *Applications of Signal Processing to Audio and Acoustics, 2005. IEEE Workshop on*, pp. 86 – 89, Oct. 2005.

[34] E. van den Berg and M. P. Friedlander, "SPGL1: A solver for large-scale sparse reconstruction," June 2007. http://www.cs.ubc.ca/labs/scl/spgl1.

[35] E. van den Berg and M. P. Friedlander, "Probing the pareto frontier for basis pursuit solutions," *SIAM Journal on Scientific Computing*, vol. 31, no. 2, pp. 890–912, 2008.

[36] J. F. Sturm, "Using sedumi 1.02, a matlab toolbox for optimization over symmetric cones," *Optimization Methods and Software*, vol. 11-12, pp. 625–653, 1999.

[37] National Instruments, *NI PCI-6070E Data Sheet*.

[38] National Instruments Corporation, *LabVIEW Tutorial Manual*.

[39] G. Fornaro and G. Franceschetti, "Image registration in interferometric sar processing," *Radar, Sonar and Navigation, IEE Proceedings* -, vol. 142, pp. 313 –320, Dec. 1995.

[40] R. Abdelfattah and J. M. Nicolas, "Sub-pixelic image registration for sar interferometry coherence optimization," in *XXth ISPRS Congress* (O. Altan, ed.), vol. XXXV, pp. 273–376, 2004.

[41] F. O. Oladipo, "Design and implementation of a parallel registration algorithm for sar images," Master's thesis, Department of Electrical Engineering, University of Cape Town, 2001.

[42] M. Guizar-Sicairos, S. T. Thurman, and J. R. Fienup, "Efficient subpixel image registration algorithms," *Opt. Lett.*, vol. 33, pp. 156–158, Jan. 2008.

[43] W. Zou, Y. Li, Z. Li, and X. Ding, "Improvement of the accuracy of insar image co-registration based on tie points - a review," *Sensors*, vol. 9, no. 2, pp. 1259–1281, 2009.

[44] A. Budillon and G. Schirinzi, "Artifact reduction in sar compressive sampling tomography," pp. 2700–2703, 2011.

[45] J. M. Horrell, *Range-Doppler Synthetic Aperture Radar Processing at VHF Frequencies*. PhD thesis, University of Cape Town, Department of Electrical Engineering, 1999.

[46] Y. Wang, B. Wang, W. Hong, L. Du, and Y. Wu, "Imaging geometry analysis of 3d sar using linear array antennas," in *Geoscience and Remote Sensing Symposium, 2008. IGARSS 2008. IEEE International*, vol. 3, pp. 1216–1219, July 2008.

[47] J. Wu, X. Zhang, X. Wang, L. Senhadji, and H. Shu, "L1-norm minimization for quaternion signals," *CoRR*, vol. abs/1202.5471, 2012.